Temporal Structure of AGN Light Curves: Tracers of the Physics of the Emission Processes

DISSERTATION

der Fakultät für Physik der Ludwigs-Maximilians-Universität
München
zur Erlangung des Grades
Doktor der Naturwissenschaften
Dr. rer. nat.

vorgelegt von

PATRICIA ARÉVALO
aus Santiago, Chile

München, den 5. December 2005

1. Gutachter: Prof. G. Morfill
2. Gutachter: Prof. R. Saglia
Tag der mündlichen Prüfung: 15. März 2006

Contents

1 **Introduction** **1**
  - 1.1 Active Galactic Nuclei 1
    - 1.1.1 Accretion 4
    - 1.1.2 X-ray Emission 6
  - 1.2 Why Study X-ray Variability? 7
    - 1.2.1 Characteristics of the Variability 8
  - 1.3 Statistical Tools 10
    - 1.3.1 Scatter and Significance, Tests with Artificial Data 15
  - 1.4 Research Topics 20
    - 1.4.1 Simultaneous Flux/Spectral Variability 21
    - 1.4.2 Correlated Variability Between Energy Bands 21
    - 1.4.3 A Phenomenological Model for the Flux Variability 22

2 **X-ray variability of the NLS1 PKS 0558–504** **25**
  - 2.1 Abstract 25
  - 2.2 Introduction 26
  - 2.3 Observations and temporal analysis 28
    - 2.3.1 Hardness Ratios 33
  - 2.4 Spectral analysis 35
    - 2.4.1 High energy power law fits 39
  - 2.5 Discusssion 40
    - 2.5.1 Spectral properties 40
    - 2.5.2 Temporal variability: short time scales 44
    - 2.5.3 Temporal variability: longer time scales 47
    - 2.5.4 Temporal variability: the longest time scales 47
  - 2.6 Conclusions 48

3 X-ray to UV Variability Correlation in MCG-6-30-15 51
3.1 Abstract . . . 51
3.2 Introduction . . . 52
3.3 Data reduction and light curves . . . 53
3.3.1 X-ray light curves . . . 54
3.3.2 UV light curves . . . 54
3.4 Cross-correlation analysis . . . 60
3.4.1 DCF between the UV flux and the variations in the X-ray energy spectrum . . . 64
3.5 Discussion . . . 64
3.5.1 Comptonisation scenario . . . 66
3.5.2 Reprocessing scenario . . . 68
3.5.3 Comparison with previous results . . . 69
3.6 Conclusions . . . 71

4 Investigating a Fluctuating-accretion Model for the Spectral-timing Properties of Accreting Black Hole Systems 73
4.1 Abstract . . . 73
4.2 Introduction . . . 74
4.3 The Model . . . 76
4.3.1 Model construction and basic assumptions . . . 78
4.3.2 Numerical implementation . . . 79
4.3.3 Analytical estimates . . . 82
4.4 Spectral-Timing Properties . . . 83
4.4.1 Dependence on emissivity indices . . . 84
4.4.2 Disc structure parameters . . . 88
4.4.3 Input signals . . . 90
4.4.4 Damping . . . 93
4.5 Comparison with AGN X-ray light curves . . . 96
4.5.1 Time lags . . . 97
4.5.2 Energy dependence of the PSD . . . 97
4.5.3 Cross correlations . . . 101
4.6 Application to Cyg X-1 data . . . 104
4.7 Discussion . . . 110
4.7.1 Time lags . . . 110
4.7.2 PSD shape . . . 111
4.7.3 Extent of the emitting region . . . 112
4.7.4 Improvements to the model . . . 112
4.8 Conclusions . . . 114
4.9 Appendix A: Analytical estimates for filtered PSD and lags . 116

4.10 Appendix B: Spectral-timing measurements 117

5 Conclusion 119

Chapter 1

Introduction

1.1 Active Galactic Nuclei

The general denomination of Active Galactic Nuclei (AGN) refers to the small fraction of galaxies that contain an extremely luminous and compact core. Carl Seyfert was the first to catalogue these sources systematically, identifying them by their bright nuclei and very distinguishable strong *emission* lines. Seyfert originally classified these galaxies into two types, according to their optical energy spectra: Type 1 Seyfert galaxies show a strong featureless continuum and, superposed on this, broad permitted lines and narrow permitted and forbidden emission lines. Seyferts of type 2 have a much weaker continuum and narrow permitted and forbidden lines.

Subsequently, more types of objects appeared to comply with the broad definition of AGN, initiating a wide variety of classification criteria. Roughly 10% of Seyfert galaxies were identified with strong radio sources, receiving the name of radio-loud AGN or radio galaxies (RG). The same optical spectral classification of Seyferts applies to radio galaxies, namely broad-line (BLRG) and narrow-line (NLRG). Radio galaxies are further classified by the morphology of their radio-emitting regions, which can be core-dominated or extended in giant radio lobes, many times connected to the centre of the host galaxy by highly collimated jets.

Later it was recognised that some objects, quasi-stellar in appearance, had similar spectra to Seyfert 1 galaxies, but highly red-shifted. The measured red-shifts place them at cosmological distances. They were also identified with radio emitters and were named Quasi-Stellar Radio Sources, or Quasars. When many more of these optical objects resulted to be radio-quiet they received the general name of Quasi Stellar Objects, QSO. QSOs were interpreted as extremely luminous versions of Seyfert 1s, with nuclear flux many times out-shining the whole host galaxy, making them the most distant and luminous objects known at the time. The current definition of Quasars includes a luminosity threshold, stating a maximum absolute magnitude, $M < -24$. One last class of AGN consists of Blazars. These are characterised by a featureless power-law continuum energy spectrum, high polarisation and rapid variability. BL Lac objects and Optically Violently Variables (OVVs) belong to this class.

A striking characteristic of the various classes of AGN is their very broad energy spectrum, ranging from radio wavelengths to X-rays. These spectral energy distributions (SED) are very different from those of normal galaxies and are partly attributable to non-thermal processes such as synchrotron radiation and Compton scattering.

The central engine

The central regions of active galaxies cannot be resolved observationally and have a point-like appearance. A way to estimate the size of the emitting region is through the observed rapid flux variability that characterises these objects. Considering that significant changes in the flux must come from a causally connected region, typical variability on time scales of hours give maximum sizes of several Astronomical Units, indicating that the source must be very compact. Quasars have typical luminosities of 10^{45} to more than 10^{48} erg/s, a source capable of producing such large luminosities must be very massive or the radiation pressure would overwhelm the gravitational pull causing the object to blow apart. For spherically symmetric accretion on to a body of mass M, having Thompson scattering as the main interaction between the in falling matter and the radiation field, the maximum luminosity is limited by the Eddington luminosity $L_{\rm Edd} \sim 1.5 \times 10^{38} M/M_\odot$, where $M_\odot = 2 \times 10^{33} g$ is the mass of the Sun. This relation implies masses of 10^6 to up to 10^{10} $\mathrm{M}_\odot$ for the central engines of Seyferts and Quasars. More accurate studies using the Doppler broadening of the permitted lines and the time it takes them to react to changes in the ionising continuum flux yield results consistent with these estimates.

The requirements of high mass, small size and high energy output of the central engine constrain the possible mechanisms that power the AGN. One model that complies with these requirements is accretion on to a compact massive object. Accretion is the most efficient mechanism to liberate large amounts of energy for a given mass, as in this process the in-falling matter must loose an amount of gravitational potential energy comparable to its rest mass. Depending on the accretion rate, this process can produce the required luminosities within a very small region. There is now general agreement that the source of the huge AGN luminosity is accretion of matter on to a super massive central black hole.

Unification

In 1985 R. Antonucci and J. Miller discovered broad lines in the spectrum of a Seyfert 2 galaxy, when observed in polarised light. This result suggests that this Seyfert 2 contains a Seyfert 1 nucleus heavily obscured from direct view but observable in reflected, and so polarised, light. This fact and other similarities between Seyferts 1 and 2 lead to the emergence of Unification Schemes, where both classes of galaxies would correspond to the same physical objects and their observed properties would differ as a result of their orientation with respect to the observer. Current Unified Schemes propose that AGN consist of the following structures: A central black hole and accretion disc as the primary source of emission and a possible jet emerging perpendicularly to the disc. Further out, a set of high velocity clouds in Keplerian orbits giving rise to the broad lines, i.e. the broad-line region. These structures are hidden from direct view at some observing angles by high column density material, often referred to as the molecular torus although its geometry is not well constrained. Finally, lower velocity, lower density clouds provide the narrow permitted and forbidden lines observed in both classes of objects. A schematic diagram is shown in Fig. 1.1, identifying the main structures of the AGN and the classification depending on observation angle.

The unified model provides at least a phenomenologically consistent picture of broad and narrow-line objects. However, it has become clear that orientation effects cannot account for all the differences in observable parameters among different classes of AGN, and so, some of these must have an intrinsic origin. Specifically, the central black-hole mass, its spin parameter and the accretion rate are probably the next defining parameters in the classification of AGN.

In particular one class of objects that does not fit in the simple paradigm described above are Narrow Line Seyfert 1 (NLS1) galaxies. These have an optical spectrum similar to Seyfert 1 but their permitted broad lines are in the narrower end of the range. This narrower broad-lines are interpreted as broad lines coming from clouds orbiting a less massive central black hole, and so, having smaller Keplerian velocities. However, their luminosities are comparable with those of normal Seyfert 1 galaxies, implying that NLS1 are going through a process of violent growth through high accretion rates. The classification of NLS1 as a distinct class of objects is supported by their

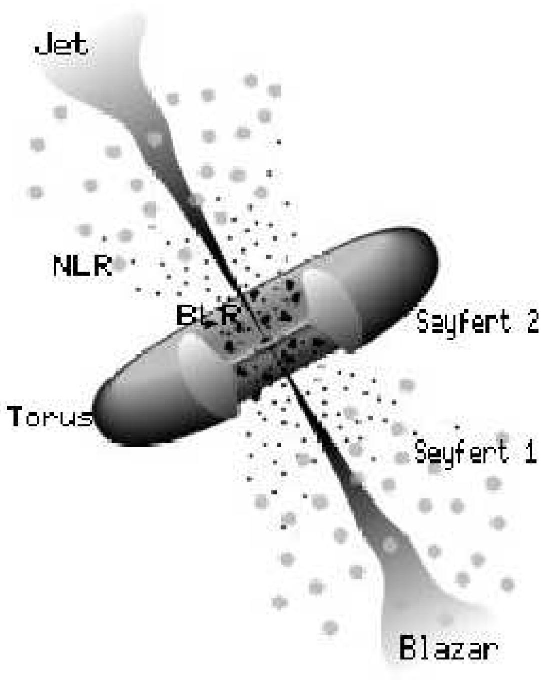

Figure 1.1: Schematics of the AGN unification paradigm, figure adapted from Urry & Padovani (1995), featuring a relativistic jet, narrow-line region (NLR) clouds, broad-line region (BLR) clouds, molecular torus, and a central accretion disc and black hole. A line of sight aligned with the jet gives the AGN the appearance of a Blazar. At higher inclinations, but still with direct view to the central engine, the AGN appears as a Seyfert 1; at an edge-on view the torus obscures the central engine and the BLR giving the AGN a Seyfert 2 look.

X-ray characteristics, they have significantly softer X-ray spectra and larger, more rapid variability than their broad line counterparts. In fact, it is the extreme fluctuation properties of NLS1s that make them ideal objects for the study of these systems from the variability approach.

1.1.1 Accretion

Given that the mechanism powering the AGN is very likely accretion onto a compact object, it is important to study if and how this matter can be fed to the black hole. In a simple picture, gas falls in the potential well of the galactic centre towards the central black hole. This gas will have a finite total angular momentum which provides a preferred direction. The system of gas clouds will proceed to minimise its energy by flattening into a disc structure of matter following circular Keplerian orbits. If the material can cool efficiently, it will form a very thin disc. Spectral fitting of X-ray emission lines are consistent with fluorescence produced by material in a Keplerian orbit very close to the central black hole, preferring disc geometries, and give strong evidence for the presence of an accretion disc.

However this matter has angular momentum so it cannot proceed to fall on to the black hole directly. It is necessary to include a mechanism that produces an effective viscosity ν responsible for the transport of angular momentum outward, thus allowing matter to move inward and be effectively *accreted*. The actual value needed for this viscosity is too high to be explained by mechanical interaction between the particles but other mechanisms have been proposed to achieve the necessary rate of angular momentum transport, such as shear stresses produced by e.g. magnetic fields in the accretion disc, magnetically driven outflows or turbulence.

The accretion luminosity equals the amount of gravitational energy that must be lost by the accreting matter before reaching the last stable orbit, as from there inwards it need not loose energy or angular momentum to continue falling. This luminosity is proportional to the accretion rate. In terms of the efficiency η, $L_{\rm acc} = \eta \dot{M} c^2$. The value of η depends on how deep into the potential well of the black hole can the matter go before reaching the last stable orbit. This depends on the spin of the black hole, as for higher spin parameters the last stable (prograde) orbit moves inwards from 6 to 1 $R_{\rm g}$, where the gravitational radius is given by $R_{\rm g} = GM/c^2$. The theoretical limiting values for the efficiency are $0.057 < \eta < 0.423$ for a non-rotating to a maximally rotating central black hole. Notice, however, that if the flow is radiatively inefficient part of this luminosity will be advected and the *observed* luminosity can be much smaller.

Early on, Shakura & Sunyaev (1973) proposed a simple prescription for the viscosity, as a first attempt to study the disc structure and behaviour. In this approach, the viscosity is simply related to the pressure P through: $\nu = \alpha c_s H$ where H is the vertical scale hight and c_s the sound speed given by $c_s^2 = P/\rho$. The viscosity allows the infall of matter and gives it a radial velocity, as a function of radial position R, $v_{\rm viscous}(R) = \alpha (H/R)^2 R \Omega_K(R)$, where (H/R) is the ratio between the disc half thickness and radius and $\Omega_K(R)$ is the Keplerian orbital frequency. Therefore, higher values of α and/or thicker discs produce larger infall velocities. With this α-prescription the structure equations of the thin disc can be directly solved. Although this is a very simplified approximation it is useful to calculate order-of-magnitude estimates of parameters such as the the radial velocity of in-falling matter or of observable quantities such as the energy spectrum of the radiation emitted by the disc. For example, assuming that the energy output of the AGN is produced as thermal radiation from the accretion disc through viscous dissipation, a crude estimate of the disc temperature can be directly computed as

$$T_{\rm eff}(R) = \left[\frac{3GM\dot{M}}{8\pi\sigma R^3} \left(1 - \sqrt{\frac{R_{in}}{R}} \right) \right]^{1/4} , \tag{1.1}$$

where M is the BH mass, $\dot{M}$ is the accretion rate, R is the distance from the centre and R_{in} is the position of the inner edge of the disc. This relation is simply given by the expected black body flux emitted per unit area in the disc given the local loss of gravitational energy from the infalling matter. This approximation describes the disc emission as a multi-temperature black body which, for the masses and luminosities of typical AGN, peaks in the optical band for high mass objects and in the UV/soft X-rays for lower-mass black holes. This disc contribution is often identified as the 'Big Blue Bump' component of AGN SEDs, although accurate spectral fitting requires additional effects and components.

The luminosity of the central engine can heat the disc or, alternatively the disc can be radiatively inefficient, in both cases radiation pressure can dominate over gravity and the disc becomes geometrically thick. Thick discs have different emissivity properties and time scales as thin discs, producing a wealth of different predictions for the observable quantities. Present efforts are directed towards modelling the time evolution of disc structures and to produce accurate spectra for different accretion disc types.

1.1.2 X-ray Emission

As noted in the previous section, pure accretion disc thermal emission cannot account for the hard X-ray spectrum observed in AGN. For radio-loud objects, where a relativistic jet is probably present, the X-ray emission can sometimes be explained by a continuation of the radio synchrotron spectrum. However, X-rays are also observed in radio-quiet objects and so a different emission process must be at work.

A preferred source of X-rays is inverse Compton scattering of soft photons, in the optical/UV range, through an optically thin cloud of hot electrons (e.g. Sunyaev & Titarchuk, 1980). This process can produce power-law X-ray spectra for some ranges of the parameters of the electron distribution and is probably responsible for at least part of the hard X-ray emission. Unsaturated Comptonised spectra have a power-law shape with high- and low-energy cut-offs, broadly defined by three parameters, namely the temperature of the source of thermal 'seed' photons $T_{\rm o}$, optical depth τ and temperature T of the hot electrons. The first parameter defines the low energy cut-off of the Comptonised spectrum as few photons are down-scattered to lower energies. The energy of the outgoing photons will increase with the average energy of the electrons it encounters and with the average number of encounters, given by the optical depth of the medium. A combination of optical depth and electron temperature then defines the slope of the power-law spectrum and the electron temperature alone defines the high energy cut-off.

Observationally, the slope of the X-ray spectrum can be measured but the high energy cut-off often falls above the sensitivity range of the instruments and cannot be determined. Therefore, it is possible to constrain the Comptonisation parameter $y \sim T\mathrm{max}[\tau, \tau^2]$, but not each parameter separately.

The process of inverse Compton scattering is quite well understood. Much more uncertainty remains regarding the origin and geometry of the Comptonising media in AGN. Popular models invoke the presence of a 'corona' over the accretion disc, in analogy to the X-ray emitting solar corona. These models propose that a cloud of electrons over the disc surface can be heated by magnetic reconnection and Comptonise the thermal photons coming from the underlying disc. Haardt & Maraschi (1993) and Haardt, Maraschi & Ghisellini (1994) have studied some configurations for the corona model to predict spectra, through self-consistent solutions of energy equilibrium between the disc and corona. Many parameters of these models remain unconstrained and continue to be studied through AGN X-ray observations.

1.2 Why Study X-ray Variability?

AGN are notoriously variable, both in flux and in spectrum, providing a wealth of information through their timing properties. Moreover, as their central engines are too small to be imaged, the structures that compose the AGN can only be modelled and constrained through indirect measurements such as energy spectra and variability properties.

A simple measure like the typical time scale of large amplitude fluctuations in the flux at different energy bands gave early estimates on the size of the corresponding emitting regions, and correlations between these fluctuations gave information on their connections. The study of variability has now been taken much further than these first estimates, both in the identification of structures in the time series provided by the light curves and on the physical interpretation of these structures.

1.2.1 Characteristics of the Variability

AGN light curves show significant variability in a broad range of time-scales, generally composed of aperiodic fluctuations and therefore referred to as noise. The top panel of figure 1.2 shows an X-ray observation of the Seyfert 1 galaxy MCG-6-30-15. This source displays high amplitude variability, reaching in this observation flux changes by a factor of ~ 5 in less than 3 hours. There is, however, significant variability at longer and shorter timescales too, all these compose the variability pattern. Just by eye, it is easy to see that the long time-scale fluctuations have higher amplitude than the faster variability. The distribution of variability "power" among different temporal frequencies can be a defining characteristic of the variability. The *Power Spectral Density* (PSD) determines the variability amplitude as a function of Fourier frequency and it is a characteristic of the variability process. The Power Spectra of AGN light curves usually have a power law dependence on Fourier frequency $P(f) \propto f^{-\alpha}$, with greater power at lower frequencies. This type of variability, where the Power Spectrum has a power-law shape with $\alpha \sim 1$ is often referred to as *red noise*, as opposed to *white noise* where there is no dependence of variability power on time-scale.

In the case of the MCG-6-30-15 light curve in figure 1.2 the power spectrum is well fitted by a power law of index ~ -1.8 at high frequencies, changing to a flatter slope of index ~ -1 at the lowest frequencies. For comparison, the middle panel presents an artificial red-noise light curve with $\alpha = 2$, this means that low frequency fluctuations have significatively more variability power than high frequency ones, resulting in relatively smooth high amplitude fluctuations in long timescales. The bottom panel shows a similar light curve but this time with $\alpha = 1$ which gives similar power to high and low frequency fluctuations. AGN X-ray light curves normally show intermediate values of α. The value of α can further depend on the time-scales probed, so that the power spectrum is shaped as a broken or doubly-broken power-law, determining different regimes of the variability process. The Power Spectrum slope can also depend on energy band, implying differences between the emitting regions.

Another feature of this observed light curve is that it seems to be more

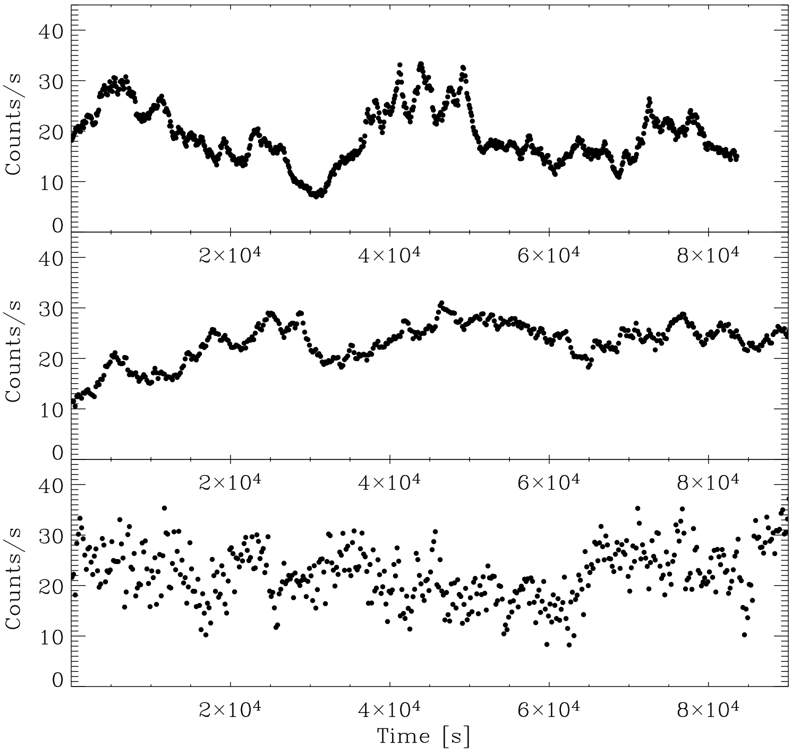

Figure 1.2: top panel: X-ray light curve of the Seyfert 1 galaxy MCG-6-30-15 in 100 s bins, the errors in count rate are smaller than the symbols. Middle and bottom panels: artificial red noise light curves with power spectral indices of -2 and -1 respectively.

variable when the flux is higher. This fact was noticed by Uttley & McHardy (2001) and described formally as a linear relation between the square root of the light curve variance $\sigma_{\rm rms}$ and the flux. This relation is seen in different kinds of accretion-powered objects and holds for a variety of time-scales, suggesting that it is a main feature of the underlying variability process. A related characteristic is the *log-normal* distribution of the fluxes (Gaskell, 2004). According to this, bins with fluxes *much higher* than the mean are more common than bins with fluxes *much lower* than the mean, so the distribution around the mean count rate is asymmetric but the distribution of the logarithm of the fluxes is symmetric and, in fact, Gaussian.

Finally, light curves from different X-ray energy bands exhibit slightly different behaviours. Although they are usually highly coherent, higher energy light curves tend to have relatively more short-timescale variability and also tend to lag behind the fluctuations of softer X-ray bands. These time lags between energy bands appear to increase both with the time-scale of the fluctuations and with the separation of the energy bands.

The physical interpretation of these properties is still very speculative. Many phenomenological and more physical models have been constructed to explain the PSD shape and the time lags between different X-ray energy bands. Most of these models propose means to generate a range of randomly activated regions, whose sizes follow a power-law distribution. This class includes self-organised criticality and avalanche-flare models, which can reproduce well the power-law dependence of the variability amplitude on frequency. All these however fail to predict the non-linear characteristics of the light curves (i.e. $\sigma_{\rm rms}$-flux relation, log-normal distribution) and so suggest that a totally different mechanism is required to produce the variability. A model proposed by Lyubarskii (1997), where the variability is caused by fluctuations of the accretion flow throughout the disc, that couple together as they propagate inward, can reproduce the linear and non-linear properties of at least the flux variability of AGN. This model is very promising as a general approach, the challenge now remains to understand physically how these fluctuations can be generated and further propagated through the accretion flow and to study the detailed dependence of the PSD and lag spectra on the accretion flow parameters. This issue will be discussed in more detail in Chapter 4.

1.3 Statistical Tools

It can be easily seen, by looking at AGN light curves, that the X-ray flux is usually variable and the variability pattern may contain several structures. To be able to use this information to build physical models it is necessary to extract more *quantitative* information. Several statistical tools have been developed or adapted to recover accurate information from the temporal structure of AGN light curves. Here we will describe the most common techniques, which are also used in the analyses presented in the following chapters.

Variability Amplitude

The first question that arises when dealing with a variable signal is *how variable is it?* A simple quantitative estimate of the amplitude of the variability is given by the variance S^2. For a continuous signal $x(t)$ sampled at discrete time intervals t_i, the variance can be estimated as

$$S^2 = \frac{1}{N-1} \sum_{i=1}^{N} (x(t_i) - \bar{x})^2, \tag{1.2}$$

where N is the number of points sampled and $\bar{x}$ is the average value of the count rate. The definitions and normalisations used in this section follow Press et al. (1992).

However, astronomical data is affected to varying degrees by Poisson noise, caused by the finite number of photons collected in each time interval. This causes the value of S^2 to be an overestimation of the intrinsic variance of the source. To solve this problem, it is common practice to subtract the contribution to the variance expected from Poisson noise, $\sigma_{\rm err}^2$, which can be easily calculated knowing the number of counts in each time bin. Then, the root mean square (rms) amplitude of variability used in X-ray timing analyses is given by:

$$\sigma_{\rm rms} = \sqrt{S^2 - \overline{\sigma_{\rm err}^2}}, \tag{1.3}$$

where $\overline{\sigma_{\rm err}^2}$ is the value of $\sigma_{\rm err}^2$ averaged over all time bins.

Finally, as this variability amplitude depends on the actual count rate of the source through the dependence of S^2 on $x(t)$, the fractional rms amplitude, $F_{\rm var} = \sigma_{\rm rms}/\bar{x}$, is sometimes used. This dimensionless quantity represents the variability amplitude normalised by the source's mean count rate and is used to compare the variability of sources with different luminosities.

Power Spectral Density

The next step is to characterise the power spectral density (PSD) of the light curve, that is, how the variability power is distributed among different Fourier frequencies. As the data is a discrete sequence of N points, the Fourier transform can only be estimated for $N/2$ positive frequencies and it is normally done using the Discrete Fourier Transform (DFT) method. For this, the Fourier Transform is calculated for a discrete set of frequencies f_i sampled uniformly at intervals of $1/\Delta T$ between $1/N\Delta T$ and the Nyquist frequency $1/2\Delta T$, where ΔT is the length of the time bins. The real and imaginary parts of the DFT of $x(t_i)$, R_X and I_X, are given by:

$$R_X(f_j) \quad = \quad \left(\frac{\Delta T}{N}\right)^{1/2} \sum_{i=1}^{N} x(t_i) \cos(2\pi f_j t_i)$$

$$I_X(f_j) \quad = \quad \left(\frac{\Delta T}{N}\right)^{1/2} \sum_{i=1}^{N} x(t_i)\sin(2\pi f_j t_i). \tag{1.4}$$

The normalisation constants $(\Delta T/N)^{1/2}$ make the amplitudes independent of the length and sampling of the light curve. The variability power density in each frequency bin, $|X(f_i)|^2$ is the modulus squared of the Discrete Fourier Transform:

$$|X(f_j)|^2 = X^*(f_j)X(f_j) = R_X(f_j)^2 + I_X(f_j)^2, \tag{1.5}$$

which is then normalised by the count rate to obtain the *periodogram* $P(f_j)$ (Priestley, 1981)

$$P(f_j) = \frac{2}{\bar{x}^2}|X(f_j)|^2. \tag{1.6}$$

With this normalisation, the integrated periodogram between f_1 and f_2 gives the contribution of this Fourier frequency range to the total fractional variance squared, F_{var}^2.

The periodogram gives an estimate of the underlying PSD of the light curve. For AGN X-ray light curves it normally shows a power-law dependence on frequency, with power decreasing with increasing frequency. The power-law index is a usual measure that characterises the variability of a source. Further features such as changes in slope (breaks) in the power spectrum indicate characteristic frequencies in the system and the presence of periodic or quasi-periodic signals would appear as peaks in the periodogram at the corresponding frequencies.

Structure Function

The periodogram is a very useful tool to characterise the variability but it is not always possible to apply this method. As it recurs to the Fourier Transform of the light curve, if the sampling is very sparse or uneven the distorting effects of the windowing function can make it impossible to discern the real structure of the light curve. In cases of light curves with poor time sampling, astronomers can resort to the Structure Function (SF) defined in Simonetti et al. (1988). The SF contains, in principle, the same information as the periodogram and, as it is calculated, in the time domain, does not suffer large distortions due to the sampling pattern.

Formally, the first order SF is defined by

$$SF(\tau) = \frac{1}{N(\tau)} \sum_{i=1}^{N} w(t_i)w(t_i+\tau)[x(t_i+\tau) - x(t_i)]^2 \tag{1.7}$$

where τ is the so called *time lag.* The SF function gives an estimate of the strength of the correlation between two points in the light curves separated in time by τ. The weighting function $w(t_i) = 1$ when the data point $x(t_i)$ exists and $w(t_i) = 0$ when it does not so that $N(\tau) = \sum_{i=1}^{N} w(t_i)w(t_i + \tau)$ is the total number of points in the sum of $SF(\tau)$. Since the contribution of points in the time series that have no measurement is annulled, gaps in the data set are naturally excluded from the analysis.

The SF of this kind of light curves is also a power law, with SF value increasing with increasing time scale. Plateaus and turnovers in the curve represent time scale ranges where the variability ceases to be correlated and dips in the SF indicate periodicities in the light curve.

Correlation Functions

It is sometimes interesting to explore the *correlation* between two light curves in, for example, two different energy bands. The correlation function describes how well the variability of two light curves match. It is normally defined as a function of time lag τ, so if the correlation function reaches a maximum value at $\tau = \tau_0$, it means that the two light curves are best matched when one of them is displaced in the time axis by τ_0. This analysis is therefore useful to measure the time it takes one emitting region to respond to the changes in another region in cases where their variations are connected by a transfer function. The Discrete Correlation Function (DCF) method of Edelson & Krolik (1988) is widely used to estimate the correlation between two astronomical time series, as it can handle differently sampled light curves without resorting to interpolation of the data. In this method, the unbinned DCF (UDCF) is first computed using all and only existing data points $x(t_i)$ and $y(t_j)$ in the time series:

$$\mathrm{UDCF_{ij}} = \frac{(\mathrm{x(t_i)} - \bar{\mathrm{x}})(\mathrm{y(t_j)} - \bar{\mathrm{y}})}{\sqrt{(\sigma_{\mathrm{x}}^2 - \mathrm{e_x^2})(\sigma_{\mathrm{y}}^2 - \mathrm{e_y^2})}}, \tag{1.8}$$

where e_x^2 is the mean error squared of the data points in the light curve $x(t)$. It is necessary to subtract these observational errors from the variances σ^2 to keep the correct normalisation. Then the UDCF is binned in time lag with bin size $\Delta\tau$ so that pairs of points having $\Delta t_{ij} = t_j - t_i$ in the range $\tau - \Delta\tau/2 \leq \Delta t_{ij} < \tau + \Delta\tau/2$ are added to produce DCF(τ),

$$\mathrm{DCF}(\tau) = \frac{1}{M} \sum_{i=1}^{M} \mathrm{UDCF}_{ij}, \tag{1.9}$$

where M is the number of points in the time lag bin.

Cross Spectrum

The usual correlation functions calculated in time domain do not distinguish between the different frequency components that compose each light curve. Therefore, the values obtained for the correlation coefficient and time lags are only representative of the most significant flux changes, which tend to correspond only to the low Fourier frequency fluctuations. When the quality of the data is sufficiently good, it is possible to calculate Fourier-frequency resolved correlations functions. These are useful to disentangle signals at different Fourier frequencies in the light curves, that might show different correlated behaviours.

The Cross Spectrum $C(f)$ is analogous to the power spectrum but this time calculated with two different light curves, $x(t)$ and $y(t)$, as

$$C(f) = X^*(f)Y(f) = |X(f)||Y(f)|e^{i(\phi_y(f)-\phi_x(f))} \tag{1.10}$$

where $X(f)$ is the modulus of the Fourier transform of $x(t)$ and $\phi_x(f)$ is the corresponding phase.

The Cross Spectrum is a complex valued function, giving information on the coherence between the light curves and their phase lags, as a function of Fourier frequency. The coherence, γ^2, is proportional to the modulus of the average of an ensemble of Cross spectrum estimates:

$$\gamma^2(f) = \frac{|\langle C(f)\rangle|^2}{\langle |X(f)|^2\rangle\langle |Y(f)|^2\rangle}, \tag{1.11}$$

and has a value of $\gamma^2(f_j) = 1$ when the light curves are perfectly correlated at frequency f_j and a value of $\gamma^2(f_j) = 0$ when they are completely uncorrelated. For well correlated light curves it makes sense to calculate the phase lag, $\phi(f_i)$, between them,

$$\phi(f_j) = \arg\{\langle C(f_j)\rangle\} = \arctan\left\{\frac{\langle I_C(f_j)\rangle}{\langle R_C(f_j)\rangle}\right\}. \tag{1.12}$$

From this relation we obtain the time lags, $\tau(f)_j$, where now τ is a function of Fourier frequency, that measures the time delay between corresponding fluctuations in both light curves,

$$\tau(f_j) = \phi(f_j)/2\pi f_j. \tag{1.13}$$

1.3.1 Scatter and Significance, Tests with Artificial Data

As noted in the previous section, X-ray light curves of AGN have PSDs characteristic of red-noise processes. It is crucial to account for this red-noise nature when estimating any statistical quantity of these light curves as, as we will see, they are characterised by large inherent scatter. The effects that the red-noise nature of the light curves has on the different variability measures often depends on the particular realisation of the light curves and is not simply predictable. An easy way to study what to expect from the behaviour of the statistical tools described above is to test them with artificial time series of known properties.

In a stochastic red-noise process, the mean of the periodogram at a given frequency is distributed around the underlying PSD value as a Gaussian distribution with two degrees of freedom (χ^2_2). The mean and standard deviation of the distribution are equal to the PSD (see Timmer & König, 1995, for a simple derivation) so that there is an inherent scatter of 100% in the periodogram values, completely unrelated to any observational noise. This fact has important implications for the identification of periodicities in the data, as well as for the significance estimation of correlations and even for the determination of basic quantities such as the mean and variance of the light curves. This last point was studied in detail by Vaughan et al. (2003b) who pointed out that the mean and variance of a stretch of a red noise light curve depends strongly on the value of the periodogram at the lowest Fourier frequencies, where the variability power is usually highest. As the periodogram values have a large scatter, these few points can produce large differences in the mean and variance, so a change in these values, within a range, is expected and does not imply changes in the process producing the variability. Therefore, non-stationarity in the light curve cannot be claimed simply from changes in the first two statistical moments of the variability.

The usual solution to this problem is to use simulated light curves with the same basic statistical properties as the observed data, to estimate the expected scatter of its statistical moments. These artificial data must account for the stochastic nature of the red-noise light curves. As noted by Timmer & König (1995), a way to construct such light curves is to randomise *both* the phase and the amplitude of the data in Fourier space. The randomisation of the amplitudes is required to produce all possible light curves correspondent to the assumed underlying PSD shape. Their method consists of drawing two Gaussian distributed random numbers and multiply them by half the square root of the underlying PSD, for each Fourier frequency sampled. These numbers are then used as the real and imaginary parts of the Fourier Transform of the artificial data. In this way, the resulting light curve periodogram values follow a χ^2_2 distribution around the underlying PSD values, with the required standard deviation. The light curve is then obtained simply through the inverse Fourier Transform of this periodogram. It can then be scaled and clipped to match the count rate and sampling of the real data.

Before these light curves can be used to compare with the real data it is necessary to account for the effects of observational noise and sampling. Poisson noise has the net effect of adding a constant value to the periodogram at all frequencies, or equivalently a Poisson deviate at each point in the light curve. The way to deal with this effect depends on the quantities to be tested. If the aim is to fit a PSD model to the periodogram, then a constant value (equal to $2/N$) should be added to the *model* at each frequency (see Uttley, M^{c}Hardy & Papadakis 2002 for PSD model fitting methods). Alternatively, if quantities such as mean and variance are to be calculated then it is easier to add a Poisson deviate to the simulated light curves.

The sampling of the light curve has two main effects on the periodogram, *red noise leak* and *aliasing*. Red-noise leak appears in cases where the light curve has significant variability power below the smallest frequency probed. This means that the observed segment of the light curve will show marked rising or falling trends. In other words, the low frequency power leaks into the probed frequency band, altering the shape of the measured periodogram. One way to reduce this effect is to de-trend the observed light curve to eliminate the long term variability. Another method is to produce artificial light curves much longer than the observed ones, effectively introducing low frequency fluctuations, and then clip them to the required lengths. In this way the surrogates will suffer from red-noise leak (on average) by the same amount as the real data. Secondly, the effect of aliasing arises when the observed light curve is variable at frequencies above the Nyquist frequency. These higher frequencies cannot be probed and they pass as lower frequency fluctuations into the observed band, their power is completely absorbed by their 'alias' frequencies. To include this effect in the artificial light curves, they should be produced in much finer time sampling than the real data, introducing variability power up to a higher Nyquist frequency. Then these surrogates can be binned, so that their periodograms include the distortions due to aliasing.

As noted before, the periodogram of red-noise light curves have an intrinsic scatter of 100% the value of the underlying PSD. This is particularly problematic when searching for periodicities in the light curve since a spurious peak in the periodogram can easily be interpreted as a real periodicity peak. This problem is inherent to the stochastic nature of the data and so also affects other methods that search for periodic signals, such as epoch folding. Therefore it is essential to provide accurate significance estimates to the peaks in the periodogram.

Benlloch et al. (2001) propose a method to estimate the significance using simulated light curves generated as described above. The periodograms of these artificial data are computed to see how often does a similar peak appear in (by construction) aperiodic data. This gives an idea of the certainty with which the periodicity can be claimed. The only caveat of these methods is the uncertainty in the underlying PSD parameters used to generate the light curves, as this information is usually only partially known. However, it is always possible to perform the same test with different input PSD parameters, within acceptable ranges. These tests tend to give consistent results and provide a more robust significance estimate.

A similar phenomenon appears in the correlation functions. The problem here arises because, in a red noise light curve, consecutive time bins are highly correlated. The error of the DCF is given by

$$\sigma_{\mathrm{DCF}}(\tau) = \frac{1}{\sqrt{(M-1)(M'-1)}} \left\{ \sum [\mathrm{UDCF_{ij}} - \mathrm{DCF}(\tau)]^2 \right\}^{1/2} \tag{1.14}$$

where M is the number of points in the time lag bin and M' is the number of *uncorrelated* points in the same bin. To estimate this errors accurately using this formula it must be possible to know how many uncorrelated points contribute to the sum.

As noted by e.g. Uttley et al. (2003), the effective number of uncorrelated points depends on the sampling and on the PSD of the light curves and cannot be directly calculated. The significance of a peak in the correlation function between two red-noise light curves can again be estimated using simulations. The algorithm consists of producing a large set of uncorrelated pairs of simulated data with the PSD parameters of the observed light curves. Then a correlation function is calculated for each pair and the value of their highest correlation peaks are recorded. A confidence value can then be attributed to the observed correlation peak by noting how often a similar or higher peak is found by chance in uncorrelated data of similar characteristics.

Finally, the strong correlation of consecutive points in the time domain also has implications for the Structure Function. As a result of the point-to-point coupling in the data, consecutive lag bins in the SF are also highly correlated. The main effect in the appearance of the SF is that it produces *smooth* fluctuations, which tend to be confused with real structure in the data.

A second point is that the SF is used for light curves heavily affected by gaps, because it suffers less from the effects of sampling than the periodogram. Although this is true, the accuracy of the SF analysis is often overestimated and this can be exposed through the use of simulations. Fig. 1.3 shows the SF calculated for four realisations of the same red-noise process. A fifth light curve of length ∼ 10 times greater is used for comparison and produces the SF extending up to the longest time lags in this figure. As can be clearly seen, the SF does not reproduce the same power-law behaviour for the different realisations, allowing for a noticeable error in the determination of the slope. Secondly, all the 'structure' seen in the last 1.5 orders of magnitude in the lag axis are completely spurious as they have not been included in the construction of the light curves and do not appear in the SF of one of these light curves calculated to a longer length.

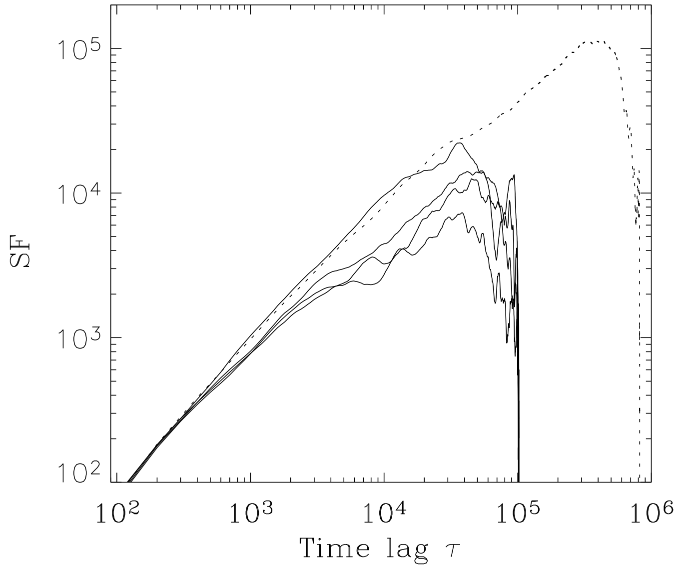

Figure 1.3: SF of four short realisations of an artificial red-noise light curve (solid lines) and one long light curve (dashed line). The SF recovers the correct slope only for small time lags, for longer time lags the slope depends strongly on the particular realisation. In addition, spurious structure appears in the last 1.5 order of magnitude of the time lags, noticeable when comparing to the SF of a longer realisation of the same process.

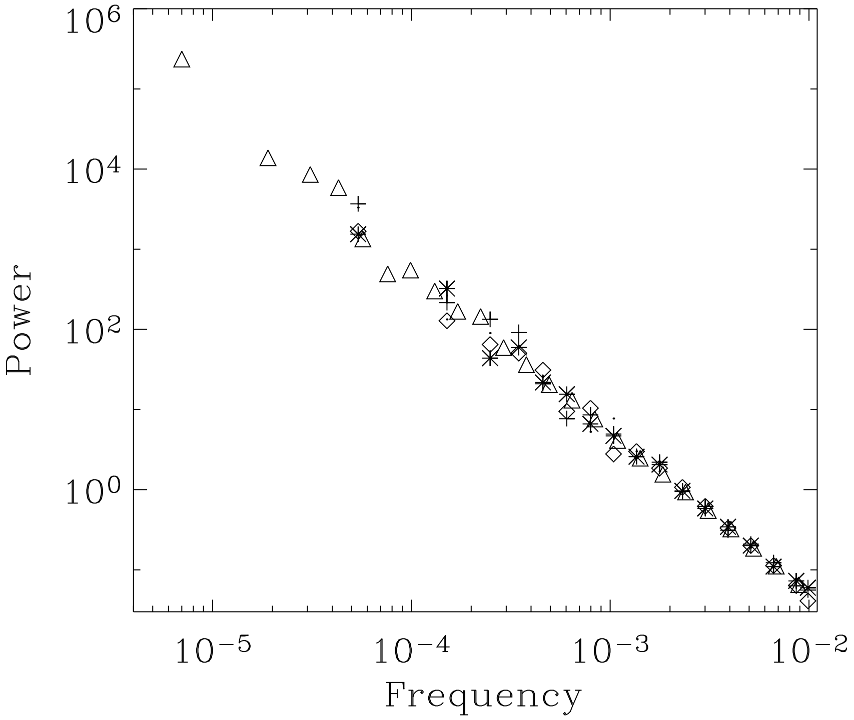

Figure 1.4: Binned periodograms of the same five light curves as in Fig. 1.3. The PSDs of the long light curve is represented by triangles, all other symbols correspond to the four short light curve segments. The power law PSD shape is recovered accurately and only small spurious structures can be observed.

Figure 1.4 shows the periodograms for the same five light curves, where the triangles correspond to the long light curve. As is apparent from this plot, the *binned* periodograms estimate the spectral slope consistently. One last point that must be considered when using the SF analysis is that the sampling of the data does affect the observed structures. Fig. 1.5 shows the periodograms of two continuous light curves as dashed lines and, overlaid, the periodograms of the same light curves sampled with observations and gaps of equal length at regular intervals. The overall structure of the particular SF is recovered but numerous spurious peaks and dips appear at the sampling time scale and its multiples. The precise structure of these features depends on the actual realisation of the light curve and thus cannot be simply 'deconvolved' by knowing the sampling pattern. Uneven sampling or larger gaps complicate this problem further. The SF remains the best option to analyse light curves with numerous gaps, but it should be complemented with tests with artificial light curves to estimate the real significance of the structures observed.

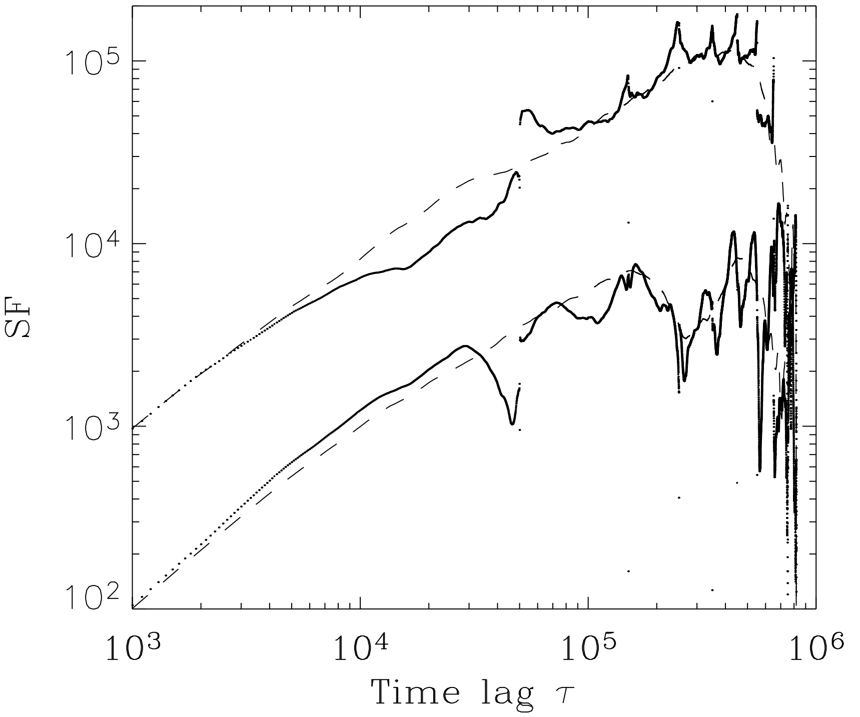

Figure 1.5: SF of two continuous red-noise light curves in dashed lines and the corresponding SF of these light curves sampled at regular intervals of data and gaps, overlaid in solid lines. The sampling pattern distorts the structure function producing structure at a time lag corresponding to the sampling cycle and its multiples.

1.4 Research Topics

The variability observed in AGN light curves and spectra can be used in several ways to extract information on the physical system. Here we outline a few possible research approaches and introduce subsequent chapters.

1.4.1 Simultaneous Flux/Spectral Variability

Spectral variability can be an indication of physical changes in the emitting region. In particular, for the X-ray spectrum of AGN, changes in the slope can reflect a varying temperature and/or optical depth of the Comptonising corona. It is expected that such changes will also be related to the observed flux level. For example, if the general accretion disc/corona model is correct, then an increase in the disc flux will produce more seed photons that will be Comptonised by the corona, which then looses energy more rapidly and cools down, producing a steeper energy spectrum. Conversely, a decrease in the disc flux will lead to a harder spectrum. There are, however, many more ways in which the spectrum and flux can be connected, even within the same scenario, e.g. an increase in the accretion rate will produce more disc seed photons but at the same time direct more power into heating the corona through magnetic reconnection and, depending on the details of the process, the dependence of spectral slope on flux can be much more complex. Alternatively, a change in accretion rate can produce a different level of evaporation of the disc, changing the optical depth of the corona.

In principle, continuous monitoring of flux and spectral slope in the X-ray regime can constrain the relation between the accretion disc and corona but, generally, the available data is not sufficient to produce a clear picture. Some progress can be made, however, by searching for correlated variability and confronting the results with general model predictions. In this spirit, we analyze the flux variability on different time scales and the energy spectral changes of the NLS1 PKS 0558-504 in Chapter 2.

1.4.2 Correlated Variability Between Energy Bands

AGN are variable throughout the energy spectrum. Given that the characterisation of the variability properties puts constraints on the physical conditions of the emitter, this can be used to study the separate structures that compose the AGN. It is expected, however, that the different regions will be somehow connected so additional information can be extracted from the *correlations* between different energy bands.

The choice of the pair of energy bands to be correlated depends on the emission mechanism we want to study. In radio quiet objects, the natural emission mechanism for the Optical/UV is thermal emission from the accretion disc and Compton up-scattering of seed photons through a corona of hot electrons for the X-rays. These two regions can be strongly coupled as the disc emission is a likely source of seed photons for Comptonisation and because, in turn, the X-rays produced by the corona shine on the disc, affecting its luminosity and spectrum. The correlation between Optical/UV and X-ray bands will probe the connection between the thermal disc and the Comptonising corona: The relative amplitude of variability in each band marks the maximum influence one emitting region has on the other and possible time lags between the energy bands constrain the size of the regions and the speed of propagation of the fluctuations.

The importance of the search for correlated variability has been recognised by a few research groups that have conducted dedicated observational campaigns. The results of these campaigns have yielded some significant correlations in a variety of time scales, showing different time lag and variability amplitude behaviours. These positive results prove the power of this approach but also mark the necessity to conduct more studies of this kind to disentangle the effects that a few main parameters (i.e. black hole mass, accretion rate, observed energy bands) have on the observed correlations. In Chapter 3 we present a short time-scale study of the NLS1 MCG-6-30-15 observed simultaneously in the U and X-ray bands.

1.4.3 A Phenomenological Model for the Flux Variability

A main aim of AGN research is to construct a complete physical model that can predict self-consistently all the observed characteristics of luminosity, energy spectrum and temporal variability of these objects. We are however very far from achieving this goal. Given the complexity of the problem, present developments must rely on studies restricted mainly to one aspect of the problem, i.e. generation of X-ray emission with the appropriate spectrum, prediction of spectral changes through dynamical evolution of emitting regions, creation and evolution of accretion disc instabilities, etc. The hope is then that these separate theories can be ultimately united to produce a complete picture.

It is important to notice, when dealing with variability models, that the source of the *variability* is not necessarily the same as the source of *emission*. In other words, the emitting region can be subjected to changing physical conditions, governed by external factors, which affect the flux output. In tis case, it is these external factors that produce the variability, not the particular mechanism of emission. It is possible to make progress by constructing phenomenological models that deal purely with the variability, for example, by modelling the creation and propagation of fluctuations that then modulate the X-ray emission. This approach produces simple models that can be probed without prohibitively long numerical calculations and has not been exploited to the levels permitted by existing observational data. For example, accretion rate fluctuations in the disc can produce fluctuations of the optical flux arising from viscous dissipation as much as they can affect the heating rate of the corona and, with it, the X-ray flux. In this case it is the accretion rate fluctuations that produce the variability and so it is this process that should be modelled to match the observed variability properties. In Chapter 4 we present a model based on the idea of Lyubarskii (1997) that the variability is caused by accretion rate fluctuations, produced on the local viscous time-scale throughout the disc, that propagate towards the centre. This simple configuration was initially proposed to reproduce the PSD slope in a natural way and was later shown to reproduce the $\sigma_{\rm rms}$-flux relation as well. Combining Lyubarskii's paradigm with assumptions about the radial emissivity profiles for different energy bands, the high coherence and Fourier-frequency dependent time lags can also be reproduced. We will study the dependence of the variability properties on different parameters and configurations and compare them with the available data.

Chapter 2

X-ray variability of the NLS1 PKS 0558–504

W. Brinkmann, P. Arévalo, M. Gliozzi, & E. Ferrero

Astron.Astrophys. 415 (2004) 959-969

2.1 Abstract

We present results from several XMM-Newton observations of the radio-loud Narrow-line Seyfert 1 galaxy (NLS1) PKS 0558-504. We find evidence for strong and persistent X-ray variability, both on short and long time-scales. On short time scales of $\gtrsim 2$ hours the source varies smoothly by 15-20%; long-term variations by a factor 2 could not be resolved in the relatively short exposures: we find the source mostly in a 'low' state, in 2 out of the 11 observations in a 'high' state. X-ray flares seem to be recurrent with a time scale of ~ 24 ks which, if interpreted as the Keplerian time scale in the disc, would place the emission region just outside the last stable orbit. The X-ray spectrum of PKS 0558-504 can be well fitted by two Comptonization components, one at moderate temperatures of kT $\sim$ 4.5 keV and optical depths of $\tau \sim 2$, the other at high temperatures (kT $\sim$ 50 keV) and low optical depths ($\tau \sim 1.0$). These parameters are, however, subject to large errors due to the inherent degeneracy of the Comptonization models. Flux variations of the source are caused by changes of the colder component only, the hot component with parameters very similar to those of BLS1 galaxies, stays constant. All results fit nicely the picture that NLS1 galaxies are lower mass objects, accreting close to the Eddington rate emitting X-rays from a very active magnetically powered accretion disc corona.

2.2 Introduction

Narrow-line Seyfert 1 galaxies are optically identified by their emission line properties: the ratio [O III]/Hβ is less than 3 and the FWHM Hβ less than 2000 km s^{-1} (Osterbrock & Pogge 1985, Goodrich 1989). Their spectra are further characterized by the presence of strong permitted Fe II, Ca II, and O I λ 8446 ionization lines (Persson 1988). NLS1 are seldom radio loud (Ulvestad et al. 1995, Siebert et al. 1999, Grupe et al. 1999) and they are usually strong infrared emitters (Moran et al. 1996). In particular, NLS1 have been found to have extreme spectral and variability properties in soft X-rays (Boller et al. 1996, Brandt & Boller 1998, Boller et al. 2000), which might be related to an extreme value of a primary physical parameter, originating from the vicinity of a super-massive black hole.

PKS 0558-504 ($z = 0.137, m_{\rm B} = 14.97$) is one of the very few radio-loud NLS1 galaxies ($R_{\rm L} = f_{\rm 5GHz}/f_{\rm B} \simeq 27$, Siebert et al. 1999). It was optically identified on the basis of X-ray positions from the High Energy Astronomy Observatory (HEAO-1, Remillard et al. 1986). The Ginga observations (Remillard et al. 1991) showed an increase in the X-ray flux by 67% in 3 minutes, implying that the apparent luminosity must be enhanced by relativistic beaming. Further X-ray observations with different satellites have confirmed the peculiar activity (e.g. strong variability, steep spectrum, high luminosity) of this source. Gliozzi et al. (2000) reported long-term variability from different X-ray observations corresponding to luminosities in the 0.1−2.4 keV soft X-ray band between 1.5×10^{45} erg s^{-1}and 5.4×10^{45}erg s^{-1}(for $H_0 = 50$ km s^{-1} Mpc^{-1}, $q_0 = 0.5$ and isotropic emission). The soft X-ray spectrum is rather steep ($\Gamma \sim 3.1$) and the medium energy power laws are considerably flatter ($\Gamma \sim 2$). Another peculiar property displayed by PKS 0558-504 is the unusually high X-ray to radio luminosity ratio (Brinkmann et al. 1997).

The six days long ROSAT All Sky Survey light curve of September 1990 and a series of pointed HRI observations (April 19 - 25, 1998) showed count rate variations by a factor of 2 in less than one day (Gliozzi et al. 2000). With the most extreme value of the luminosity variations found during the observations, $\Delta L/\Delta t = 1.12\times10^{42}$ erg s^{-2}, the straightforward application for an estimate of the lower limit of the radiative efficiency of $\eta > 4.8\times10^{-43}\Delta L/\Delta t$ (Fabian 1979) led to $\eta > 0.54$, which exceeds even the theoretical maximum for accretion onto a maximally rotating Kerr black hole. However, spectral variations and the extrapolation of steep power law spectra to low energies can lead to uncertain luminosities, as pointed out by Brandt et al. (1999).

Very dramatic flux variations by a factor of two in 33 min and, perhaps,

Table 2.1: XMM−Newton PN /RGS observations of PKS 0558−504

Orbit	Observing date (UT)	Instrument	Mode	Filter	Live time (ksec)	count rate (count/s)
30	Feb 07, 2000: 11:16-13:19	PN	FF	medium	5.93	13.3
32	Feb 10, 2000: 23:26-03:23	PN	FF	thin2	11.49	18.2
33	Feb 12, 2000: 23:13-04:41	PN	FF	thin2	16.22	17.07
	Feb 13, 2000: 12:33-17:04	PN	FF	thin1	13.34	12.41
	Feb 13, 2000: 18:29-22:59	PN	FF	thin2	13.30	13.74
42	Mar 02, 2000: 18:15-21:42	PN	FF	medium	10.93	26.0
45	Mar 07, 2000: 20:49-03:31	PN	SW	thin1	16.88	26.9
84	May 24, 2000: 13:04-16:54	PN	FF	medium	10.68	14.5
	17:21-21:08	PN	SW	medium	9.53	19.7
	06:19-13:16	RGS	SP	-	25.00	n/a
	13:16-22:13	RGS	SP	-	32.21	n/a
153	Oct 10, 2000: 01:49-04:47	PN	SW	thin1	7.50	18.8
	05:38-08:01	PN	FF	thin1	8.05	15.3
	01:27-08:46	RGS	SP	-	26.41	n/a
283	Jun 26, 2001: 03:21-06:36	PN	FF	medium	10.59	12.2
	02:37-06:43	RGS	SP	-	14.80	n/a
341	Oct 19, 2001: 12:41-15:51	PN	FF	medium	10.22	23.9
	11:55-15:59	RGS	SP	-	14.61	n/a

by 40% on a time scale as short as 2 min were reported by Wang et al. (2001) from ASCA observations on January 31, 2000 which leads to an even higher value of the radiative efficiency of $\eta = 0.9 \pm 0.2$.

PKS 0558−504 was observed repeatedly by XMM−Newton as a calibration and performance variation (PV) target. The XMM observations benefit from the high sensitivity of the instruments and the uninterrupted exposures resulting from the eccentric satellite orbit. O'Brien et al. (2001) published the spectral analysis of some preliminary data of the commissioning/CalPV phase. The 0.2−10 keV spectrum is dominated by a large soft X-ray excess, which shows no evidence for absorption or emission line features. A power law spectrum at higher energies ($E \geq 4$ keV) requires in the soft band additionally three black body components; the most physical explanation for the hot big blue bump is, however, Comptonization by a multiple temperature corona of an accretion disc.

Gliozzi et al. (2001) used data from the same observations for a study of the X-ray variability of the source. The long term light curve shows persistent variability with a tendency of the X-ray spectrum to harden when the count rate increases. The short term variability is characterized by smooth modulations with a typical time scale of ~ 2.2 hr and the most extreme count rate variations found imply a radiative efficiency slightly higher than the theoretical maximum for accretion onto a Schwarzschild black hole.

In this paper we present an analysis of XMM PN and RGS data taken so far in several observations between January 2000 and October 2001. The next section starts with the observational details and a temporal analysis of the data. Section 2.4 deals with the spectral variability of PKS 0558-504. In Section 2.5 we discuss the results in the framework of disc-corona accretion models for Seyfert galaxies and the last part contains a summary of the main conclusions.

2.3 Observations and temporal analysis

PKS 0558-504 was observed with the instruments on board XMM−Newton during 9 orbits between Jan 2000 and October 2001. As the source was a calibration target the exposures of the EPIC instruments were always relatively short and different instrument modes were used. For the following analyses we will rely only on data from the RGS instrument (den Herder et al. 2001) and from the PN camera (Strüder et al. 2001). Table 2.1 lists the relevant data of the observations. The RGS were always operated in spectroscopy mode (SP), the PN camera in Small Window (SW) or Full Frame (FF) mode, with either a thin or medium filter (for details of the XMM instruments see Ehle et al. 2001).

All PN data have been reprocessed using XMMSAS version 5.4. We selected photons with Pattern ≤ 4 (i.e. singles and doubles) and quality flag $= 0$. We calculated the 0.2−10 keV light curves for all observations by extracting the photons from a circular region centered on the source with a radius of 50". This extraction radius contains about 90 % of the source photons, using the encircled energy function given by Ghizzardi & Molendi (2001). We did not correct the light curves for the photon pile up which occurred in the central pixels of the point spread function when the detector was operated in FF mode and the source was in a bright state. It amounts to about $\sim 3\%$ and does not change the form of the light curve significantly. The backgrounds were determined with the same selection criteria from source free regions on the same chip and subtracted from the source light curves, which were binned in 400 sec bins.

For four of the orbits the reflection gratings (RGS) provided scientifically useful data simultaneously to the PN exposures. The RGS data was processed using the task *rgsproc* of the XMMSAS version 5.4. The light curves were constructed using the task *evselect*, selecting photons in the 0.3−2.0 keV energy band that belonged both to the source spatial region and the first order spectral region. The background light curves were calcu-

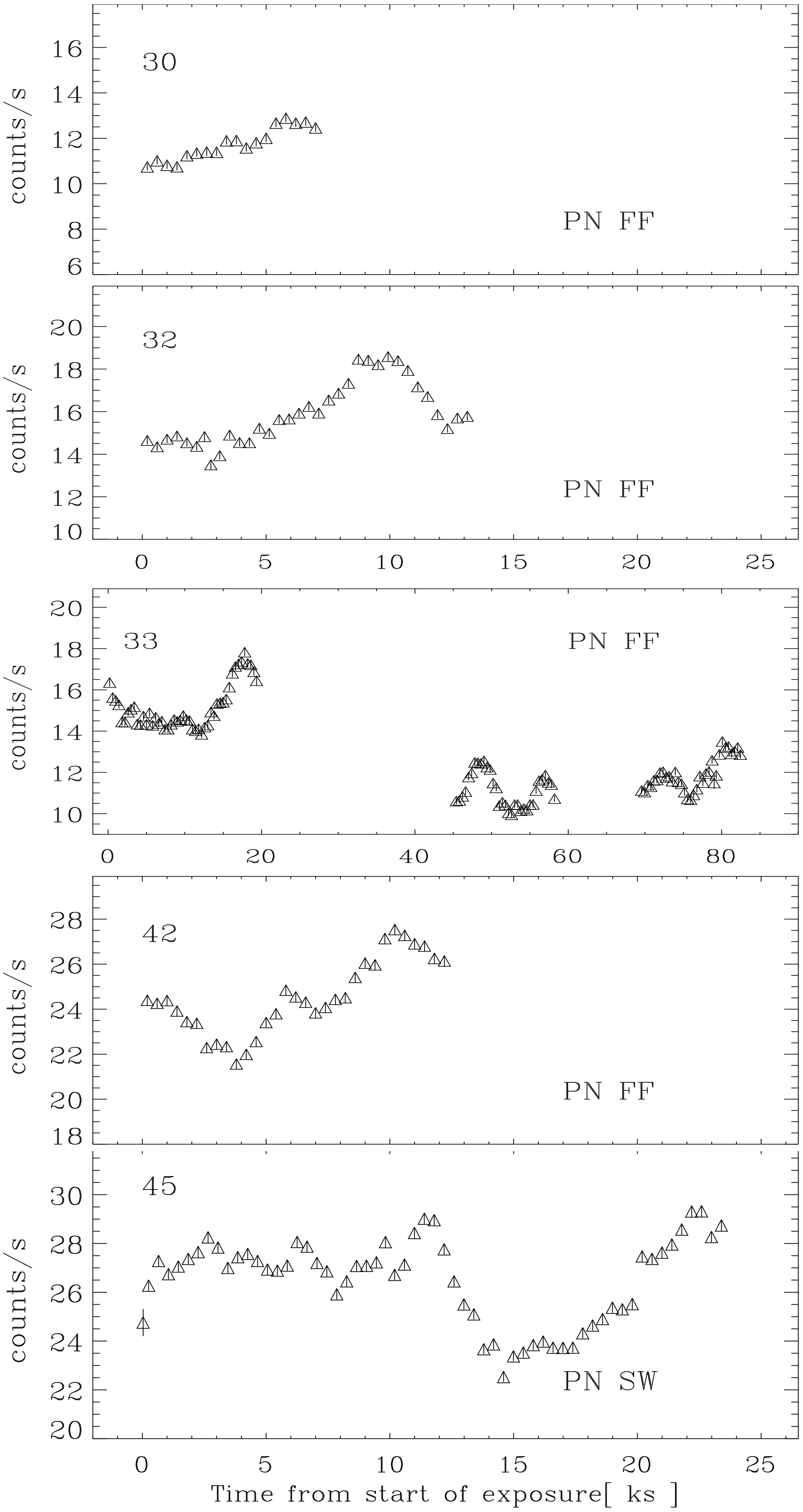

Figure 2.1: Light curves of PKS 0558-504 for the early orbits without RGS exposures. Triangles represent the PN data, with error bars smaller than the symbols. Note the longer time axis for orbit 33.

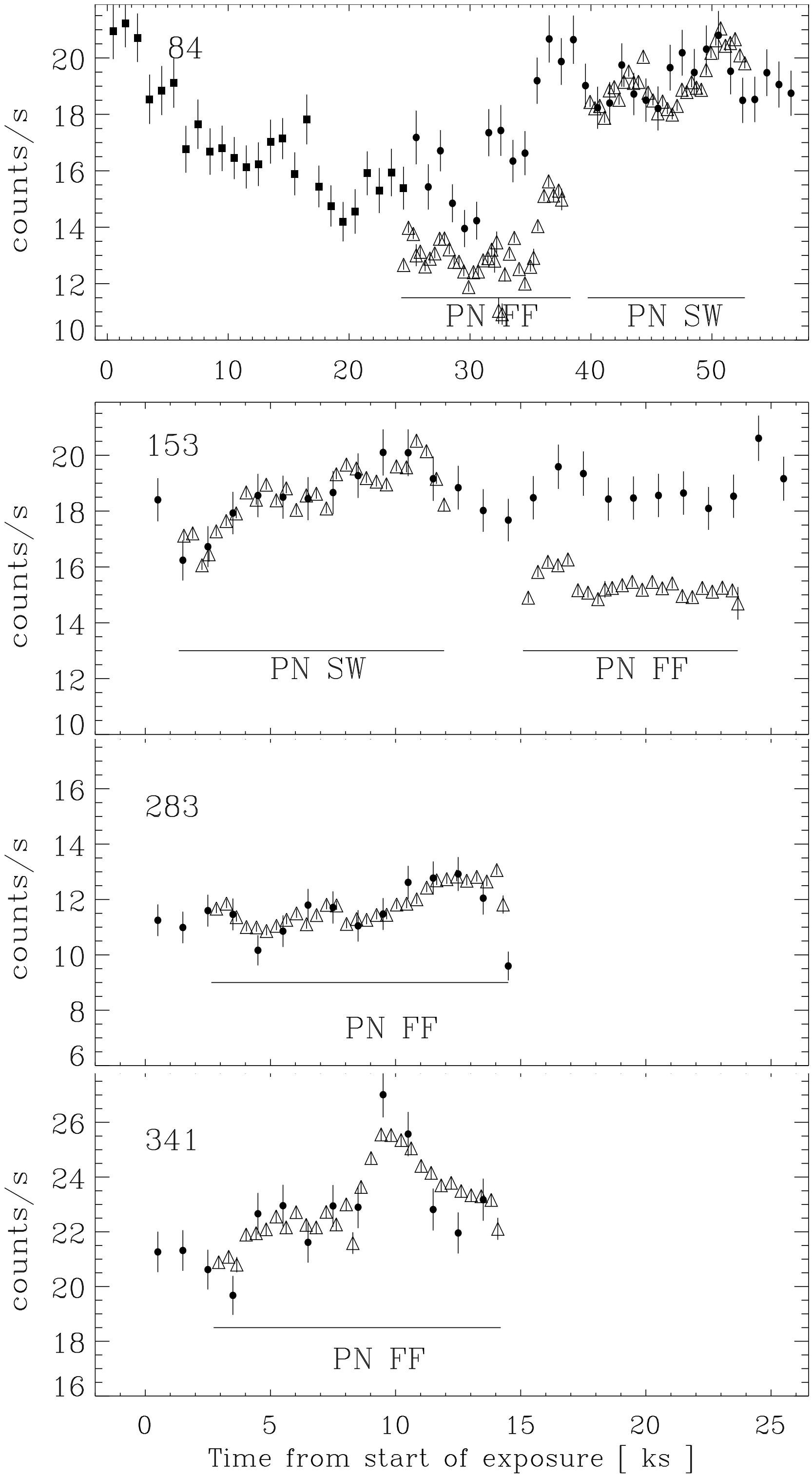

Figure 2.2: Light curves of PKS 0558-504 for the later orbits with RGS exposures. Triangles represent the PN data, with error bars smaller than the symbols. The dots represent the RGS light curves rescaled to match the PN SW count rate of the corresponding exposure. For orbit 84 the filled squares represent the first RGS exposure using both RGS detectors while for the second RGS exposure (dots) only the RGS 2 was available.

lated from all photons belonging to the first order spectral region and to the spatial region excluding the source. As the detector area used for the background is larger than the area of the source the background light curve had to be rescaled before being subtracted. The background subtracted source light curve was binned in 1000s bins to achieve a reasonable signal to noise ratio while preserving the overall shape of the curve.

The PN data is affected by the dead time of the detector that reduces the effective exposure by a factor of 0.9994 in the FF mode and 0.7101 in the SW mode. There is also a loss of counts due to the out-of-time events, the photons collected during the read out. This last effect further reduces the collection efficiency by a factor of 0.9328 in the FF and 0.9884 in the SW mode, respectively. The PN light curves were thus corrected for these two effects. The RGS light curves were scaled by a factor of ~ 12 in order to match them with the resulting PN SW count rates of the corresponding orbits. The plots in Fig. 2.1 show the PN light curves of early orbits for which no RGS observations were performed. In Fig. 2.2 we present the later PN observations with the scaled RGS light curves overlaid so that the times match. We used the same length for most of the time axes and the same range of count rates for a comparison of the variability pattern. Only orbit 33 and 84 had considerably longer exposures.

Clearly visible is a deficit of counts in the FF mode of $\sim 20\%$ when the RGS light curve is normalized to the SW mode data. This is an effect of photon pile up and a redistribution of double events into higher order event patterns (Freyberg, private comm). The correction factor to the RGS data is in this case of pattern migration of the order of ~ 15, but it is, as for the SW mode data, not the same for all orbits. It obviously does not only depend on the count rate and spectral variations but seems to be influenced by the level of background activity as well.

On long time scales (different orbits) the light curves show that the source undergoes intensity variations by a factor of $\gtrsim 2$. During the individual exposures we find substantial variability with an amplitude of up to $\sim 15{-}20\%$, which is not correlated with the average count rate of the observation. We never detected the large intensity variations in an individual exposure, thus the time scale must be longer than typically one orbit. Fig. 2.4 (see sect. 2.1) further suggests that the source exhibits some bi-modal behavior, being either in a high or a low state. The variances in the hard and soft band light curves are very similar; only in the highest intensity states the hard band light curves show stronger variations than the soft light curves.

The relatively smooth and nearly linear intensity changes have a time

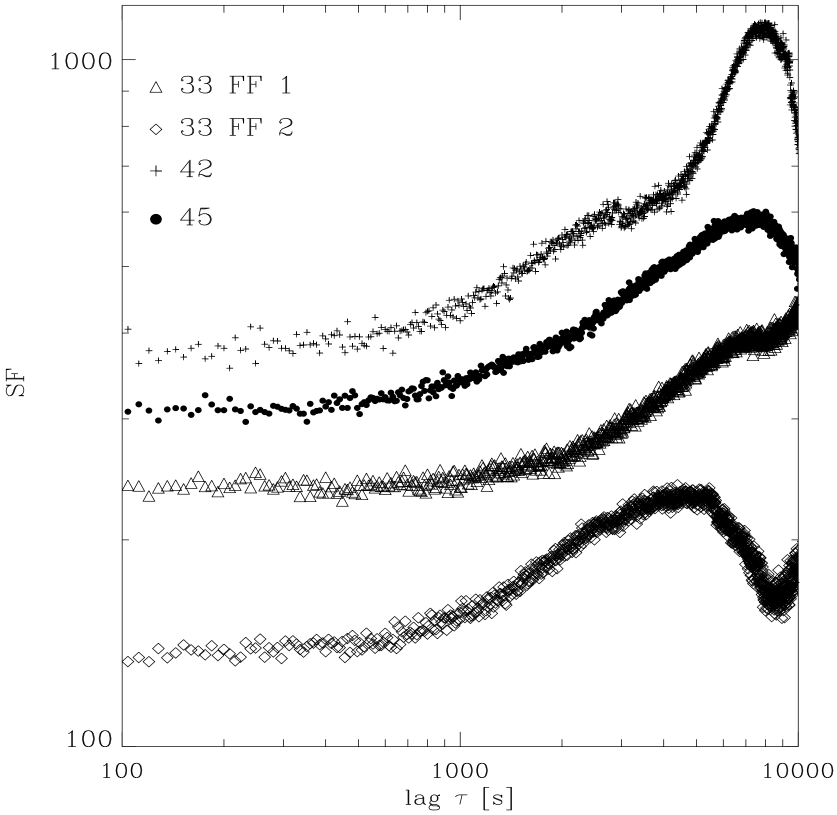

Figure 2.3: Structure functions of the LC of several orbits.The graphs are displaced arbitrarily in y-direction for clarity.

scale of typically $\gtrsim 2$ hours as can be seen directly from the light curves (Figs. 2.1 and 2.2). However, this is not a strict, well defined time scale as illustrated by the structure functions (Simonetti et al. 1985) of some individual orbits (Fig. 2.3). As already noted by Gliozzi et al. (2001) this time scale merely seems to reflect the typical rise/decay time scales in the light curves with a relatively narrow variance. But the light curves show as well that even the longest RGS exposure in orbit 84 is too short to cover all relevant time scales of the source.

The temporal structure of the intensity variations during different orbits show some intriguing similarities in shape and even in the amplitudes of the flux variations, independent of the average flux level. A temporal analysis of the whole data set, using orbit 32 as a template, shows a 'repetition rate' of that signal of ~ 23850 sec. The search was simply done by aligning the count rate peak of orbit 32 with the individual peaks of the other light curves. If the signal were strictly periodic we would expect this flare in 8 of the orbits but we find only 6 at the expected position. There are two exposures, orbits 153 and 283, when the source is in a low state, where no flare is found at the expected time. The statistical significance for this 'quasi-periodicity' would be rather high for purely random fluctuations, but lower for other models like shot-noise or self-organized criticality in the accretion disc (Mineshige et al. 1994). A rigorous statistical analysis to determine the significance of the existence of that signal, like the Monte Carlo technique developed by Uttley et al. (2002) turned out to be impossible, due to the underlying red noise process and, in particular, due to the extreme sparsity of the data, covering observations over more than two years. Longer observations are clearly required for definite results.

The most dramatic flux variations occurs near the middle of orbit 341 where the count rate changes by ~ 4.3 counts/s in ~ 1128 s. With the spectral parameters deduced below, assuming a Friedman cosmology with $\mathrm{H}_o = 75\ \mathrm{km\,s^{-1}Mpc^{-1}}$ and q_o=0.5, we obtain a $\Delta L_{0.2-10\mathrm{keV}}/\Delta t \sim 4.5 \times 10^{41}$ $\mathrm{erg\,s^{-2}}$. This leads to an upper limit of the radiative efficiency (Fabian 1979) of $\eta \sim 0.23$ which is similar to that found previously from ROSAT (Gliozzi et al. 2000) and XMM observations (O'Brien et al. 2001). These efficiency values are much more moderate than those claimed for the two flares detected by Ginga (Remillard et al. 1991) and Wang et al. (2001).

2.3.1 Hardness Ratios

We computed hardness ratios using 1000 sec binned soft and hard band light curves, and the expression, $HR = [4.0 - 10\ \mathrm{keV}]/[0.2 - 1.0\ \mathrm{keV}]$. The count rates in these energy bands appear to represent the two relatively independent spectral components of the source, as can be seen in Sec. 2.5. By plotting the HR as a function of the total count rate (0.2−10 keV), we are able to investigate whether the HR variations are correlated with the source flux.

The total count rates had to be corrected for the above mentioned deadtime effects as well as for pattern migration and pile up. From spectral simulations with typical source parameters (see sect. 3) we found that the hardness ratios change by about 0.01 comparing the thin filter observations with the medium filter data.

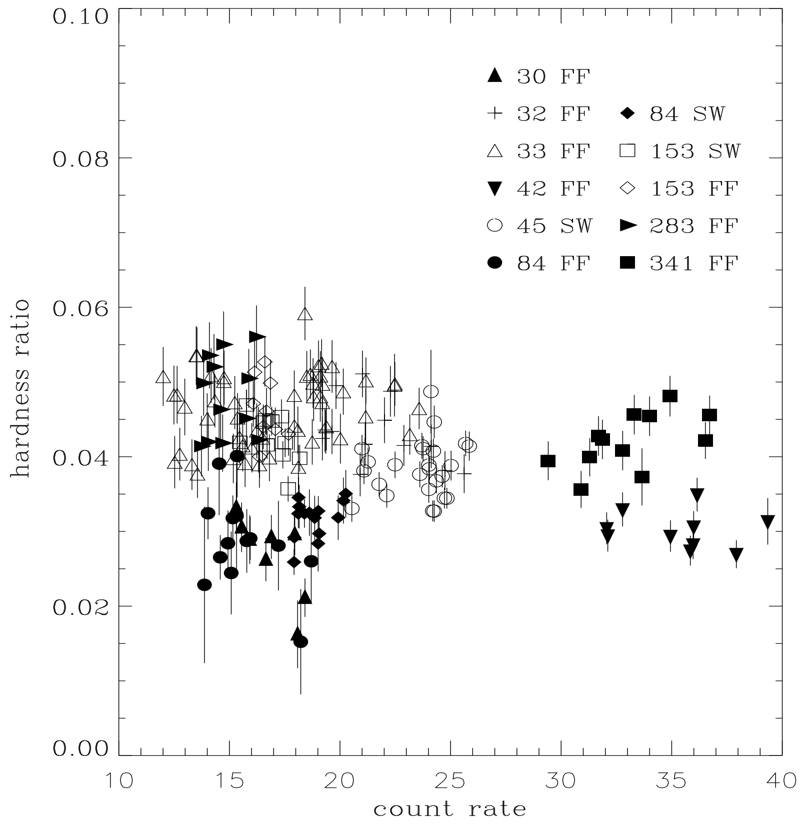

Figure 2.4: Hardness ratios as function of the total count rate for different orbits. Filled symbols denote observations with medium filter, open symbols with thin filters.

In Fig. 2.4 we plot the hardness ratios as function of the corrected 0.2−10 keV count rate for the different orbits. Filled symbols denote observations with medium filter, open symbols with thin filter. The count rates and hardness ratios are corrected to medium filter observations. Some data points with large errors are affected by flares in the background. We do not find a simple correlation between hardness ration and count rate as claimed by Gliozzi et al. (2001) from their restricted data base. The data suggest that the source can be predominantly found in a lower intensity state, differing by a factor of two in count rate from the high states. This reflects the scewed distribution of count rates found in other NLS1 as well. Whether the gap between these two states is real or a selection effect due to the limited observational coverage can only be decided in future observations. The hardness ratios show a large dispersion on long time scales, i.e. for different orbits. On the shorter time scales of a typical observation the hardness ratios in the low state appear to be nearly constant. There is a general slight tendency for the hardness ratios to get smaller with increasing count rate. In the high state orbit 341 there are strong indications of a hardening of the spectrum when the source brightens.

2.4 Spectral analysis

NLS1 galaxies are generally characterized by very steep spectra in the soft energy band (Boller et al. 1996). From *ROSAT* observations of PKS 0558–504 Gliozzi et al. (2000) find a steep power law with $\Gamma \sim 3$ in the $0.1-2.4$ keV energy range; in the *ASCA* $0.6-10$ keV band Vaughan et al. (1999) obtain $\Gamma = 2.26 \pm 0.03$. The XMM$-$Newton data (O'Brien et al. 2001) clearly show a strong soft excess below $\sim$2 keV over a harder power law at higher energies.

The PN data with their outstanding signal to noise ratio and their wide bandpass are ideally suited for a detailed spectral study of the source. For the spectral analysis we used the latest available response matrices (version 6.3) issued in December 2002. We extracted single and double events with quality flag = 0 from a rectangular region of 30×30 RAW pixels around the source position. The region includes $\sim 90\%$ of the source photons but avoids the gap between the detector chips. The background was taken on the same chip at distances as close to the source position as possible, avoiding contamination. With a count rate of $\gtrsim$ 20 counts s^{-1} in the high state the PN detector, operated in Full Window mode, showed strong indications of pile-up, clearly apparent from the XMMSAS task *epatplot*. We therefore discarded photons from the innermost (typically 2×3) RAW pixels at the core of the point spread function from the spectral analysis.

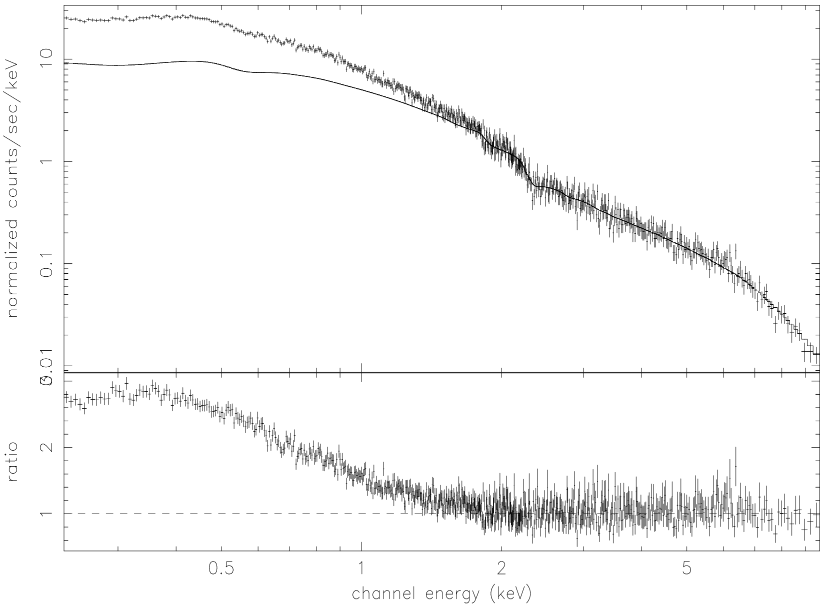

Figure 2.5: Power law fit with galactic absorption to the PN data for PKS 0558–504 in the 2 − 10 keV energy range; the fitted model is extrapolated to lower energies. The lower panel gives the ratio between data and model.

In Fig. 2.5 we show the power law fit in the 2−10 keV energy range to the data of orbit 153 ($\Gamma = 2.13 \pm 0.03; \chi^2_{\rm red} = 0.90/303$ d.o.f with a galactic $N_H = 4.4 \times 10^{20}$ cm^{-2}). The fitted model is extrapolated to lower energies and the ratio between data and model, given in the lower panel, clearly demonstrates the presence of a large soft X-ray excess over the hard power law. The spectrum of PKS 0558–504 appears to be a carbon copy of that of the NLS1 galaxy PG 0844+349 (Brinkmann et al. 2003) even with respect to the 'big blue bump' seen in both objects (O'Brien et al. 2001) and it is very similar to that of 1H 0419-577 (Page et al. 2002) and the other NLS1 galaxy Mrk 896 (Page et al. 2003) studied with XMM-Newton.

The upper limits given for an iron line are rather low (O'Brien et al. 2001) and the soft band spectral excess is far too broad to be fitted by a single black body component. A multiple blackbody (in the soft band) plus a power law at higher energies provides acceptable fits to the data, however, the physical nature of these different components remains obscure. Two power law models require absorption in excess of the galactic value and yield slightly worse fits. For example, for the above mentioned orbit 153 (see as well Table 2.2) we obtain an $N_H = 7.79 \times 10^{20}$ cm^{-2}, $\Gamma_{\rm soft} = 3.28 \pm 0.08$, $\Gamma_{\rm hard} = 1.62 \pm 0.10$ with a $\chi^2_{\rm red} = 1.163/578$ d.o.f., values which are representative for the other orbits as well.

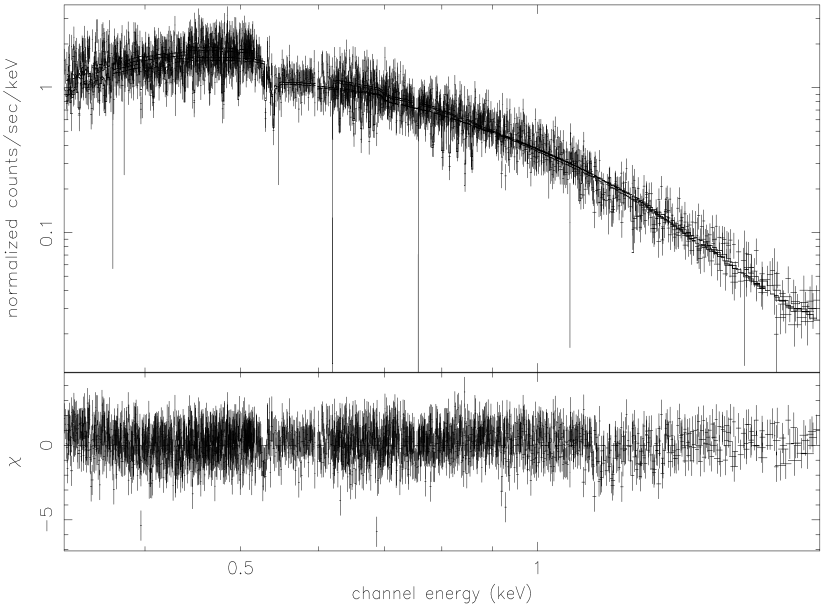

Figure 2.6: CompTT fit (without edge) with galactic absorption to the RGS1 data of orbit 84. The lower panel gives the $\Delta\chi^2$ per channel.

The relatively long RGS observation of orbit 84 provides a sufficient number of photons for an accurate fit. We have reprocessed the RGS data using XMMSAS version 5.3.3 and the RGS response matrices were created with the SAS package $rgsrmfgen$. The spectral data were binned to contain at least 30 photons per energy channel. We fitted the RGS data with a single *compTT* Comptonization model, available in $Xspec$ (Titarchuk 1994), assuming galactic absorption plus an additional high energy power law (see sect. 3.1). The fit is acceptable ($\chi^2_{\rm red} = 1.01/1162$ d.o.f) and yielded a temperature of the soft photons of $kT_0 = 63.9 \pm 5.0$ eV and an optical depth of $\tau = 2.47 \pm 0.25$. The temperature of the hot Comptonizing electrons was fixed at $kT_1 = 4.5$ keV to reduce the error bars (see the discussion below). An additional absorption edge, required only for one of the two observation intervals ($E_{\rm edge} = 1.14 \pm 0.02$ keV, $\tau = 0.27 \pm 0.06$) improves the fit significantly ($\chi^2_{\rm red} = 0.989/1158$ d.o.f) according to an F-test. The residuals

Table 2.2: Results from spectral fits of two−component Comptonization models assuming fixed Galactic $N_H = 4.4 \times 10^{20} cm^{-2}$, z=0.137

Orbit mode	kT_o (eV)	kT_1 (keV)	τ_1	$norm_1$	kT_2 (keV)	τ_2	$norm_2$	χ^2_{red}	dof
30 FF	$77.1^{+10.2}_{-10.2}$	$4.5^{+166.8}_{-4.5}$	$1.9^{+60.0}_{-1.9}$	1.30E-2	$47.3^{+2614}_{-47.3}$	$0.72^{+51.77}_{-0.72}$	1.90E-4	1.098	464
32 FF	$87.4^{+5.6}_{-5.6}$	$4.6^{+74.8}_{-4.6}$	$2.4^{+29.7}_{-2.4}$	1.21E-2	$61.8^{+3929}_{-61.8}$	$0.93^{+70.16}_{-0.93}$	0.98E-4	1.026	716
33 FF (1)	$84.8^{+5.1}_{-5.1}$	$4.4^{+68.4}_{-4.4}$	$2.3^{+27.5}_{-2.3}$	1.10E-2	$52.4^{+1960}_{-52.4}$	$0.77^{+36.66}_{-0.77}$	1.97E-4	1.039	823
33 FF (2)	$86.9^{+6.9}_{-6.9}$	$5.3^{+119.6}_{-5.3}$	$1.9^{+37.7}_{-1.9}$	0.71E-2	$60.2^{+2869}_{-60.2}$	$0.73^{+44.73}_{-0.73}$	0.96E-4	1.089	639
33 FF (3)	$82.8^{+7.4}_{-7.4}$	$5.3^{+138.3}_{-5.3}$	$1.8^{+42.0}_{-1.8}$	0.86E-2	$61.2^{+2144}_{-61.2}$	$0.63^{+29.34}_{-0.63}$	1.34E-4	1.088	663
42 FF	$86.7^{+5.3}_{-5.3}$	$4.5^{+68.38}_{-4.5}$	$2.4^{+27.8}_{-2.4}$	2.43E-2	$51.4^{+2502}_{-51.4}$	$0.60^{+40.15}_{-0.60}$	3.38E-4	1.029	757
45 SW	$74.7^{+6.2}_{-6.2}$	$4.8^{+103.8}_{-4.8}$	$1.9^{+35.7}_{-1.9}$	3.37E-2	$49.9^{+2282}_{-49.9}$	$1.08^{+55.46}_{-1.08}$	2.74E-4	1.002	909
84 FF	$78.8^{+17.4}_{-17.4}$	$4.5^{+241.3}_{-4.5}$	$1.7^{+84.0}_{-1.7}$	1.59E-2	$49.9^{+2782}_{-49.9}$	$0.59^{+45.27}_{-0.59}$	2.92E-4	0.957	415
84 SW	$73.4^{+11.8}_{-11.8}$	$4.6^{+187.5}_{-4.6}$	$1.8^{+65.9}_{-1.8}$	2.73E-2	$52.8^{+2659}_{-52.8}$	$0.72^{+46.16}_{-0.72}$	3.05E-4	1.029	485
153 FF	$87.3^{+8.8}_{-8.8}$	$4.5^{+112.3}_{-4.5}$	$2.0^{+42.5}_{-2.0}$	0.98E-2	$49.8^{+2440}_{-49.8}$	$0.72^{+46.25}_{-0.72}$	1.98E-4	1.067	576
153 SW	$77.0^{+7.8}_{-7.8}$	$4.7^{+119.7}_{-4.7}$	$1.9^{+42.1}_{-1.9}$	2.18E-2	$50.5^{+1974}_{-50.5}$	$0.79^{+38.96}_{-0.79}$	3.00E-4	0.974	656
283 FF	$87.8^{+10.1}_{-10.1}$	$5.2^{+184.5}_{-5.2}$	$1.7^{+55.3}_{-1.7}$	0.68E-2	$40.0^{+1135}_{-40.0}$	$0.83^{+29.74}_{-0.83}$	3.97E-4	1.119	695
341 FF	$93.1^{+6.5}_{-6.5}$	$5.0^{+122.8}_{-5.0}$	$2.1^{+42.6}_{-2.1}$	0.80E-2	$46.3^{+1073}_{-46.3}$	$0.51^{+13.86}_{-0.51}$	6.32E-4	1.108	792

NOTE: For orbits < 45 the lower threshold for the event amplitudes was different from the later setting. No extra response matrices exist for these early observations, but the spectral fits seem not to be affected noticeably.

shown in Fig. 2.6 are, however, smaller than the systematic differences between the two RGS detectors and no other strong absorption or emission features are observed.

We tried to determine the possible contribution of an iron line (neutral or ionized) to the spectra. To improve the signal to noise ratio we accumulated the data from different observation modes and filters and fitted first a power law and then a power law with a line to the combined SW and FF mode 4−9 keV data. As the accumulated spectra for the different modes covered different intensity states of the source, the normalizations of the spectra were different for the SW and FF mode data. For a neutral ion line we obtained equivalent widths of EW = 24 eV (SW) and 9.7 eV for the FF mode data ($\chi^2_{red} = 0.925$); for an ionized line we obtained EW = 31 eV (SW) and 45 eV for the FF-mode data ($\chi^2_{red} = 0.914$). In all fits the errors of the normalizations of the Gaussian lines were large and the inclusion of the lines did not improve the fits. The single power law model yielded already $\chi^2_{red} = 0.927$, thus the data do not require the presence of any iron emission line.

The featureless spectrum indicates that we are seeing the bare continuum disk emission from the quasar: thus disk Comptonization models, where the X-rays are produced via inverse Compton emission in a hot corona embedding a cooler accretion disk (e.g. Haardt & Maraschi 1993, Pounds et al. 1995), provide a satisfactory physical explanation to the data.

In a first step we fitted the combined PN data of each orbit, regardless of flux variations during the observation with the sum of two *compTT* components with absorption fixed at the galactic value. This Comptonization model describes the up-scattering of soft photons by hot, thermal electrons in a corona above the accretion disc. The temperatures of the soft photons were assumed to be the same for both components. In Tab. 2.2 we present the results of the fits for the different orbits and observation modes. The temperatures of the soft photons, given in column 1 are always around 80 eV, with relatively small errors. The temperatures of the Comptonizing electrons of the first component turned out to be $\mathrm{k\,T_1} = 4.5{-}5$ keV, the optical depths around $\tau_1 \sim 2$, both with rather large errors. The second component is characterized by rather high temperatures, $\mathrm{k\,T_2} \gtrsim 50$ keV, but optical depths $\tau_2 \lesssim 1.0$, and both parameters have very large errors.

The physical parameters in the Comptonization models are only poorly constrained because the spectral shape in the X-ray range is mainly determined by the combination of the temperature $\mathrm{kT/mc^2}$ and the optical depth τ of the scattering electrons; the cutoff energy is essentially related to $\mathrm{kT/mc^2}$. For Comptonizing electrons as hot as found from the fits, the determining spectral characteristics (high energy cut-off) is at energies far above the energy range of the XMM instruments and only the spectral index α of the non-relativistic, low-energy part of the spectrum can be obtained (Titarchuk & Lyubarskij 1995). Variations of the spectral shape with intensity, time lags between the fluxes in different energy bands, or energy resolved power density spectra as additional diagnostic tools (e.g. Kazanas et al. 1997) might provide insight into the way the corona is heated and cooled.

2.4.1 High energy power law fits

While the cooler Comptonization model nicely matches the PN energy band only the power law like, low energy part of the hot Comptonizing component falls into the energy band ≤ 10 keV. We therefore fitted the data with a combination of a *compTT* plus a power law model. The temperature of the Comptonizing photons was fixed at $\mathrm{k\,T} = 4.5$ keV and the absorption to the galactic value.

Table 2.3 summarizes the results of these fits. The parameters of the Comptonization model are rather well determined, the errors of the normalization are typically $\sim 6\%$. The slopes of the high energy power laws are reasonably accurate, the normalizations of the power laws show, however, rather large errors which can amount to $\sim 30\%$ during the high states, when the power law contribution to the total spectrum is small.

In Fig. 2.7 we show the dependencies of fitted parameters of the comptonization component on the corresponding count rates of the observation interval. The temperature T_0 of the soft input photons (bottom panel) remains around 80 eV, with no clear correlation with the intensity state of the source (a linear fit yielded a slope of $\beta = (0.316 \pm 0.305) \times 10^{-3}$). The optical depth shows a linear correlation with count rate with a slope of $\beta = (0.282 \pm 0.039) \times 10^{-1}$. The parameters of the power law components of the same fits are shown in Fig. 2.8. The spectral index remains nearly constant (slope of linear fit $\beta = (0.560 \pm 0.338) \times 10^{-2}$) at a value of 2.0. Note, that in most plots the intrinsic variance of the data is quite high.

The normalization of the power law changes only marginally and quite generally, the errors of the fitted parameters are larger when the source is bright and thus the relative contribution of the power law component smaller. Changes of the flux are thus mainly caused by an increase of the optical depth of the scattering electrons combined with an increase of the normalization of the Comptonization component.

We repeated the fits, leaving the temperature of the scattering electrons free but fixed the optical depth to $\tau = 1.8$. The results are very similar to those of Fig. 2.7. The flux variations are in that case correlated linearly only with changes of the temperature of the scattering electrons over the range 3.9 keV $\lesssim$ kT $\lesssim$ 7.4 keV.

2.5 Discusssion

2.5.1 Spectral properties

The spectrum of PKS 0558–504, like that of other NLS1 galaxies, can be fitted well by a combination of two compTT Comptonization models: one with low ($\sim$ 4.5 keV) temperature and moderate optical depths ($\tau \sim 2.0$) and a second, high temperature component with kT $\gtrsim$ 50 keV and low scattering depths ($\tau \lesssim 0.7$). A determination of exact parameters of the scatterer is not possible: from the high kT component only the low-energy power law can be seen in the XMM energy band and the measured slope is merely an indicator for a wide range of possible (kT,τ) combinations (Titarchuk & Lyubarskij 1995). The low temperature component shows in principle measurable characteristic changes of the spectral slope inside the PN energy band; however, the superposition of the two components

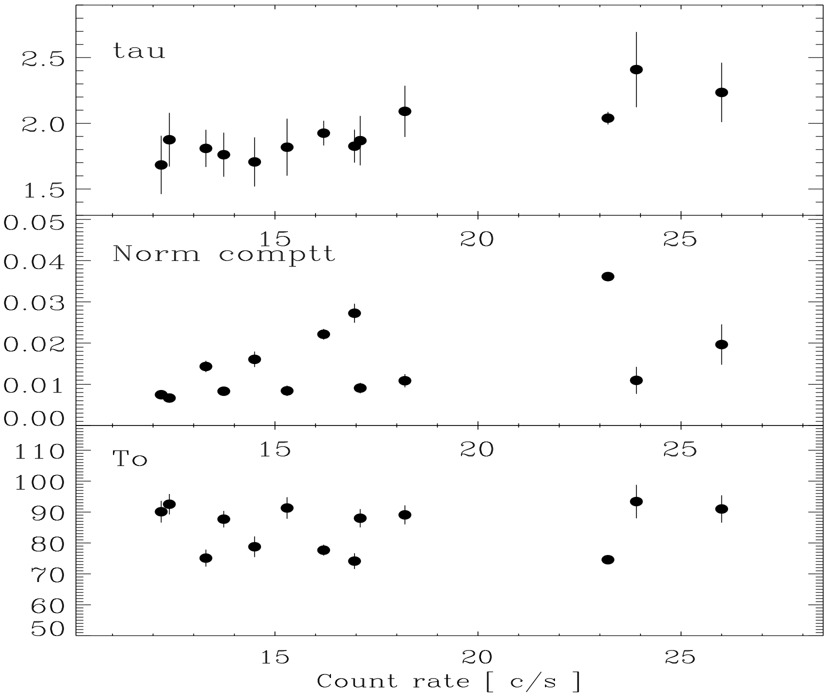

Figure 2.7: Parameters of the compTT component of a compTT + power law fit as a function count rate.

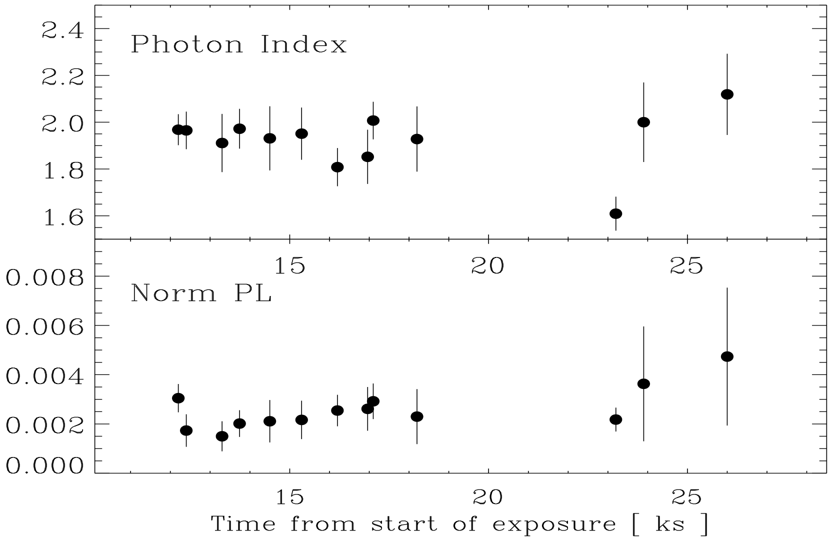

Figure 2.8: Parameters of the power law component of a compTT + power law fit as a function count rate.

and the position of the spectral break at rather high energies ($\gtrsim 5$ keV) with low photon statistics leaves considerable uncertainties in the parameter determination as well. Thus, this low-temperature component could be quite well replaced with a considerably hotter component with much smaller optical depth; the physical implications of this (less favored) combination will be discussed below.

Nevertheless, the above envisaged two components, low kT and high τ plus high kT and low τ represent an appealing picture for the X-ray emission of NLS1 galaxies. The high temperature component is very similar to that describing the emission of broad line Seyfert 1 (BLS1) galaxies. For those BeppoSax measurements (Petrucci et al. 2001) gave temperatures in excess of 150 keV and optical depths around $\tau \sim 0.2$. As the PDS detector covers the high energy band where spectral curvatures occur, the errors on temperature and optical depth are very small; the largest uncertainties seem to be related to the exact spectral shapes predicted by the different Comptonization models.

Unfortunately, the low signal-to-noise high energy BeppoSax data for PKS 0558–504 do not further constrain the parameters of the hot Comptonization component. A fit to the combined MECS and PDS data with

Table 2.3: Results from spectral fitting of a *compTT* plus a hard power law model, assuming fixed galactic $\mathrm{N_H} = 4.4 \times 10^{20}\mathrm{cm}^{-2}$, z=0.137

Orbit mode	kT_o (eV)	kT (keV)	τ	norm_{compTT}	Γ	norm_{po}	χ^2_{red}	dof
30FF	75.1 ±2.8	4.5	1.81 ±0.14	2.29E-02	1.91 ±0.12	2.40E-03	1.104	466
32FF	89.1 ±3.1	4.5	2.09 ±0.19	1.81E-02	1.93 ±0.14	3.84E-03	1.033	718
33FF (1)	88.0 ±3.0	4.5	1.87 ±0.19	1.51E-02	2.01 ±0.08	4.86E-03	1.045	825
33FF (2)	92.5 ±3.3	4.5	1.88 ±0.20	1.07E-02	1.97 ±0.08	2.78E-03	1.082	641
33FF (3)	87.7 ±2.7	4.5	1.76 ±0.17	1.34E-02	1.97 ±0.09	3.24E-03	1.076	665
42FF	91.0 ±4.4	4.5	2.24 ±0.23	2.67E-02	2.12 ±0.17	6.43E-03	1.025	759
45SW	76.3 ±1.2	4.5	1.94 ±0.06	2.67E-02	1.80 ±0.07	2.37E-03	1.040	856
84FF	78.8 ±3.4	4.5	1.71 ±0.19	1.91E-02	1.93 ±0.14	2.51E-03	0.953	417
84SW	74.1 ±2.6	4.5	1.83 ±0.13	2.66E-02	1.85 ±0.12	2.56E-03	1.025	487
153FF	91.3 ±3.5	4.5	1.82 ±0.22	1.34E-02	1.95 ±0.11	3.46E-03	1.060	578
153SW	77.7 ±1.8	4.5	1.93 ±0.09	2.14E-02	1.81 ±0.08	2.46E-03	0.971	658
283FF	90.1 ±3.5	4.5	1.68 ±0.22	0.96E-02	1.97 ±0.07	3.90E-03	1.116	697
341FF	93.4 ±5.4	4.5	2.41 ±0.29	1.99E-02	2.00 ±0.17	6.60E-03	1.109	794

a compTT model resulted in a kT = 47 keV, $\tau = 0.56$ and a $\chi^2_{\mathrm{red}} = 0.97$. However, the 90% confidence intervals for these values are 20.8 keV $\lesssim$ kT $\lesssim$ 162 keV and 0.01 $\lesssim \tau \lesssim$ 2.85.

The PKS 0558–504 fits at higher energies of either a power law or the hot Comptonizing component are in agreement with the results for the BLS1 fits, as can be seen from the conversion of the power law slopes to (kT,τ) (Titarchuk & Lyubarskij 1995, eqn 17, 22). Thus, this component seems to be present in both object classes, in NLS1 and BLS1 galaxies.

In addition to this hard component NLS1 galaxies show a second, softer Comptonization component. This soft component contributes about twice the luminosity of the hard component over the 0.1–100 keV energy range and clearly dominates the emission in the XMM band. As the Compton luminosity of a source is proportional L $\sim y \times U \times R^2$ (Haardt, private comm.), where U is the radiation energy density of the soft photons, R the size of the source and $y \sim kT \max(\tau, \tau^2)$ is the Compton y parameter, the emission areas for the two components with the above given parameters must be of similar sizes.

In contrast to BLS1 galaxies no iron lines from a reflection component could be detected. It appears that the 'cold reflector' in BLS1 galaxies, responsible for the iron line emission, is replaced by a 'warm' (kT $\sim$ 4.5 keV), scattering component. Further, the higher optical depths imply that any reflection features (like the iron line) tend to be more suppressed by Compton scattering in the corona itself (Matt et al. 1997).

2.5.2 Temporal variability: short time scales

The source shows variability on various time scales. During the individual observations we find flux changes of typically $\lesssim$ 20% (the maximum is nearly 50% in orbit 33) on time scales of a few hours. A closer inspection shows that these flux variations are caused by changes of the soft compTT component only; the hard component remains practically constant.

This is nicely illustrated in Fig. 2.9 which shows the comparison of the two spectra for the low and high state of orbit 32. We fitted the first, about 5 ksec, of the data when the source was at a low flux level with two compTT models. We then froze the fit parameters and plot the data from the peak of the light curve and the deviations of the these data from the model (in $\delta\chi^2$) in the bottom panel of Fig. 2.9. As can be seen, the intensity changes occur only in the soft part of the spectrum.

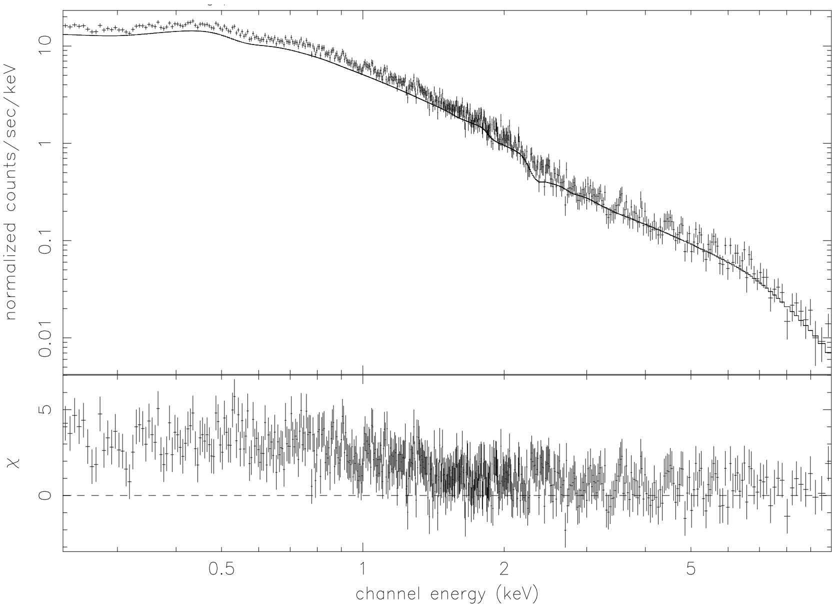

Figure 2.9: The high state data of orbit 32 overlaid on a two component compTT model with parameters which were obtained from a fit to the low state data from the first 5 ksec of the observation. The lower panel shows the $\delta\chi^2$ per channel between data and this model.

More details of the spectral behavior can be seen in Fig. 2.10 which shows the changes in the spectrum during orbit 42. The spectra correspond first to the low count rate state at the beginning of the orbit, then to the rising phase, and finally to the high count rate state at the end of this observation. The spectra were fitted with fixed galactic absorption and a fixed temperature of 4.5 keV for the Comptonising electrons to avoid the degeneracy problem between optical depth and electron temperature. The model parameters of the power law component remain unchanged within the errors while in the Comptonization component the optical depth increases slightly with count rate from 2.1 to 2.5. In these fits the increase in the optical depth is responsible for the change of the spectral shape: it dominates the spectrum up to higher energies as the count rate increases.

The plot further illustrates the difficulties of a hardness ratio analysis: at low count rates the soft and the hard band are each representing the contribution of the individual Compton components; at very high intensities most of the XMM spectral range is dominated by the soft component.

Thus the flux changes occuring on time scales of $\gtrsim$ 2 hours in a relatively smooth manner are caused by variations of the strength of the soft compTT component. Whether these variations are caused by changes of the temperature of the Comptonizing gas (at constant scattering depths τ and normalizations) or by changes of τ and the normalization at a constant gas temperature cannot be distinguished from the spectral fits. The first scenario would require a heating of the same gas volume, possibly by electromagnetic processes (i.e. Alfvén waves); the latter requires changes in the size of the emitting area and/or the volume of the gas responsible for the emission. This could be most easily achieved by an increase of the number of active emission regions on the disc (Haardt et al. 1994), which are formed at similar temperatures but with initially higher densities and then evolve gas dynamically. A popular class of models which follows these patterns are magnetically heated coronae where the energy is primarily stored in magnetic fields which rise buoyantly from the disc, reconnect and release their energy in flares (Merloni and Fabian 2001). These heat the corona and can trigger an avalanche (Poutanen & Fabian 1999) which create in turn a bigger active region.

The energy released in a typical burst $\Delta L \Delta t$ is of the order of 10^{45} erg. Using the characteristic size of the system (see sects. 4.3, 4.4) of a few $\times 10^{13}$ cm it turns out that this energy can be stored easily in a magnetic field of the order of $\lesssim 10^3$ Gauss or, taking the physical parameters from the Comptonization fits, as thermal energy of the gas. However, recently Merloni & Fabian (2001) strongly argued in favor of magnetic fields for storing the energy in the corona. The time scales for Compton cooling are rather short, of the order of 10^2 secs only (Wang et al., 2001), therefore the evolution of the bursts must be governed by the rate at which energy can

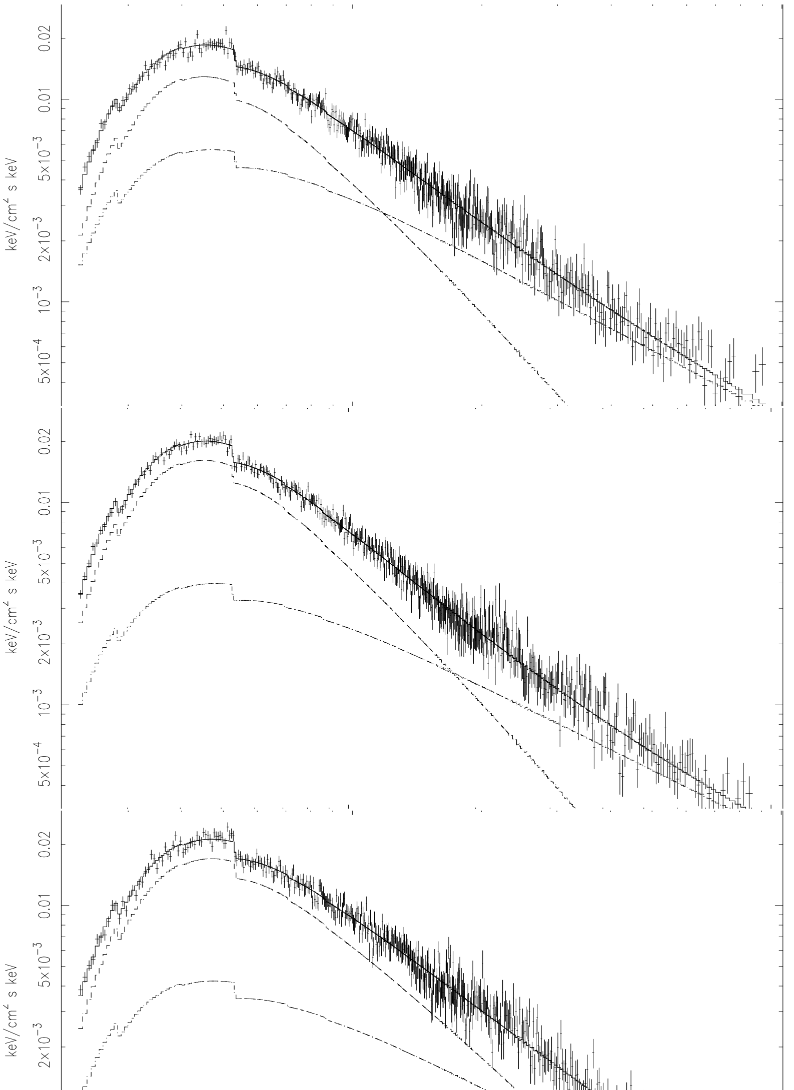

Figure 2.10: Unfolded spectra from orbit 42 in the preflare(top), rise(middle) and flare(bottom) stages. The average count rates for the plots, from top to bottom, are 24.2, 25.0, 28.0 counts/s.

be supplied to the emission region.

2.5.3 Temporal variability: longer time scales

We find evidence for a time scale of $\sim$ 24 ksec in the data from the recurrent occurrence of stronger intensity peaks. Unfortunately, the statistical significance for the existence of such signal cannot be assessed reliably due to the extreme sparcity of the data. Although not strictly periodic - there are some orbits where no peak occurs at the expected time - this time scale seems to represent a quite stable clock in the system. It might either be a rather well defined time scale of a dominant instability occurring in the disc or it might be related to the orbital time scale of the emitting matter.

By adopting the empirical broad-line region size versus optical luminosity relation of Kaspi et al. (2000) and using the Hβ line width of 1250 $\mathrm{km\,s^{-1}}$ (Corbin 1997) a central black hole mass of 4.5×10^7 $\mathrm{M_\odot}$ was derived for PKS 0558–504 by Wang et al. (2001). Assuming Keplerian motion the above time scale of $\sim$ 24 ks would correspond to the orbital period at $\sim$ 3.2 Schwarzschild radii, i.e. just outside the last stable orbit. Considering the uncertainties in the above mass determination this distance strongly supports the interpretation that the 24 ksec time scale is related to the orbital motion of the emission region.

2.5.4 Temporal variability: the longest time scales

On even longer time scales, of the order of several satellite orbits, the source changes by more than a factor of two, but we never see these transitions to occur during an individual orbit. For example, during orbits 42 and 45 the source is obviously in a high state which might thus last for more than a week. During the second part of orbit 33, i.e. about 2.5 weeks earlier, the flux is more than 2.5 times smaller. That these long term intensity variations are a common phenomenon of NLS1 galaxies is demonstrated in the long light curves of Ark 564 (Gliozzi et al. 2002) or MCG-6-30-15 (Vaughan et al. 2002).

Substantial changes of the radiating area or the physical conditions of this area, respectively, are expected to happen on the dynamical time scale for Keplerian inflow, $\tau \sim 9\ 10^3\ (\mathrm{r/R_s})^{3/2}\ (\mathrm{M_{bh}}/10^7\ \mathrm{M_\odot})$ sec, where $\mathrm{R_s}$ is the Schwarzschild radius of the central black hole of mass $\mathrm{M_{bh}}$. With the above deduced parameters for PKS 0558–504 we find a time scale of $\sim 2.3{\times}10^5$s, which is consistent with the observational result that large changes of the source flux occur on time scales longer than an XMM orbit.

2.6 Conclusions

We have analyzed in some detail the observations of PKS 0558–504 performed over nine irregularly spaced XMM orbits spanning a time of more than two years.

The source showed strong variability of $\lesssim$ 20% in an individual observation with typical time scales of $\gtrsim$ 2 hours. The flux variations often exceed the efficiency limit for scattering limited spherical accretion. However, as the emission is dominated by Compton - up-scattered soft photons in a hot corona heated by magnetic reconnection, and the energy is stored in the magnetic fields which do not contribute to the scattering opacity, the effective efficiency could be as large as $\eta \lesssim B^2/(8\pi\rho c^2) \lesssim 1$, where ρ is the mass density of the corona region (Wang et al. 2001).

The flaring pattern seems to repeat with a time scale of $\sim$ 24 ksec, however not in a strictly periodic manner. Interpreting this time scale as the orbital time scale of Keplerian motion we find that the emission occurs at distances of $\gtrsim$ 3.2 Schwarzschild radii from the central black hole. On longer time scales, beyond the temporal spacing of the XMM orbits, intensity changes by more than a factor of two are observed, which can be related to the dynamical time scale of Keplerian inflow in the disc. We do not see any large flare from the source as reported from Ginga (Remillard et al. 1991) and ASCA (Wang et al. 2001) observations. Thus that phenomenon must be a rare event.

The spectrum of PKS 0558–504 (like that of several other NLS1 galaxies as well) can be well fitted by the sum of two Comptonization models, one with high temperature (kT $\gtrsim$ 50 keV) and low optical depths ($\tau \sim 0.7$), similar to that found for BLS1 galaxies, and an additional cooler component (kT $\sim$ 4.5 keV) and larger optical depths ($\tau \gtrsim 2$). Flux variations are predominantly caused by changes of this latter component, whose presence is obviously the distinguishing criterion for the X-ray properties of NLS1 galaxies.

As the spectral capabilities of current instruments are insufficient to resolve the degeneracy in the spectral shapes of multiple Comptonization model fits, the second (cooler) component could equally well be fitted by another hot component with extremely small optical depths ($\tau \lesssim 0.06$). This would, however, not change the general scenario of a magnetically very active corona on the accretion discs of NLS1 galaxies but require different physical parameters for the generation of the coronal active regions. Unfortunately, current corona models do not seem to have sufficient predictive power to allow to distinguish between these theoretical possibilities. The low mass of the accreting black hole, the correspondingly high accretion rate is expected to be responsible for higher magnetic field strengths in NLS1 galaxies (Mineshige et al. 2000) providing a mean for storing energy in the corona and leading to strong variability of the emission from the systems (Merloni & Fabian 2001, Merloni 2003). If the turbulent magnetic pressure greatly exceeds that of the gas turbulent Comptonization might play an important role in producing the soft X-rays (Socrates et al. 2003). This largely unexplored process would provide a direct link between details of the disc physics and the observed spectrum.

An unanswered question is related to the radio-loudness of PKS 0558–504, and how that effects the emission characteristics. The spectral decomposition into two Comptonization components and the short-term intensity variations are found in other, radio-quiet NLS1 galaxies as well, therefore we regard this as being a typical NLS1 characteristic and not related to a possible radio jet, although outflows are expected from powerful magnetically dominated coronae (Merloni & Fabian 2002). However, the additional emission from a jet might be responsible for the large flare events, detected by Ginga (Remillard et al. 1991) and ASCA (Wang et al. 2001). It should be noted that during the flare the spectrum was significantly harder than in the 'quiescence state' (Wang et al. 2001), thus indicating an additional, different emission mechanism.

Unfortunately, the X-ray spectra of NLS1 galaxies are nearly featureless and thus they bear only little discriminating power to allow parameter studies for the various corona models. The best way to get access to the physical processes responsible for the X-ray emission might be, like in BL Lac objects, to pursue detailed temporal analyses of the emission.

Acknowledgements This work is based on observations with XMM-Newton, an ESA science mission with instruments and contributions directly funded by ESA Member States and the USA (NASA). We thank Graziella Branduardi-Raymont for her help for producing RGS light curves and the referee, P. Uttley, for constructive comments which improved the quality of the paper. PA & EF acknowledge support by the International Max-Planck Research School on Astrophysics (IMPRS).

Chapter 3

X-ray to UV Variability Correlation in MCG-6-30-15

P. Arévalo, I.Papadakis, B. Kuhlbrodt, & W. Brinkmann

Astron.Astrophys. 430 (2005) 435-442

3.1 Abstract

We used a ~ 300 ks long *XMM-Newton* observation of the Seyfert 1 galaxy MCG-6-30-15 to study the correlation between the 0.2–10 keV X-ray and the 3000–4000 Å U bands. We found a significant correlation peak at a time lag of $\tau_{\max} \sim 160$ ks where the UV flux variations preceded the variations in the X-ray band. We interpret this result as evidence in favour of Comptonisation models where the observed X-rays are produced through Compton up-scattering of thermal UV seed photons from an accretion disc, as this process naturally predicts the UV variations to precede similar flux variations in the X-rays. The length of the time lag favours models where the observed UV and the seed-photon-emitting regions are connected by perturbations of the accretion flow traveling inwards through the disc, affecting first the main-U-band-emitting radii and then the innermost region where the bulk of the seed photons is expected to be produced. Finally, the absence of significant features in the correlation function with X-ray flux variations preceding those in the UV indicates that the observed U-band photons are not mainly produced through reprocessing of hard X-rays in this source.

3.2 Introduction

The spectral energy distributions of Active Galactic Nuclei (AGNs) are extremely broad, often ranging from radio wavelengths up to gamma rays. Though this is well established, the origin of the emission is still a matter of debate. In general most of the AGN's luminosity is in the so called Big Blue Bump in the optical-UV regime, and a considerable fraction of the energy is emitted in the X-ray band. The study of the variability of the sources in these energy bands and their correlations can provide important information on the emission mechanisms.

The most widely accepted model for the energy release in AGN is accretion of matter onto a supermassive black hole, and the accretion flow is thought to form an optically thick disc. In the standard picture this accretion disc radiates thermally mainly in the optical/UV band, for AGN black hole masses of $\sim 10^6 - 10^8$ $M_\odot$. The production of X-rays is commonly attributed to Compton up-scattering of UV-photons (e.g. Sunyaev & Titarchuck 1980) by hot electrons in a corona (Haardt & Maraschi 1991). Under this hypothesis the UV and X-ray light curves are expected to be correlated with the X-rays lagging the UV. However, it is also possible that the X-rays produced this way would illuminate the disc or other surrounding optically thick material and produce UV radiation through reprocessing (e.g. Guilbert & Rees 1988). If the bulk of the observed UV continuum arises from this thermal re-emission the resulting light curves would again be correlated but this time the UV should lag the X-rays. Some models where the UV and X-ray emission come from a single continuum process predict no time lags between the bands. In principle simultaneous observations of these two energy bands with good time resolution and sampling should provide information about the physical and geometrical conditions of the emission region and help to discriminate between the models.

Several multi-wavelength monitoring campaigns of AGN conducted in the previous decade aimed to search for correlations between X-rays and optical/UV emission. A definite correlation could be found in only a few cases and the sign or existence of a time lag differed from case to case (see Maoz et al. (2002) for the puzzling results of their long-duration campaign of NGC3516 together with a summary of previous studies). The existence of positive as well as negative time lags suggests that different processes could be dominating the emission at different times and, in general, does not imply any simple relation between the energy bands. Some cases where no lags were found might be explained in terms of inappropriate sampling of the light curves, if the time lags are for example much shorter that the typical spacing between data points.

In this paper we study the temporal variations of the Seyfert1 galaxy MCG-6-30-15 (m_B~13.8, z=0.00775). This galaxy is famous for its broad and skewed Fe K_α line (Tanaka et al. 1995), which is consistent with fluorescent emission from a disc close to the central supermassive black hole. This spectral feature is strong evidence for the accreting black hole model and limits the primary hard X-ray emitting region to a few Schwarzschild radii R_S (Fabian & Vaughan 2003). MCG-6-30-15 has been extensively observed in X-rays where it shows large and rapid flux variability (see eg. Iwasawa et al. 1996; Fabian et al. 2003). Timing analyses indicate a featureless, red-noise-like power density spectrum with a possible break at 10^{-4} Hz as its only characteristic time scale (Vaughan et al. 2003).

The aim of the work presented here is to determine the relationship between the UV and X-ray light curves of MCG-6-30-15. The results of cross-correlation analyses of the variability of the light curves are compared with the predictions of different emission models to estimate their applicability to this object. We make use of simultaneous X-ray and UV data obtained with the instruments on board *XMM-Newton*. The observation spans approximately 430 ks (i.e. ~ 5 days) and the time resolution, limited by the sampling time of the UV light curves, is ~ 1.2 ks. Therefore we can use these data to search for correlations between the X-ray and UV light curves on time scales of a few ks with lags up to a few days.

The paper is organized as follows: In Sec. 3.3 we describe the data reduction and the construction of the light curves. Sec. 3.4 contains the cross correlation analysis, implications of the results are discussed in Sec. 3.5 and we summarize our conclusions in Sect. 3.6.

3.3 Data reduction and light curves

MCG-6-30-15 was observed with XXM-Newton between July 31st and August 5th 2001, during revolutions 301, 302 and 303. The observations spanned a total time of $\sim$ 430 ks with 80 ks, 122 ks and 123 ks stretches of scientifically useful, uninterrupted exposures. For the analysis we used data from the EPIC-PN detector (Strüder et al. 2001) to construct the X-ray light curve and from the Optical Monitor, OM (Mason et al. 2003) for the UV.

The X-ray data used here have already been analyzed extensively by several authors. Vaughan et al. (2003) studied in detail the time variability of the X-ray continuum in the PN energy band. The broad Fe K_α line in the spectrum has been studied and modeled by Fabian et al. (2002), Fabian &

Vaughan (2003), Miniutti et al. (2003) and Ballantyne et al. (2003) using this same data set. Vaughan & Fabian (2004) tested different spectral models for the PN 3–10 keV band, and the soft X-ray spectrum was studied by Turner et al. (2003, 2004) using the reflection grating spectrometer (RGS) data of the same observation.

3.3.1 X-ray light curves

All EPIC-PN exposures were taken in the small-window (SW) mode using the medium filter. We processed the data using XMMSAS version 5.4.1. The light curve was constructed following the procedure described in Fabian et al. 2002, differing only in extraction radius (30" in the previous analysis, 50" in the present work). This bigger radius was chosen to include at least 90% of the energy of a point source (Ghizzardi & Molendi 2001) and results in a slightly higher count rate (6% difference) than that presented in the work mentioned above.

The background-subtracted light curves were binned in different bin sizes and the corresponding errors were calculated by propagating the Poissonian noise. Bins with data gaps were corrected for their effective exposure times. Since all exposures were taken in the same observation mode we did not correct for mode-dependent exposure time losses such as dead time or out-of-time events.

In general the background activity was low, on average less than 1% of the source count rate. Only in the last few ks of each exposure did the background increase significantly. These segments of the light curves were excluded from the analyses. The final light curve is shown in Fig. 3.1.

The X-ray light curve displays large amplitude variations in all observable time scales with an overall minimum-to-maximum ratio of ~ 5. The power spectrum of this light curve has approximately a broken power-law shape and the frequency of the break at $\sim 10^{-4}$ Hz indicates the presence of a characteristic time scale at $\sim 10^4$ s in the system. The average luminosity of the source in the 0.2–10.0 keV band is $\sim 10^{43}$ erg/s and the minimum-to-maximum luminosity difference has a value of $\Delta L \sim 1.5 \times 10^{43}$ erg/s (Vaughan et al. 2003).

3.3.2 UV light curves

The OM is a 30 cm optical/UV telescope co-aligned with the X-ray telescopes on board *XMM-Newton.* It is sensitive in the 1600-6000 Å wavelength range and its typical point spread function has a full width at half

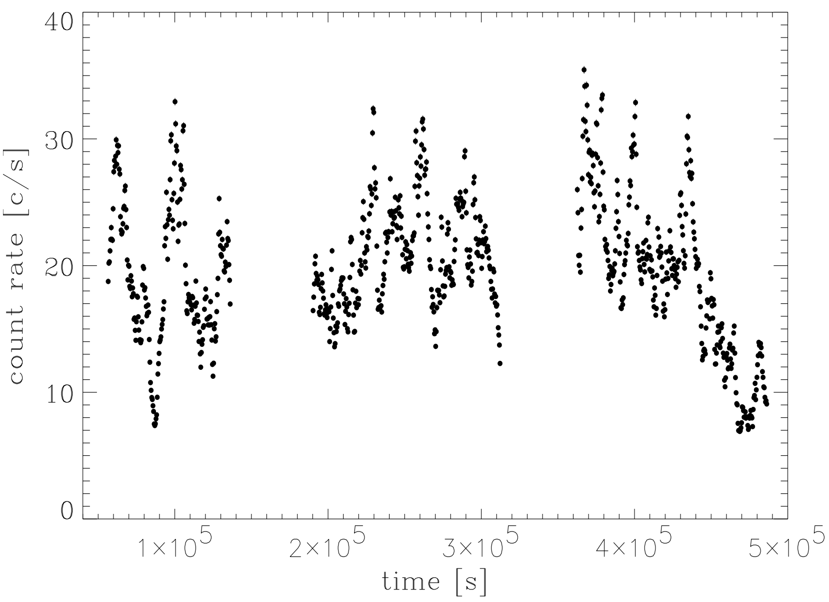

Figure 3.1: X-ray light curve from the PN data in 400 s bins. Time is in seconds starting from 0:00:00 hrs of July 31^{st}, 2001. The errors in the count rate are typically smaller than the symbols.

maximum of 2.2" in the *U* band. For this observation the OM was operated in imaging mode using the *U* filter (3000-4000 Å). We processed the data using the task OMICHAIN of XMMSAS version 5.4.1. The data consist of a sequence of 274 snapshot exposures 800 s long typically separated by time gaps of 320 s. Fig. 3.2 shows one of the OM exposures on logarithmic scale. The *U*-band luminosity of the AGN is smaller than that of the total host galaxy so the Poissonian error in the total (galaxy+nucleus) counts introduces a significant scatter that may mask the intrinsic variability of the nucleus. It was therefore essential to separate the contribution of the nucleus from that of the rest of the galaxy to obtain an accurate measure of the AGN variability. To do this we used the algorithm developed by Kuhlbrodt et al. (2004) which decomposes the image of a galaxy into disc, bulge and/or nuclear point source components.

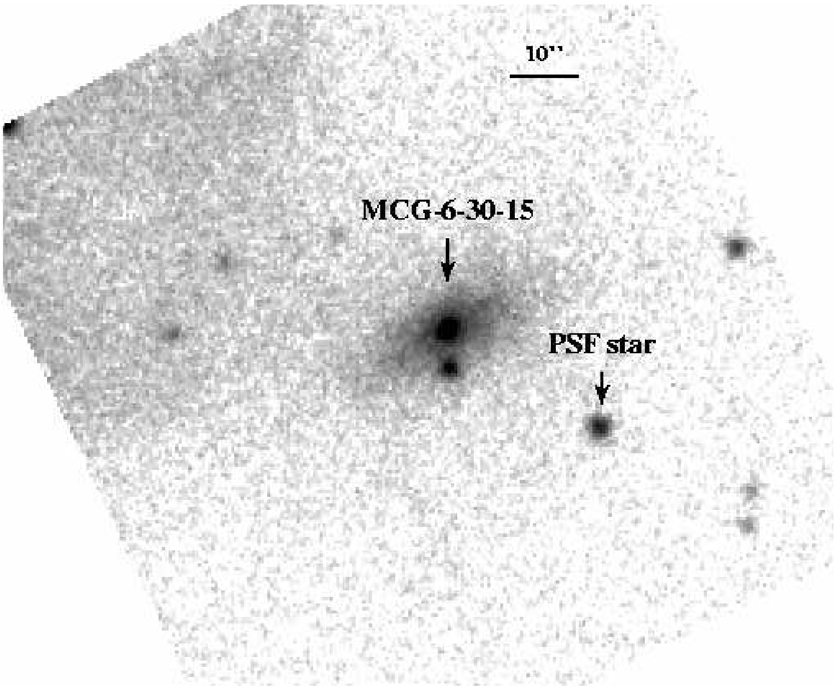

Figure 3.2: OM image of MCG-6-30-15. The host galaxy is clearly seen around the brightest point source, which corresponds to the AGN. The secondary object 6" to the south of the nucleus and the non-uniform background pattern were taken into account in the fitting procedure.

The principle behind the algorithm is that the light distribution of the nucleus is modeled with the image of a nearby star. Since both the star and the active nuclear region are not resolved in the UV, their images are representative of the point-spread function (PSF) of the optical system. Spatial or temporal variation of the PSF do not play a role in our case: as a nearby star with high signal-to-noise was always present in the images, variations in the PSF were taken into account by determining its actual shape in every exposure. This star, labeled PSF star in Fig. 3.2, is only used for the PSF modeling and not for photometric comparison. The model of the galaxy consists of the exponential disk profile by Freeman (1970) and a de Vaucouleurs (1948) profile for the bulge, expanded to two dimensions with elliptical isophotes (see Kuhlbrodt et al. 2004 for details) and convolved with the PSF. The nuclear and galaxy components are then fitted simultaneously.

Image decomposition

As a first approach MCG-6-30-15 was fitted using a three-component model accounting for a disc, a bulge and a nuclear point source. The bulge contribution to the galaxy flux is small, typically $\sim 10\%$ of the disc flux. This component was subsequently discarded from the fitting procedure to improve the accuracy in the determination of the nuclear flux.

As can be seen in Fig. 3.3 the two-component (disc+nuclear point source) model is a good approximation and fits the light profile accurately. This figure shows the model fit, where the dashed line represents the disc, the dashed-dotted line the nuclear component and the solid line represents the sum of the components fitted to the data points (filled diamonds). It is important to note that although MCG-6-30-15 has been classified as an E/S0 galaxy based on the galaxy morphology as seen in the optical band, in the U band it is very well fitted by a Freeman disc model only.

We used the two-component model to fit all 274 images individually, allowing only for variable nucleus and disc normalisations. The disc fluxes obtained showed a very small scatter in their values, entirely accountable for by Poissonian noise, and gave no indication of strong systematic changes in the photometric performance of the detector. However, as the nuclear flux is small compared to the disk flux, $F_{\rm nuc}/F_{\rm disc} \sim 0.17$, and the simultaneous determination of both fluxes is slightly degenerate, even small errors in the disc flux could result in significant artificial variations in the nuclear

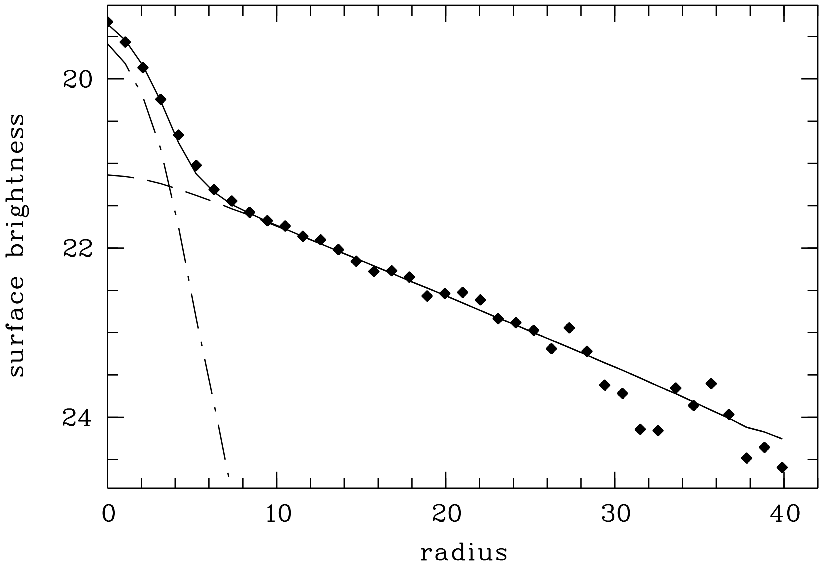

Figure 3.3: Light profile fit with a two-component model. The radius is in pixels (1 pixel=0.48”) and the surface brightness in arbitrary units. The solid line shows the total model fit to the data (filled diamonds). The dashed line shows the disc contribution, and the dashed-dotted line the nuclear component.

light curve. To make sure that the nuclear variability present in the light curve was not an artifact of this degeneracy we modified the routine in order to enforce a constant disc flux. This was done by taking the average disc flux to produce a galaxy template and compare this to the galaxy component in each image, excluding the central region. The background level was then fine-tuned to minimize their difference. By following this procedure we could subtract the background accurately and fix the disc flux to the template value. The final nuclear flux was determined by fitting once more the nuclear component to all the background-corrected images.

To estimate the error in the determination of the nuclear flux we made dedicated Monte Carlo simulations using synthetic images. We generated images with the template-galaxy disc parameters and appropriate PSFs for the nuclear component. We used 10 different disc-to-nucleus flux ratios around the measured values. Observational noise was then added before running the fitting routine on the synthetic data set. We ran the process for 170 synthetic images to estimate the performance of the decomposition routine in the specific conditions of the data. The errors in the determination of the nuclear flux were 3.5%, independent of the flux ratio in the range studied.

The light curve was constructed by plotting the nuclear flux as a function of the midpoint time of each exposure and is shown in Fig. 3.4. To reduce the scatter produced partly by observational noise we binned the data in 10 ks ($\sim$ 10 exposures per bin) and calculated the errors by averaging quadratically the errors of the individual points within the corresponding bin. In this way the intrinsic low amplitude variability of the light curve becomes evident; it can be seen as the filled circles overlaid on the same plot. The binned UV light curve varies smoothly on time scales of $\sim$ 100 ks with a maximum amplitude variation of 15% throughout the observation, small compared with the variations by a factor of 5 observed in the X-rays. The average U-band nuclear flux measured is $\sim 7.60 \times 10^{-13}$ erg/s/cm^2. Assuming a distance of 30 Mpc (Hayashida et al. 1998) and galactic extinction of $A_\lambda = 0.334$ (Schlegel et al. 1998), the average nuclear luminosity in the U band is $\sim 1 \times 10^{41}$ erg/s. For comparison we also constructed the light curve of the star used for PSF modeling using simple aperture photometry. The resulting 10-ks-binned light curve showed small fluctuations, a χ^2 test gave a value of $\chi^2_{red} = 1.34$ for 35 degees of freedom against the constant flux hypothesis. These fluctuations are somewhat larger than those expected purely from Poissonian noise and could reflect variations in the sensitivity of the detector. However, given their small amplitude these variations could only account for a fraction of the fluctuations seen in the nuclear light curve which gives a value of $\chi^2_{\rm red} = 6.89$ for the same test.

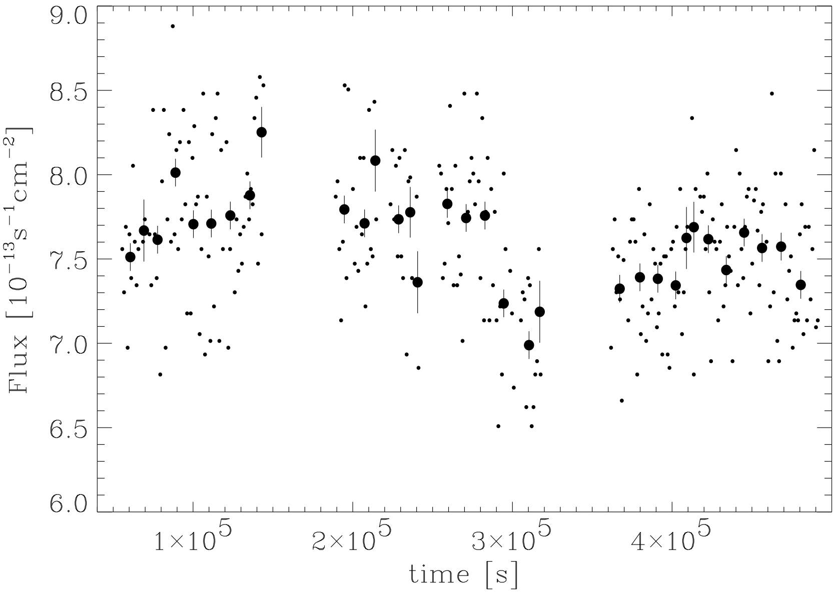

Figure 3.4: U-band light curve; dots show the unbinned data and filled circles the 10-ks-binned light curve. For clarity, only the error bars of the binned light curve are shown. The errors were calculated using Monte Carlo simulations as described in the text. The time is in seconds, counted from 0:00:00 hrs, July 31^{st}, 2001.

3.4 Cross-correlation analysis

The cross correlation between the UV and X-ray light curves was computed using the discrete correlation function (DCF) method of Edelson & Krolik (1988). The X-ray data were binned in 5 ks bins to smooth out the rapid variations, which are not observed in the UV. The UV light curve was binned averaging five consecutive points to reduce the scatter and the error of the individual points. The DCF between the full X-ray band (0.2–10 keV) and the UV light curve using a lag bin of size $\Delta\tau = 10$ ks is plotted in Fig. 3.5. The most significant feature is the positive correlation peak at $\tau_{\rm max} = 160$ ks with amplitude $DCF_{\rm max} = 0.82$ where the variations in the UV lead those in the X-rays. No significant peaks, either positive or negative, are evident in negative lags i.e. there is no indication of UV variations being driven by changes in the X-ray flux on the time scales probed.

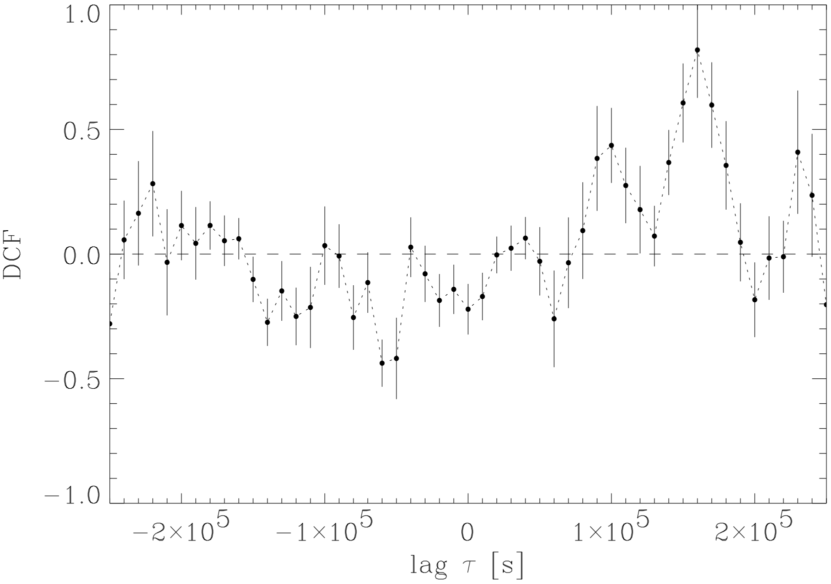

Figure 3.5: Discrete Correlation Function (DCF) calculated between the full X-ray band (0.2–10keV) and the UV light curve as a function of time lag in seconds. Positive lags imply UV leading X-rays. The DCF binning used is 10 ks. The error bars plotted represent the standard error of the DCF only and do not account for the effects of the correlations between nearby data points.

In order to estimate the error on $\tau_{\max}$ and $DCF_{\max}$ we used the Monte Carlo method described by Peterson et al. (1998). We find $\tau = 160^{+45}_{-65}$ ks, while $DCF_{\max} = 0.82^{+0.17}_{-0.25}$ where the errors represent the 95% confidence limits. These errors are associated mainly with the uncertainties caused by the observational sampling of the light curves and the flux uncertainty in the individual measurements. However, since both light curves are probably realisations of a red-noise process, it is possible to detect significant correlations even if they are intrinsically uncorrelated. In order to investigate this issue further, we performed a second numerical experiment.

As already mentioned in Sec. 3.3.1, the X-ray power spectrum has a broken power-law shape. Vaughan et al. (2003) found a slope of -1 up to a frequency of 10^{-4} Hz above which the slope steepens to a value of ~ -2 for one of their fitted models. Assuming this power spectral shape, we used the method of Timmer & König (1995) to construct 10,000 synthetic light curves with a mean and variance equal to those of the 0.2–10 keV light curve. The points in the synthetic light curves were sampled every 10 s in order to account for aliasing effects, while the length was 10 times larger than that of the observed X-ray light curve in order to account for red-noise leak. These synthetic light curves were then re-binned in 5 ks bins and sampled to match the length and sampling pattern of the original X-ray light curve. We estimated the DCF between the observed UV light curve and each of the synthetic light curves, registering the resulting $DCF_{\rm max}$. Only in 1.5% of all cases did we find a $DCF_{\rm max}$ value larger than 0.82, at any lag. We repeated this procedure using slightly flatter and steeper power spectrum slopes with nearly identical results. We conclude that the positive correlation that we detect in Fig. 3.5 is significant in the sense that most probably it is due to an intrinsic coupling between the observed UV and X-ray flux variations. In the same simulations we found peaks with $|DCF_{\rm max}| > 0.4$ in approximately 90% of the cases indicating that the peaks seen at $\tau \sim$ -60, 100 and 230 ks are not significant.

Figure 3.6 shows a plot of the X-ray and UV light curves normalized to their mean (filled and open circles, respectively). The X-ray light curve is back-shifted by 160 ks and the plot shows the period where the light curves overlap. The light curves are binned in order to eliminate the fast, large amplitude variations of the X-ray flux and to increase the signal-to-noise ratio in the case of the UV. This figure reveals clearly the reason for the large DCF peak value at lag 160 ks. If we take into account the delay, the modulation of the UV flux matches well that of the smoothed X-ray light curve over the interval sampled. The correlation suggests an intrinsic link between the observed variations in the two energy bands on time scales of $\sim$ 10-100 ks, which operates with a delay of $\sim$ 160 ks.

We also investigated briefly the correlation between the UV and the X-ray light curves in different energy bands. The resulting DCFs are very similar to that shown in Fig. 3.5, as is expected since the different X-ray energy bands show similar variations. In all cases, we observe a strong peak at lag $\sim$ 160 ks, although its amplitude shows minor differences. We find that the 2–4 keV and 8–10 keV light curves are the best correlated with the UV, both with a value of $DCF_{\rm max} = 0.84$. The 4–7-keV-band light curve, which is representative of the Fe K_α line emission, shows a marginally

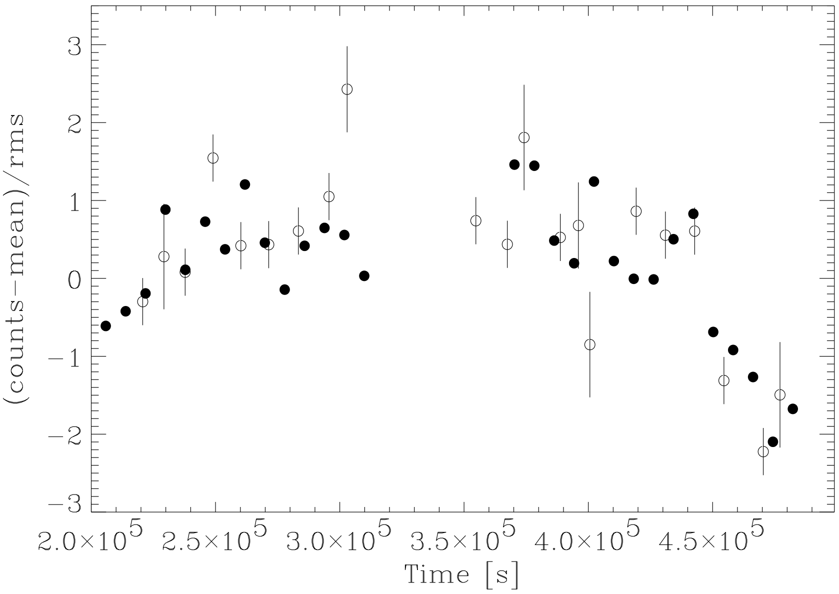

Figure 3.6: Overlap region of the normalized UV light curve (open circles) in 10 ks bins and back-shifted X-ray light curve (filled circles) in 8 ks bins. The X-ray light curve was shifted back in time by 160 ks. The X-ray error bars are smaller than the symbols.

weaker correlation ($DCF_{\rm max} = 0.83$), while the soft-excess-component (0.2–1.0 keV) light curve shows the weakest correlation with the UV light curve with a peak of $DCF_{\rm max} = 0.78$.

3.4.1 DCF between the UV flux and the variations in the X-ray energy spectrum

In order to investigate possible correlations between the UV flux and the variations in the X-ray energy spectrum we used the 2–4 and 8–10 keV light curve to construct the 2–4 keV/8–10 keV softness ratio curve. These energy bands were selected to show the spectral changes in the 2–10 keV continuum while minimizing the contribution of the Fe line and the soft excess. The softness ratio so defined is representative of the slope of the continuum, where higher values correspond to steeper spectra. We used softness ratio and UV light curves in 5 ks bins and lag bin size of $\Delta\tau = 10$ ks to calculate the DCF, and found a moderately good correlation ($DCF_{\rm max} = 0.67$) again at a time lag of ~ 160 ks. We should point out that this value of the $DCF_{\rm max}$ is found in approximately 10% of the Monte Carlo trials described above and so the correlation is formally not significant on its own.

The X-ray spectrum in these energy bands can be well fitted by a power-law model, with photon index $\Gamma \sim 2.0$. To investigate the behaviour of the spectral slope we fitted a power-law model to the 2–4 and 8–10 keV bands every 10 ks. Fig. 3.7 shows a plot of the UV light curve (open circles) and of the photon-index (Γ) curve normalized to their mean, where the photon-index curve has been back-shifted by 160 ks. Like in Fig. 3.6 we show only the period where the UV flux and the Γ curves overlap. The figure shows that the UV flux is well correlated with the X-ray spectral slope, the 2–10 keV continuum flattens (i.e. Γ decreases) as the UV flux decreases, with a time delay of 160 ks.

3.5 Discussion

The connection between the UV and X-ray emission from AGN is thought to be primarily due to two processes: Comptonisation of UV photons into X-rays and reprocessing of X-rays into the UV range. Here we discuss both mechanisms and confront their predictions with our results.

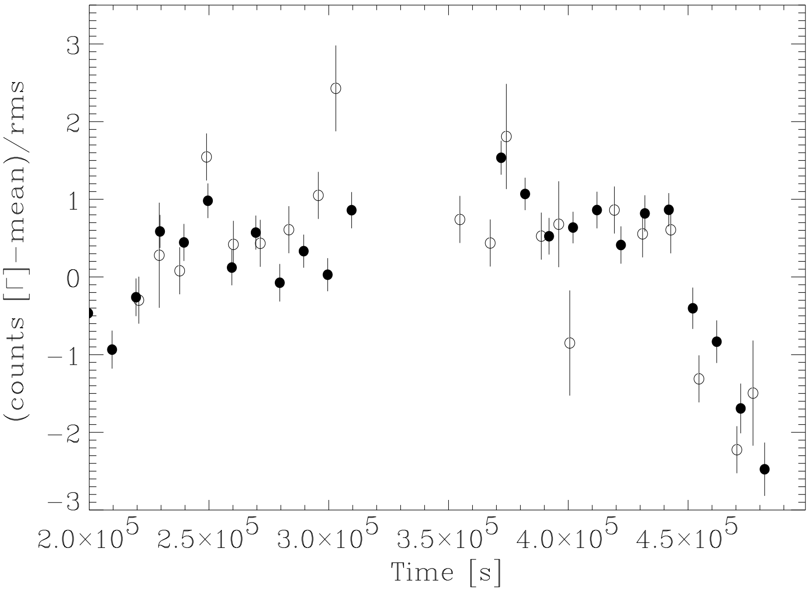

Figure 3.7: *U*-band light curve in 10 ks bins (open circles) overlaid on the photon-index curve of the hard X-ray spectrum fitted with a power-law model (filled circles). The photon-index (Γ) curve has been back-shifted by the 160 ks corresponding to the highest peak in the DCF between softness ratio and *U*-band light curves. Both curves were mean-subtracted and divided by their rms.

3.5.1 Comptonisation scenario

The positive peak found in the DCF with UV variations leading those in the X-rays suggest that variations in the thermal component (accretion disc) drive the changes in the emission of the scatterer (corona) on time scales ≥ 10 ks, and constitutes evidence for the Comptonisation scenario.

Origin of the time lag

To investigate the possible origin of the time lag we estimate the physical separation of the emitting regions. The X-ray emission region is thought to be compact and located very close to the black hole due to its rapid high-amplitude variability and by the spectral shape of the fluorescent Fe line. Fabian et al. (2003) limit the size of the hard X-ray source to a few $R_{\rm S}$. The U-band emission is probably produced thermally through viscous dissipation in the accretion disc. We use the standard thin disc model to estimate the radii of maximum U-flux emission. For this we assume a disc radial temperature profile given by $T_{\rm eff}(R) = [(3GM\dot{M}/8\pi\sigma R^3)(1-\sqrt{R_{\rm in}/R})]^{1/4}$ where M is the black hole mass, $\dot{M}$ is the accretion rate estimated from the bolometric luminosity, σ is the Stefan-Boltzmann constant, R is the radius in the disc and $R_{\rm in}$ is the radius of the inner edge of the disc (see eg. Kato et al. 1998). We consider the disc to be composed of rings of approximately uniform temperature radiating locally as black bodies. For a black hole mass between 10^6 and $10^7 M_\odot$ (Hayashida et al. 1998; Czerny et al. 2001; Vaughan et al. 2003) and bolometric luminosity of 7×10^{43}erg/s (Czerny et al. 2001) the rings producing the largest flux in the U band (3000–4000 Å) are at $R \sim 100 R_{\rm S}$ for a $10^6 M_\odot$ black hole and $R \sim 25 R_{\rm S}$ for a $10^7 M_\odot$ black hole. The radii obtained correspond to light travel times between the emitting regions of only a few ks, too short to explain the measured lag.

However, if the accretion disc indeed extends down to a few $R_{\rm S}$ as the shape of the Fe line suggests, most of the disc flux should be emitted in this small radius and mainly in higher energy photons than the observed 3000–4000 Å band. Therefore the bulk of the seed photons for Comptonisation may be emitted in a different region of the accretion disc than the observed U band photons. The length of the time lag that we observe favours models where variations in the accretion flow affect first the flux at outer radii and then in the innermost region. In this case, the observed delay would correspond to the time needed for the accretion flow fluctuations to travel inwards from the radius where most of the U band photons are produced ($\sim 25 - 100 R_{\rm S}$) to the innermost region of $\sim 5 R_{\rm S}$ where most of the seed photons for Comptonisation are emitted. As a reference time scale, the sound crossing time in a standard thin disc between these radii with black hole mass of $10^6 M_\odot$ is ~ 1000 ks, marginally consistent with the measured lag. If we consider that the variable part of the UV light curve might arise from radii smaller than that producing most of the U band luminosity we obtain shorter sound crossing times, closer to the 160 ks lag. Alternatively, MHD effects might transport perturbations through the accretion disc faster than sound waves and remain a plausible source for the measured lag.

Spectral changes

The Comptonisation scenario is also supported by the correlated variations that we observe between the UV flux and the slope of the X-ray continuum energy spectrum. We find that when the UV flux rises the continuum becomes steeper with a delay of ~ 160 ks. This effect is qualitatively consistent with the behaviour of a hot plasma receiving more seed photons, radiating more X-rays and cooling to a new equilibrium temperature, thus producing a steeper power-law spectrum. A similar UV flux/Γ correlation has also been observed in the case of NGC 7469 (Nandra et al. 2000).

We should point out, however, that the UV flux/Γ correlation in MCG-6-30-15 may be merely a by-product of the UV/X-ray flux variability correlation. Fig. 3.8 shows a plot of the best-fitting Γ values as a function of the total count rate in the 2–4 plus 8–10 keV bands. The photon index Γ is well correlated with the count rate, with higher flux corresponding to a steeper spectrum. However, intrinsic Γ variations in MCG-6-30-15 have been questioned in the past using this and other data sets. For example, Taylor et al. (2003) and Fabian & Vaughan (2003) explain the X-ray spectral variations of the source with the combination of two components: a constant slope, variable normalization power-law component and constant reflection component. In this case there are no genuine Γ variations, as the softening of the spectrum is due only to a change in relative normalization of the two fixed shape components. If this is the case then the UV/Γ correlation results merely from the UV/X-ray flux correlation through the good correspondence between X-ray flux and spectral slope. The situation is far from clear, though, as the presence of a constant reflection component may not be able to account for the spectral slope variations of the source as shown by Papadakis et al. (2002). Since we find that both the UV/X-ray-flux light curves and the UV flux/Γ time series are well correlated with the same time delay, the present results do not help to discriminate between the two possibilities.

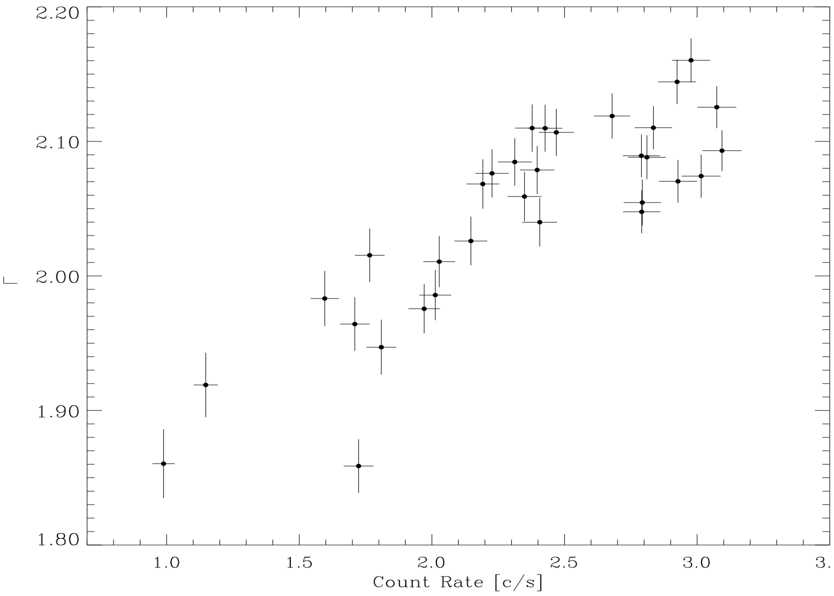

Figure 3.8: Photon index Γ of the power-law fitted to the 2–4 keV plus 8–10 keV spectrum as a function of the count rate in these bands.

3.5.2 Reprocessing scenario

There is observational evidence that the hard X-ray source in this object illuminates cooler nearby material, possibly the accretion disc. The broad and skewed Fe K_α line from fluorescent emission and the reflection hump detected in the X-ray band above 10 keV (Vaughan & Fabian 2004) give support to this statement. It is also expected that the X-rays illuminating such optically thick material would produce UV emission through thermal reprocessing and so produce correlated X-ray and UV light curves with X-ray variations leading the UVs. However, the DCF between these light curves showed no positive peaks with negative lags (ie. with X-rays leading the UV) and so give no indication of reprocessing.

To estimate the amount of reprocessed emission expected from the accretion disc we consider a simple model where the X-rays received by the disc are totally absorbed and re-emitted as black-body radiation. We start by calculating the expected U-band flux emitted by a standard thin disc around a $10^6 - 10^7 M_\odot$ black hole with bolometric disc luminosity $L_{\rm bol} = 10^{43.85}$ erg/s (Czerny et al. 2001) through viscous dissipation alone. We obtain the local black-body spectrum of the disc as a function of radius and then integrate the flux in the 3000–4000 Å band from $R = 3R_{\rm S}$ to $R = 3000R_{\rm S}$. We then recalculate the U-band flux now including the effect of reprocessing. For this simple model we assume that the reprocessed flux adds to the flux from viscous dissipation:

$$\begin{aligned} F(R) &= F_{\rm viscous}(R) + F_{\rm reprocessed}(R) \\ &= \frac{3GM\dot{M}}{8\pi R^3}\left(1-\sqrt{\frac{R_{\rm in}}{R}}\right) + \frac{L_{\rm X}\ h}{4\pi(R^2+h^2)^{3/2}} \end{aligned}$$

where R is the radius in the disc and h the height of the X-ray source over the disc. We take the illuminating X-ray flux $L_{\rm X} = 10^{43}$ erg/s and assume the emitting region to be compact, close to the disc axis, and at a height $h = 3 - 10R_{\rm S}$. The integrated U-band flux increases by only 3–12% when the illuminating X-ray component is included, where the lower flux results from the smaller height of the X-ray source. More importantly, a change by a factor of 4 in the X-ray flux induces only a change of 4–11% in the total U-band flux for the same range of h values. Considering the simplicity of the model these numbers can only be regarded as reference values. Moreover, they are only upper limits for this geometrical configuration, given that here we assume total reprocessing of the X-ray flux. We conclude that large variations of the X-ray flux can produce variations in the reprocessed component which are too small to be detected in this data, especially if the X-ray source is located at a small height h.

3.5.3 Comparison with previous results

Several studies of X-ray/UV/Optical correlations in AGN have been carried out in the past. From these only the short-term correlations found can be compared with the work presented here. We have no information on the correlation between the optical/UV and X-rays on long (months/years) time scales for MCG-6-30-15, and the correlated variability properties of other objects appear to depend on the time scales probed. Some objects for which similar studies have been presented are NGC 4051, NGC 7469 and NGC 5548.

Notably Mason et al. (2002) found the 2900 Å UV lagging the 2-10 keV X-ray continuum by 0.2 days from a 1.5 day long *XMM-Newton* observation of NCG 4051. The mass of this object is similar to that of MCG-6-30-15 and the variability amplitudes found for the X-ray and UV bands are comparable with those presented here. However they found a lag of opposite sign and interpret it as evidence for reprocessing, contrary to what we find in MCG-6-30-15. These results might be reconciled by noting that NGC 4051 was observed in a higher-frequency UV band. If the higher-energy UV emission comes from smaller radii of the accretion disc then this band can be affected more strongly by a compact X-ray source close to the centre. In this way the UV-reprocessed component, which is probably present in both objects, would be comparatively stronger in this observation of NGC 4051. A longer (2 month) monitoring of this object gave evidence for X-rays lagging the optical by ~ 2.4 days (Shemmer et al. 2003), similar in sign and magnitude to the lag we found in MCG-6-30-15 between X-ray and ~ 3500 Å bands.

As mentioned before, Nandra et al. (2000) found a good correlation between UV flux and X-ray spectral index peaking at 0 lag from a 30 day long observation of NGC 7469. This result is similar to what we observe in MCG-6-30-15 considering that a lag of ~ 100 ks would not be clearly discernible in their daily binned data. In NGC 5548 Chiang et al. (2000) found the extreme UV (0.1 keV) continuum leading the variations in the soft and hard X-rays by 10 and 40 ks respectively from a 20 day baseline campaign. Again this lag is qualitatively similar to what we find, with lower energies leading the variations of higher energy bands.

On long time scales however the behaviour of the objects studied can be quite different. NCG 5548 shows high-amplitude, highly correlated variability in X-ray and optical bands (Uttley et al. 2003), NGC 3516 also displays high-amplitude variability in both bands but this time the correlation is very weak (Maoz et al. 2002) while NGC 4051 shows very weak optical variability, although well correlated with the much more variable X-rays (Peterson et al. 2000).

It is possible to explain some of the different X-ray/UV long-term correlations observed in different objects by considering the differences in their black-hole masses as noted by Uttley et al. (2003). Since MCG-6-30-15 shows a similar behaviour to both NGC 5548 ($\sim 10^8 M_\odot$) and NGC 4051 ($\sim 10^6 M_\odot$) on short time scales, a longer-term optical campaign would be necessary to test the optical variability/black-hole-mass correlation in this object. Apart from this hypothesis it is hard to draw a consistent picture of the behaviour of all the cases studied given the small number of objects with similar observations and the large number of relevant intrinsic parameters. However, we can note that Uttley et al. (2003), from long-term optical variability amplitude, Shemmer et al. (2003), from considerations of the size of the X-ray-emitting region, and the work presented here, from the magnitude of the observed time lag between X-ray and UV variations, all agree that the connection between these energy bands is probably due to accretion-flow fluctuations traveling inwards across the emission regions.

3.6 Conclusions

We analyzed simultaneous UV and X-ray data of MCG-6-30-15 to study the relation between the time variability in these two energy bands on time scales of a few ks to a few 100 ks. The X-ray light curve displayed large amplitude variations reaching a maximum-to-minimum count rate ratio of ~ 5 which implies a change in luminosity of $\Delta L \sim 10^{43}$ erg/s. The UV light curve was calculated using a sophisticated decomposition technique to determine the nuclear flux accurately against the background of the bright host galaxy. This light curve showed much smaller amplitude variability than the X-rays, not larger than 15% during the whole observation, amounting to $\Delta L < 2 \times 10^{40}$ erg/s.

We found a significant correlation ($DCF_{\rm max} = 0.82$) between the light curves with a time lag $\tau = 160^{+45}_{-65}$ ks, where the UV variations lead the X-rays. We interpret the sign of this time lag as evidence for models where X-rays arise from Comptonisation of thermal UV photons, as in an accretion disc-corona scenario. The time lag is too long to represent the light travel time from the U-band emitting region of a standard disc to the centre, where the X-rays are thought to be produced. In turn this length favours models where the variations in the disc flux arise from perturbations in the accretion flow traveling inwards through the disc, affecting first the U-band emitting region and then the innermost radii from where the bulk of the seed photons for Comptonisation must come. Finally the cross-correlation analysis gave no significant correlation with negative time lags (ie. with X-ray leading UV) suggesting that the bulk of the observed UV does not arise from reprocessed X-rays.

Acknowledgements This work is based on observations with *XMM-Newton*, an ESA science mission with instruments and contributions directly funded by ESA Member States and the USA (NASA). We are very grateful to H. Spruit and P. Uttley for useful discussions and to M. Freyberg for OM data-processing assistance. We also thank the anonymous referee for useful comments. PA acknowledges support from the International Max Planck Research School on Astrophysics (IMPRS).

Chapter 4

Investigating a Fluctuating-accretion Model for the Spectral-timing Properties of Accreting Black Hole Systems

P. Arévalo & P. Uttley
submitted to MNRAS

4.1 Abstract

We use a simple computational model for a fluctuating accretion flow to explain the variability properties observed in X-ray light curves from accreting black hole systems. In the model, which is based on existing analytical models in the literature, variability is produced by accretion rate fluctuations that propagate through the accretion flow, modulating the emission on a broad range of time-scales. The X-ray light curves are assumed to be emitted by a radially-extended region, which acts as a low-pass filter reproducing the high frequency break observed in the PSD of Active Galactic Nuclei (AGN) and black hole X-ray binaries (BHXRBs). By assigning different radial emissivity profiles to the energy bands we obtain PSDs with higher break frequencies and/or flatter high frequency slopes for higher energy bands. Different emissivity profiles also introduce time lags between the corresponding energy bands without requiring any spectral evolution of the emitting region. Keeping the characteristic frequencies and propagation speeds tied to the local viscous time-scale of a thick disc produces time lags of similar magnitude and Fourier frequency dependence as those observed in the data. The predicted lags are quite robust to changes in the emissivity profile, disc parameters and the effects of damping on the fluctuations as they propagate inwards, which may help to explain the similarity of the lag spectra in the low/hard and high/soft states of Cyg X-1. Finally, the light curves resulting from this common emitting region are highly spectrally coherent. Coherence losses at the level of a few percent appear for certain model configurations, increasing with energy separation of the bands and with Fourier frequency. We compare model predictions to X-ray data from the Narrow Line Seyfert 1 galaxy NGC 4051 and the BHXRB Cyg X-1 and show that this general scheme can reproduce simultaneously the time lags, energy-dependence of the PSD and coherence.

4.2 Introduction

A common characteristic in Active Galactic Nuclei (AGN) and X-ray binary systems (XRBs) is their strongly variable X-ray emission. Most of the variability power is in the form of aperiodic fluctuations that span several orders of magnitude in temporal frequency (e.g. van der Klis 1995, M^{c}Hardy et al. 2004). Rapid, large amplitude X-ray variations, on time-scales down to milliseconds in XRBs and minutes in AGN, are commonly observed (e.g. Revnivtsev, Gilfanov & Churazov 2000, Gierliński & Zdziarski 2003, M^{c}Hardy et al. 2004), supporting the expectation from accretion theory that the bulk of the emission must originate close to the central black hole. However, in many sources (in both AGN and XRBs), large-amplitude X-ray variations, of tens of per cent fractional rms, are observed over several decades of time-scales (e.g. Reig, Papadakis & Kylafis 2002, M^{c}Hardy et al. 2004, Uttley & M^{c}Hardy 2005), including values orders of magnitude longer than the viscous time-scale of the inner disc, suggesting that these fluctuations must originate at large radii. This discrepancy motivated the appearance of propagating-fluctuation models, as proposed by Lyubarskii (1997), who noted that while the *emission* might be produced only in the innermost regions, the *variability* can originate throughout the accretion flow. In this model, accretion rate fluctuations arise over a wide range of radii and, correspondingly, a wide range of time-scales, and propagate inwards to modulate the central X-ray emission.

As noted by Uttley & M^{c}Hardy (2001) the model of Lyubarskii (1997) is consistent with the observed linear relation between rms-variability amplitude and mean count rate in XRB and AGN X-ray light curves, which implies a coupling between fluctuations on different time-scales, ruling out models where the variability arises from strictly independent flares or active regions (Uttley, M^{c}Hardy & Vaughan 2005). Fluctuating accretion models, on the other hand, are consistent with this relation: the fluctuations couple together as they propagate down to the centre, so low frequency fluctuations produced at large radii modulate higher frequency fluctuations produced further in. A linear rms-flux relation is also observed in neutron star XRB systems, where the emission mechanism is most likely different to the one operating in black-hole systems (Uttley 2004). This result provides additional evidence for fluctuating-accretion scenarios because it suggests that the variability originates in the accretion flow and not just locally via the mechanism producing the emission (Uttley 2004).

Besides explaining the broad range of variability time-scales and the rms-flux relation, the fluctuating accretion model can also explain the spectral-timing properties of the variability, as noted by Kotov, Churazov, Gilfanov (2001). For example, it has long been known (e.g. Miyamoto & Kitamoto 1989, Nowak, Wilms & Dove 1999) that X-ray variations in black hole X-ray binaries (BHXRBs) often show hard lags, i.e. a delay in hard X-ray variations with respect to soft X-rays, which is larger for variations on longer time-scales, and at higher energies. The magnitudes of the lags are typically of order one per cent of the variability time-scale. Similar time-scale-dependent, hard lags have recently been discovered in AGN, albeit on much longer time-scales, commensurate with their higher black hole masses (e.g. Papadakis, Nandra & Kazanas 2001, Vaughan, Fabian & Nandra, 2003, M^{c}Hardy et al. 2004). In their analytical extension to Lyubarskii's model, Kotov et al. (2001) explain these lags by invoking a radially extended X-ray emitting region with an energy-dependent profile. In this scenario, the response of the emission to a fluctuation in the accretion flow is a function of the inward propagation time-scale, and hence radius of origin, of the fluctuation, combined with the emissivity profile. Hence, if the emissivity profile is more centrally concentrated at higher energies, hard-band lags are produced such that the lags are larger for longer time-scale variations. Kotov et al. (2001) show that the same basic picture can also explain the energy dependence of the PSD of BHXRBs and AGN, where there is relatively more high-frequency power observed at higher energies than at lower energies (e.g. Nowak et al. 1999b,M^{c}ardy et al. 2004). This is because the emitting region acts as a low-pass filter and, as the emitting region of the soft band is more extended, the higher frequency variations are filtered more strongly in the soft band.

Due to its success in explaining many aspects of the X-ray variability data, the fluctuating accretion model of Lyubarskii (1997) and Kotov et al. (2001) warrants a deeper investigation, which is the aim of this paper. As shown by the brief analytical treatment of Kotov et al. (2001), in principle, the model produces time-scale-dependent lags of approximately the same amplitude as observed in the data, and energy-dependent PSDs. However it is not clear exactly how the lag spectrum (lag as a function of Fourier frequency) and energy dependence of the PSD varies as a function of emissivity profile, or the parameters of the accretion flow (assuming the standard disc model of Shakura & Sunyaev 1973 e.g. the viscosity parameter α or the scale-height of the flow), or due to the effects of radial damping of variations in the accretion flow. Furthermore, since Kotov et al. (2001) analytically determined spectral-timing properties by making the simplifying assumption that the perturbation introduced into the accretion flow at each radius is a delta-function in time and radius, it is important to determine the effects on spectral-timing properties of a more realistic model, where stochastic variations over a broader range of time-scales are introduced at each radius. Finally, the fluctuating accretion model should, in principle, produce light curves which are highly correlated in different bands (i.e. spectrally coherent, see Vaughan & Nowak 1997 and Appendix B of this paper), but this aspect of the model has not yet been studied. To study these various effects in more detail, in Section 4.3 we introduce a computational toy model for a fluctuating accretion flow, based on the work of Lyubarskii (1997) and Kotov et al. (2001), and explore the dependence of the PSD, time lags and coherence on the model parameters in Section 4.4. We show how the model predictions fit X-ray data from AGN and the BHXRB Cyg X-1 in Sections 4.5 and 4.6. Specifically, we will concentrate on explaining the spectral-timing properties of the BHXRB Cyg X-1 in its high/soft state, and AGN which show similar variability properties, since these states show rather simple $1/f$-type PSD shapes, without complex quasi-periodic oscillations (QPOs). We discuss the implications of our results in Section 4.7 and summarise our results in Section 4.8.

4.3 The Model

The model is based on the scenario proposed by Lyubarskii 1997, where fluctuations propagate inward through the accretion flow, modulating the emission of the inner regions. The fluctuations are produced on time-scales related to the viscous time-scale at the radius of origin and are uncorrelated for different radial scales. This setup produces independent input fluctuations on geometrically spaced time-scales (i.e. evenly spacing of the logarithms of the time-scales, so the time-scales follow a geometric progression). In its simplest realisation, this model reproduces the linear (e.g. PSD $\propto 1/f$) and non-linear (e.g. linear rms-flux relation) general properties of the X-ray light curves, similar to those observed in Cyg X-1 in its high/soft state (e.g. Gleissner et al. 2004), and several AGN (Vaughan et al. 2003; M^{c}Hardy et al. 2004; Uttley & M^{c}Hardy 2005). Churazov et al. (2001) noted that in this class of models, the accretion rate fluctuations can be carried efficiently, and be produced up to high Fourier frequencies, by a geometrically thick accretion flow, identifying it with an extended corona over the thin disc. Kotov et al. (2001) later showed that different radial emissivity profiles for different energy bands emitted by this extended corona would produce time lags and differences between the PSDs of each band.

Recently, King et al. (2004) proposed a mechanism for the production of the fluctuations in Lyubarskii-type models. In their model, chance alignment of the poloidal magnetic fields of the matter settling onto the disc induce outflows that carry away angular momentum, increasing the local accretion rate. This process produces random fluctuations of the accretion rate on radially dependent time-scales, generating an overall variability pattern with $1/f$ type PSDs over a broad range in Fourier frequencies. By following the evolution of the surface density, they showed that the fluctuations propagate with viscous velocity in a wave-like (rather than diffusion-like) fashion.

In the work presented here, we will investigate the properties of a more general scheme to represent a fluctuating accretion flow, without making any initial assumptions as to the nature of the flow, whether it resembles an accreting corona (e.g. Życki et al. 1995), advection dominated accretion flow (ADAF, e.g. Narayan & Yi 1994) or optically thick disc (Shakura & Sunyaev 1973). However, as we will make the assumption that the accretion flow behaves like a standard accretion disc, we will use the term 'accretion disc' and 'accretion flow' interchangeably. We will further allow for models where there is significant damping of inward-propagating fluctuations (e.g. by strong viscous diffusion effects) using a simple approximation. Our main starting assumptions are described below.

4.3.1 Model construction and basic assumptions

We use standard accretion disc (Shakura & Sunyaev 1973) considerations to relate the fluctuation time-scales and propagation speeds to the radial position in the disc, since the same relations are applicable to geometrically thick and optically thin accretion flows as well as standard geometrically thin discs. Following Lyubarskii (1997) We assume that each independent annulus produces a pattern of fluctuations $\dot{m}(r,t)$, having most of the variability power at the local viscous frequency $f_{\rm visc}(r) = r^{-3/2}(H/R)^2\alpha/2\pi$ (e.g Kato et al. 1998), where (H/R) is the disc scale height to radius ratio, α is the viscosity parameter, the radial position r is in units of gravitational radii $R_{\rm g} = GM/c^2$ and the frequency is given in terms of c/RG. Equal variability power in each input signal and geometric spacing of the characteristic frequencies ensure equal power per decade in frequency, producing a power law PSD of slope ~ -1 for the overall accretion fluctuations (before consideration of damping effects).

Following Lyubarskii (1997), the local accretion rate at any radius in the disc is allowed to fluctuate around a value $\dot{M}_o(r,t)$, as $\dot{M}(r,t) = \dot{M}_o(r,t) \times (1 + \dot{m}(r,t))$, where $\dot{m}(r,t) << 1$. As this new value of the accretion rate propagates inward, it serves as the $\dot{M}_o(r,t)$ for the fluctuations produced further in, modulating the higher frequency fluctuations. The propagation speed is assumed to equal the local radial drift velocity $v_{\rm visc}(r) = r^{-1/2}(H/R)^2\alpha$.

A key feature of this model is that the absolute amplitude of accretion rate variations is proportional to the local accretion rate, $\dot{M}_o(r,t)$, at every radius. Considering that the characteristic frequencies of the input fluctuation $\dot{m}(r,t)$ decrease with radius, this implies that the amplitude of high frequency fluctuations is proportional to the actual value of the accretion rate, given by fluctuations on longer time-scales, and this produces the observed linear relation between rms variability and mean flux.

To generate light curves, we assume that the X-rays are emitted by a radially (but not necessarily vertically) extended region. This emitting region might correspond to an accreting corona, possibly sandwiching an optically thick, geometrically thin disc, or be another type of optically thin accretion flow (e.g. ADAF). Having no pre-defined emission mechanism we simply assume that the emitted flux per unit area is proportional to the local accretion rate, which introduces the variability, and to a stable radial emissivity profile. The emissivity profile, $\epsilon(r)$, is taken to follow the radial rate of gravitational energy loss in the accretion disc, $\epsilon(r) = r^{-3}(1 - \sqrt{r_{\rm min}/r})$, where $r_{\rm min}$ is the inner radius of the disc (and of the emission), which we will fix at $6R_{\rm g}$ in our simulations. This profile describes the *total* energy loss. However, as the emitted spectrum might be radially dependent, a given energy band can have a different emissivity profile and so we will use $\epsilon(r) = r^{-\gamma}(1 - \sqrt{r_{\rm min}/r})$ where the emissivity index γ is a tunable model parameter which we can specify to reproduce different spectral-timing properties.

4.3.2 Numerical implementation

For the calculation of the variability patterns, we discretize the models of Lyubarskii (1997) and Kotov et al. (2201) by assuming that a finite number of annuli produce independent fluctuations. These annuli are spaced keeping a constant ratio between consecutive radii, to mimic the behaviour of a continuous accretion flow that produces equal variability power at each radial scale. This geometric spacing of the radii introduces equal power per decade in time-scale, reproducing the $1/f$ PSD shape, as predicted by Lyubarskii (1997).

All independent annuli in the disc are assumed to produce a pattern of small accretion rate fluctuations, $\dot{m}(r,t)$. To meet the requirement of producing most of the variability power at the viscous frequency, these signals are modelled as random fluctuations with a Lorentzian-shaped PSD of variable width, with peak frequency $f_{\rm peak}$ [1] set to equal $f_{\rm visc}$. The width of the Lorentzian is governed by the quality factor Q, equal to the ratio of Lorentzian peak frequency to the full width at half maximum. We used broad input PSDs, with $Q = 0.5$, a value similar to the four-Lorentzian decomposition of the PSD of Cyg X-1 in the low/hard state (Pottschmidt et al. 2003) and also much narrower PSDs with $Q = 10$, to study the influence of this parameters on the final PSDs and Cross Spectra. The normalisation of these signal PSDs was chosen to produce a final fractional variability of the output light curves $F_{\rm var} \sim 10\% - 50\%$, by assigning each of the signals an rms $\sigma_{\rm sig} = \sqrt{F_{\rm var}^2/N}$, where $N \sim 1000$ is the number of independent annuli. We used the method described by Timmer & König (1995) to generate the signal time series $\dot{m}(r,t)$, i.e. by generating periodograms with the underlying signal PSD and the correct statistical properties of a noise process and obtaining $\dot{m}(r,t)$ through their inverse Fourier transform. The resulting $\dot{m}(r,t)$ have zero mean and rms amplitude $\sim \sigma_{\rm sig} \ll 1$.

---

[1] The Lorentzian peak frequency, corresponds to the frequency where the contribution to total rms is at its maximum, and is related to the resonance or centroid frequency $f_{\rm centroid}$ as $f_{\rm peak} = f_{\rm centroid}\sqrt{1 + 1/4Q^2}$ (e.g. see Pottschmidt et al. 2003).

The accretion rate at a given annulus, $\dot{M}(r_i,t)$, is then calculated iteratively as the product of the accretion rate at that position, including its contribution to the fluctuation, $1+\dot{m}(r_i,t)$, by the accretion rate at the annulus lying directly outside, which includes the fluctuations from all outer annuli.

$$\dot{M}(r_i,t) = \dot{M}_o \prod_{j=0}^{i} 1 + \dot{m}(r_j,t), \tag{4.1}$$

so that each $\dot{M}(r_i,t)$ is a flicker noise time series with power law PSD of slope ~ -1 up to $f_{\rm visc}(r_i)$, and shows a linear rms-flux relation.

The effect of the extended emitting region is accounted for when calculating the *light curves*. First, an emissivity index γ is assumed for each energy band. Then, the light curves are constructed by adding the variability patterns $\dot{M}(r_i,t)$ from all annuli, which are weighted by the flux originating from each annulus (i.e. $2\pi r \delta r \epsilon(r)$, where δr is the width of the annulus), and time-shifted by the propagation time of fluctuations from the outermost annulus to the present annulus.

The disc parameters are either kept constant or allowed to vary radially as $(H/R)^2\alpha(r) = Cr^{-\beta}$, where C is a scaling constant and β is an index which governs the radial variation (e.g. constant H/R and α correspond to $\beta = 0$). We will normally use $C = 0.3 \times 6.0^{\beta}$, to produce thick disc parameters $(H/R)^2 = 1$ and $\alpha = 0.3$ at the innermost radius. Radially-varying disc parameters change the radial separation of independent annuli but preserve the separation of independent characteristic frequencies. Therefore, we fix the geometrically spaced frequencies and use $(H/R)^2\alpha(r)$ to calculate the corresponding radii and propagation speeds.

Fig. 4.1 shows a light curve realisation with emissivity index $\gamma = 3$ (a), together with its PSD, plotted as frequency × power (b), and its rms variability amplitude plotted vs the average count rate of short sections of the light curve (c).

Finally, damping of the fluctuations as they propagate through the accretion flow affects the power spectra of the transmitted signals. The magnitude of the damping effect depends on the nature of the fluctuations and their propagation mechanism, which are not specified in our phenomenological model. In their analytical model, Kotov et al. (2001) include this damping effect by using a Green function for diffusion in the geometrically thin disc appoximation. Here, for simplicity and generality, we use a simple prescription for damping by assuming that fluctuations of frequency f are significantly damped after traveling a distance $\Delta r/r = \sqrt{f_{\rm visc}(r)/f}$, so that

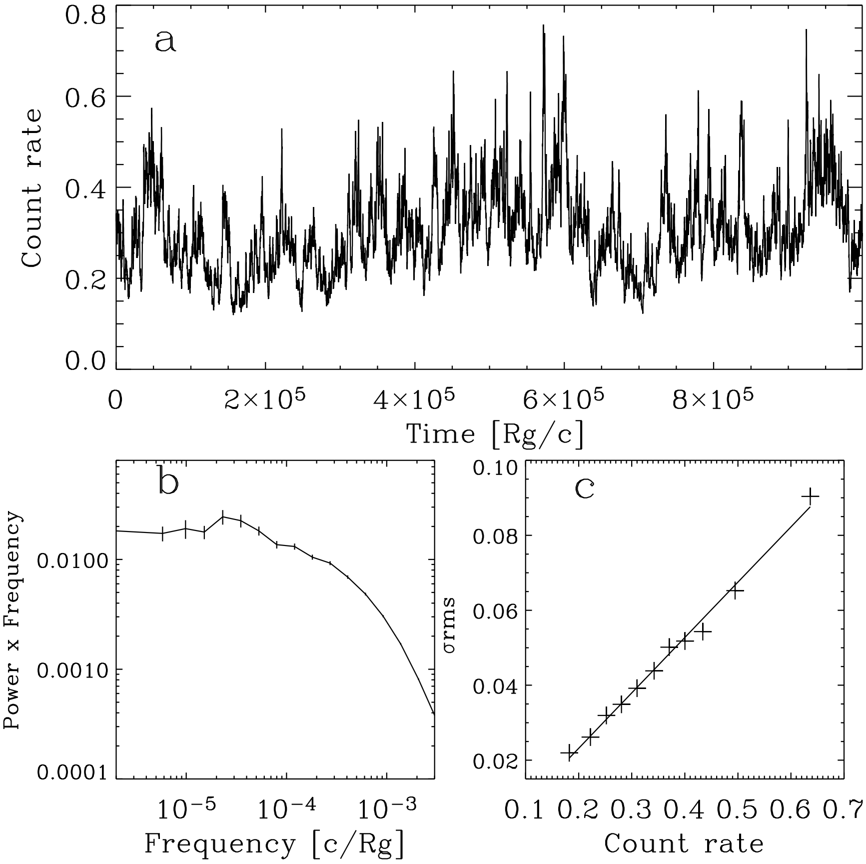

Figure 4.1: a: Lightcurve from a realisation of the variability model, with emissivity index $\gamma = 3$. b: PSD of the same lightcurve, here plotted as power × frequency, showing the typical 1/f shape at low frequencies [i.e. a flat top in this representation, which shows the relative contribution of rms from each decadal range in frequency, analogous to the $\nu F(\nu)$ form of a spectral energy distribution (SED)]. The PSD bends to steeper slopes towards $f_{\rm visc}(r_{\rm min}) = 3 \times 10^{-3} c/R_{\rm g}$. c: $\sigma_{\rm rms}$ vs flux for the same light curve, showing a linear relation.

fluctuations on frequencies much higher than the local viscous frequency are strongly suppressed (see e.g. Churazov et al. 2001, but notice that in that case damping was specifically derived for diffusive propagation of a delta-function shaped impulse in mass accretion rate). The damping prescription is implemented by first taking the Fourier transform of $\dot{M}(r_i,t)$ at each radial step r_i, then multiplying the real and imaginary coefficients of the Fourier transform at each frequency f by a frequency-dependent factor $exp\left(-D\frac{\Delta r}{r_i}\sqrt{\frac{f}{f_{\rm visc}(r_i)}}\right)$ (where the damping coefficient D is a free parameter) and inverse Fourier-transforming the result to get the new, damped $\dot{M}(r_i,t)$.

Throughout this paper we will use $R_{\rm g} = GM/c^2$ as units of distance and $R_{\rm g}/c$ as units of time. For a quick check of frequencies and time-scales note that $R_{\rm g}/c \sim (5M/M_6)s$ where $M_6 = 10^6 M_\odot$, so the frequencies quoted would be in units of Hz for a $2\times10^5 M_\odot$ black hole and units of 10^4 Hz for a $20 M_\odot$ black hole.

4.3.3 Analytical estimates

The extended emitting region acts as a low-pass filter on the PSD. This effect can be understood by considering that the signals at low temporal frequencies are imprinted in the flux from most of the emitting region, while higher frequencies are only imprinted in the emission from smaller, inner, areas. As the lightcurve has additive components from all these regions, this produces comparatively less variability power at high frequencies, creating a bend in the PSD. The 'filtered' PSD can be approximated by multiplying the original PSD(f) by the squared fraction of the total flux that is produced within the characteristic radius r_f of each frequency f as

$$\mathrm{PSD}_{\rm filt}(f) = \mathrm{PSD}(f)\left(\frac{\int_{r_{\rm min}}^{r_f}\epsilon(r)2\pi r dr}{\int_{r_{\rm min}}^{\infty}\epsilon(r)2\pi r dr}\right)^2 \tag{4.2}$$

The filter factor tends to 1 as r_f tends to ∞, i.e. for low temporal frequencies the original variability power is preserved, and decreases monotonically as r_f reaches $r_{\rm min}$, reducing the variability power at the high frequency end. Obviously, as the emissivity profiles $\epsilon(r)$ used are steep, it makes little difference to the filtered PSD if the emission region is truncated at a large radius rather than extending to infinity.

The filtering effect due to the origin of the signals within the emitting region could be easily calculated once the emissivity profile is defined, and its effect is simply to reduce the overall *normalisation* of the contribution to the PSD from each signal (in a frequency-dependent way), without distorting the signal PSD shape. However, the finite travel time of the fluctuations through the emitting region distorts the PSD shape of the input signals, by smoothing out high frequency fluctuations, thus reducing the variability amplitude further, while damping can also affect the low-frequency power. Therefore, the total effective filtering of the underlying fluctuations is quite complex, so we will primarily use numerical simulations to demonstrate its effects in the following section.

The frequency-resolved time lags can be approximated by defining, for each signal s (produced at radius r_s) an 'average travel time', $\bar{\tau}(r_s)$, by weighting the travel time of the fluctuations from r_s to the radius r, $\tau(r, r_s)$ by the emissivity profile $\epsilon(r)$,

$$\bar{\tau}(r_s) = \frac{\int_{r_{\rm min}}^{r_s} \tau(r, r_s)\epsilon(r) 2\pi r dr}{\int_{r_{\rm min}}^{r_s} \epsilon(r) 2\pi r dr}, \tag{4.3}$$

$$\text{where} \qquad \tau(r, r_s) = \int_r^{r_s} \frac{d\tilde{r}}{v_{\rm visc}(\tilde{r})}.$$

If the signals are simple fluctuations on the viscous time-scale only (i.e. defined by a delta-function and not a broad Lorentzian PSD), then r_s can be expressed in terms of frequency and this formula gives the mean travel time as a function of f. Otherwise, if the signals are characterized by broad Lorentzian PSDs, a given temporal frequency will have important contributions from a range in radii r_s. In this case, the mean travel time at a given frequency f is a sum of $\bar{\tau}$ for each contributing (i.e. overlapping) Lorentzian signal PSD, weighted by the variability power at f contributed by that signal.

Time lags between two energy bands appear when they are characterized by different emissivity indices, since this produces different mean travel times for each band. We will use the difference of $\bar{\tau}(f)$ calculated with the corresponding γ indices as an approximation to the time lags between energy bands.

An explicit form for the filter factor of the PSD and for the time lags is given in Appendix A.

4.4 Spectral-Timing Properties

The model was constructed to produce power law-PSD time series that also reproduce the non-linear properties of AGN and BHXRB light curves. The exact PSD shape and spectral-timing properties between different energy bands, depend on a few key model parameters: emissivity indices, disc structure parameters, PSD of the input signals and damping coefficient. Here we will explore how each of these parameters affect the observable properties. An overview of the spectral-timing measurements we use here is provided in Appendix B.

4.4.1 Dependence on emissivity indices

The loss of gravitational energy in the accretion disc requires an energy release per unit area proportional to $\epsilon(r) = r^{-3}(1 - \sqrt{r_{\rm min}/r})$ (Shakura & Sunyaev 1973). A given energy band will have the same radial emissivity profile only if it represents a constant fraction of the emitted flux at each radius. However, following Kotov et al. (2001), to produce the observed hard lags, we assume the emitted spectrum hardens towards the centre, so the actual radial emissivity profile will be steeper for harder bands. We will refer to time series constructed with emissivity index $\gamma = 3$ as the 'soft' light curve and use higher values of γ for the 'hard' bands. In this subsection, we assume the product of disc structure parameters $(H/R)^2\alpha = 0.3$, and that there is no damping ($D = 0$).

The PSD of the final variability pattern at $r_{\rm min}$ for a realisation with input signal $Q = 0.5$, is shown by the solid line in Fig.4.2. This PSD would correspond to an infinitely concentrated emitting region located at $r_{\rm min}$, or equivalently, a compact emitting region located entirely *within* $r_{\rm min}$. It keeps a $1/f$ behaviour (corresponding to a flat top in this plot of power multiplied by frequency) up to $f_{\rm visc}(r_{\rm min}) = 3\times10^{-3}c/R_{\rm g}$, as no annuli contribute with significant variability power above this frequency, the PSD bends downward. The dotted and dashed lines show the PSDs of soft and hard light curves from a realisation with the same underlying accretion fluctuations, with $\gamma_{\rm soft} = 3$ and $\gamma_{\rm hard} = 5$, respectively. The figure highlights the filtering effect of the extended emission on these two light curves, which makes them lose variability power at high frequencies, shifting the bend to lower frequencies. On longer time-scales, all the PSDs flatten to their original slope of -1. The resulting PSDs bend continuously to steeper slopes at high frequencies but, for a limited frequency range, they can be approximated fairly well by a singly bending power law model, as has been used to fit real data. Following e.g. M$^{\rm c}$Hardy et al. (2004), we will use the following bending power law model to fit the PSD,

$$P(f) = Af^{\alpha_L}\left(1 + \left(\frac{f}{f_{\rm b}}\right)^{\alpha_L - \alpha_{\rm H}}\right)^{-1}. \qquad (4.4)$$

	γ	$\alpha_{\rm L}$	$f_{\rm b}$ ($\times 10^{-3}c/R_{\rm g}$)	$\alpha_{\rm H}$
$Q = 0.5$	3	-1.48	1.27	-3.74
	4	-1.22	1.38	-3.54
	5	-1.10	1.54	-3.46
$Q = 10$	3	-1.44	0.80	-4.73
	4	-1.16	0.96	-4.79
	5	-1.02	1.12	-4.86

Table 4.1: Bending power-law model fits to the PSDs of simulated light curves, with emissivity indices γ= 3, 4 and 5, for broad ($Q = 0.5$) and narrow ($Q = 10$) input signal PSDs. Higher γ values, corresponding to higher energy bands, retain more high-frequency power, evident in the flatter low-frequency slope $\alpha_{\rm H}$ and in and higher $f_{\rm b}$ and/or flatter $\alpha_{\rm H}$. The fitting range used was $6 \times 10^{-5} < f < 10^{-2}c/R_{\rm g}$.

Table 4.1 gives the values for the low and high frequency slopes, $\alpha_{\rm L}$ and $\alpha_{\rm H}$ respectively, and the break frequencies $f_{\rm b}$ that result from fitting Equation 4.4 to PSDs with emissivity indices γ= 3, 4 and 5, for broad ($Q = 0.5$) and narrow ($Q = 10$) input signal PSDs. These values depend slightly on the frequency range used for fitting, but reveal the general trend of more high-frequency power for harder energy bands, given by flatter $\alpha_{\rm L}$, and higher $f_{\rm b}$ and/or flatter $\alpha_{\rm H}$.

The emissivity indices γ also define the average travel time of the signals as seen by the different energy bands, so they play a major role in determining the time lags. For emissivity profiles as used here, the lags show an almost power law dependence on frequency, as can be seen in Fig. 4.3. This figure shows, in solid lines, the time lags between a soft light curve with $\gamma_{\rm soft} = 3$ and hard light curves of indices $\gamma_{\rm hard} = 3.5$, 4, 5 and ∞, calculated for $Q = 10$. Obviously, this last light curve, taken to be the variability pattern at $r_{\rm min}$, marks the limiting lag spectrum that can be obtained by increasing $\gamma_{\rm hard}$, assuming the other parameters are fixed at the values given above. The approximate slope of these lag spectra in the range $10^{-5} - 10^{-4}c/R_{\rm g}$ goes from to -0.8 for $\gamma_{\rm hard} = 3.5$ to -0.5 for $\gamma_{\rm hard} = \infty$.

The dotted lines in Fig. 4.3 are the time lags predicted by Eq. 4.3 using the parameters of the corresponding light curve simulations. As these analytic estimates give a good fit to the simulated data, we will use them hereafter on their own or to complement the time lags calculated from simulations.

The magnitude of the time lags increases with the difference between

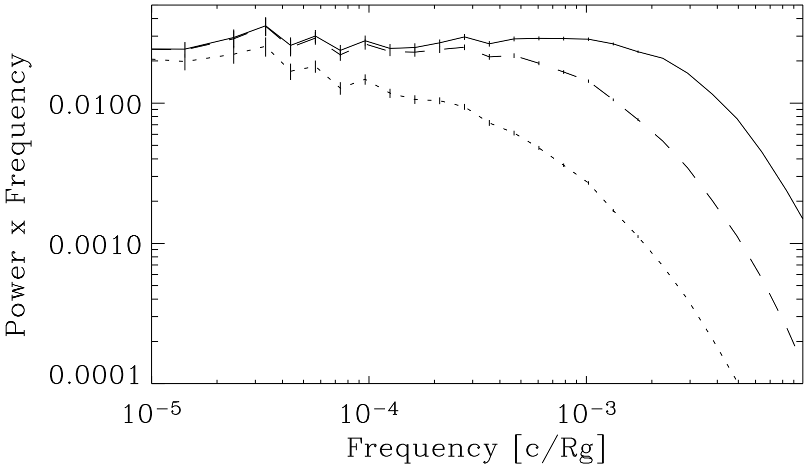

Figure 4.2: Filtering effect of an extended emitting region. The PSD of the variability pattern at the innermost radius, shown in the solid line, keeps a $1/f$ shape up to $f_{\mathrm{visc}}(r_{\mathrm{min}})$. 'Soft' ($\gamma = 3$) and 'hard' ($\gamma = 5$) light curves of the same realisation, in dotted and dashed lines respectively, lose variability power at high Fourier frequencies due to the effect of the extended emitting region. For this realisation we used model parameters $Q = 0.5, \beta = 0, D = 0$.

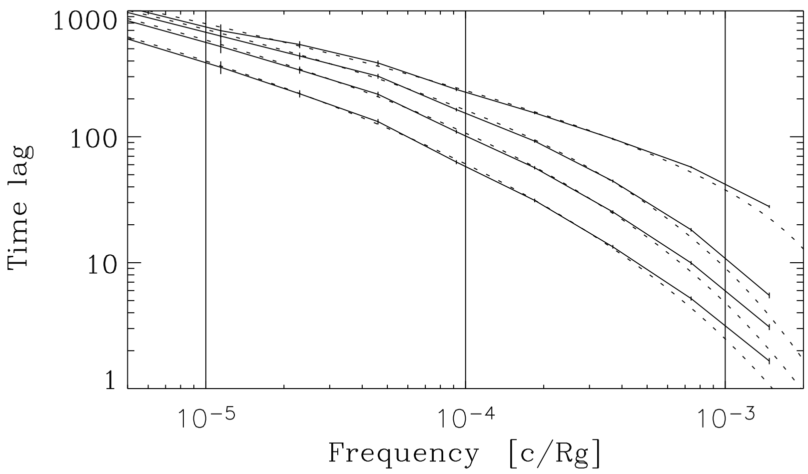

Figure 4.3: Time lags as a function of Fourier frequency, between a soft light curve of emissivity index $\gamma = 3$ and hard light curves of indices $\gamma = 3.5, 4, 5$ and ∞, for $Q = 10$. Larger lags correspond to bigger differences between emissivity indices. The points joint by solid lines represent the values calculated from numerical realisations of the light curves and the dotted lines represent the lags predicted by Eq. 4.3 using the corresponding model parameters. The vertical lines mark the frequencies that will be used in the following two figures to measure lags.

the emissivity indices of the light curves, $\Delta\gamma = \gamma_{\rm hard} - \gamma_{\rm soft}$. Fig.4.4 shows the fractional lags (lag × frequency, i.e. equal to $\phi/2\pi$, where ϕ is the phase lag, see Appendix B in this chapter) at the three Fourier frequencies marked in Fig.4.3 by the vertical lines, $f = 10^{-3}, 10^{-4}, 10^{-5} c/R_{\rm g}$, as a function of $\Delta\gamma$, calculated for narrow input signal PSD, $Q = 10$. Each set of lines was calculated with a fixed value of $\gamma_{\rm soft}$ and varying $\gamma_{\rm hard}$. In all cases, the lags increase rapidly with $\Delta\gamma$ up to $\Delta\gamma \sim 1$. For larger differences in emissivity indices, the lags remain at around $1\% - 10\%$ of the variability time-scale, tending towards the limiting value obtained for $\gamma_{\rm hard} = \infty$. In this figure, for the top panel we used $\gamma_{\rm soft} = 3$ and for the bottom panel, $\gamma_{\rm soft} = 2.5$ (solid lines) and $\gamma_{\rm soft} = 3.5$ (dashed lines). As can be seen, for any $\Delta\gamma$, the lags increase with decreasing $\gamma_{\rm soft}$, i.e. a more extended soft emitting region naturally produces larger lags with respect to all hard bands. Finally, the magnitude of the lags increases with decreasing frequency, but the slope of the lag spectrum is > -1. This translates into smaller fractional lags at lower temporal frequencies.

4.4.2 Disc structure parameters

In our model, the product of disc structure parameters $(H/R)^2\alpha$ can be treated as a single term that governs simultaneously the characteristic frequencies of each radius and the propagation speed. We do not attempt here to model the evolution of the disc structure but only to explore the effect that varying these parameters globally has on the observable quantities. We use the prescription $(H/R)^2\alpha = Cr^{-\beta}$ to treat disc parameters that vary radially. Assuming constant α, a positive value of β implies that the accretion flow flattens outwards, approximating the case of a thin disc that expands into a thick disc or ADAF-type flow towards the centre. We have used $(H/R)^2\alpha = 0.3$ at $r_{\rm min}$. Assuming $\alpha = 0.3$, this corresponds to a geometrically thick disc. The motivation for assuming this large value for $(H/R)^2\alpha$ is the need to maximize the characteristic frequencies of the innermost input signals, as the data can show significant variability up to the orbital time-scale of the last stable orbit.

Varying β changes the spacing of the radii that correspond to independent characteristic frequencies, but not the spacing of the frequencies themselves. The variability pattern at each independent annulus is not affected, but the position of each annulus in the disc shifts. Therefore, the final light curves are affected only through the effects of the extended emitting region, as the emissivity of each annulus and the travel time between them changes. The overall effect on the PSDs is a small decrease in power towards high

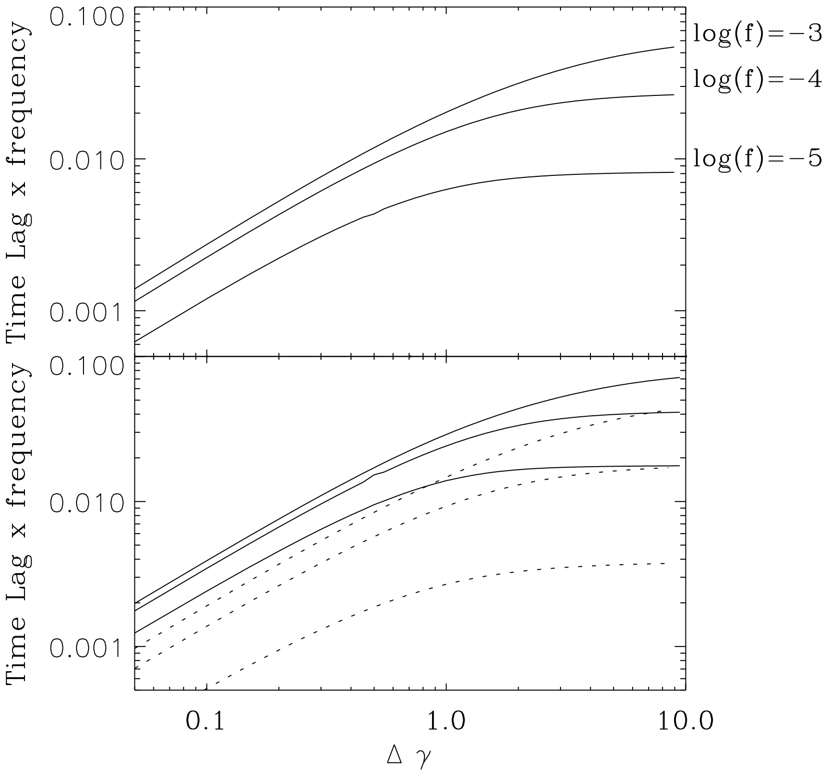

Figure 4.4: Top panel: Fractional time lags (lags × frequency) for energy bands of emissivity index *difference* $\Delta\gamma = \gamma_{\rm hard} - \gamma_{\rm soft}$, with $\gamma_{\rm soft} = 3$, measured at three temporal frequencies, $f = 10^{-3}, 10^{-4}, 10^{-5} c/R_{\rm g}$. The lags increase with the difference in emissivity indices and depend sensitively on this parameter up to $\Delta\gamma \sim 1$, for larger differences the lags remain at around $1\% - 10\%$ of the Fourier frequency. As the slope of the lag spectra is greater than -1, fractional lags are smaller at low frequencies. Bottom panel: Same as above but using $\gamma_{\rm soft} = 2.5$ (solid lines) and $\gamma_{\rm soft} = 3.5$ (dashed lines), a steeper emissivity profile for the soft band produces smaller lags for the same difference in indices. In both panels the lags were calculated for narrow input signal PSDs, with $Q = 10$. The value of Q affects mainly the lags at high frequencies, the lags at 10^{-5} and $10^{-4} c/R_{\rm g}$ in these plots are almost independent of the Q-value used.

frequencies, produced by a steeper low-frequency PSD slope (see Table 4.2).

The amplitude of the time lags remains approximately unchanged, for the frequency range studied ($10^{-3} - 10^{-5} c/R_{\rm g}$), but the slope of the lag spectra steepens. For $\beta = 1$ and $\gamma_{\rm soft} = 3$, the lag spectrum slope in the frequency range $10^{-5} - 10^{-4} c/R_{\rm g}$ goes from -1.0 for $\gamma_{\rm hard} = 3.5$ to -0.7 for $\gamma_{\rm hard} = \infty$ (c.f. the equivalent values for $\beta = 0$ of -0.8 and -0.5 respectively). The top panel in Fig. 4.5, shows the fractional lags as a function of $\Delta\gamma$ for $\gamma_{\rm soft} = 3$ and $\beta = 1$. Evidently, these functions are very similar to the $\beta = 0$ case shown in the top panel of Fig. 4.4, having only slightly lower lags at high frequencies and higher lags at low frequencies.

Changing the scaling constant C to lower values, i.e. as in a thinner disc, shifts all the time-scales up by the same factor. This effect shifts the PSD to lower frequencies without changing its shape. The lower panel in Fig.4.5 shows the fractional time lags as a function of $\Delta\gamma$ for $\beta = 0$ and $(H/R)^2\alpha = 0.03$ instead of $(H/R)^2\alpha = 0.3$, used in all previous cases. The fractional lag spectrum is equivalent to the case with $(H/R)^2\alpha = 0.3$ (top panel in Fig. 4.4) except shifted down a factor of 10 in frequency, so the absolute value of the lag at a given frequency is a factor of 10 higher than for $(H/R)^2\alpha = 0.3$. Notice however, that as the PSD also shifts in frequency, the fractional lags at, for example, the break frequency remain approximately the same.

4.4.3 Input signals

So far we have mainly considered light curves whose input signals have a Lorentzian PSD of quality factor $Q = 10$. As this shape is quite arbitrary, it is important to estimate the influence of the signal PSD on the observable parameters.

If the input signal PSDs are narrow, there is little variability power above $f_{\rm visc}(r_{\rm min})$ and the final PSD bends down sharply above this frequency, whereas broader input signal PSDs spill power up to higher frequencies making this drop less pronounced. Fig. 4.6 shows the PSDs of soft and hard light curve pairs from two realisations with different Q values for the signal PSDs. For each emissivity index, the broad- and narrow-input-PSD realisations, plotted in dashed and solid lines respectively, have similar final power spectra, only differing noticeably near $f_{\rm visc}(r_{\rm min}) = 3\times10^{-3} c/R_{\rm g}$. The same results are obtained from changing the signal PSD to, for example, a doubly-broken power law. The $1/f$ behaviour of the low frequency PSDs is produced by using equal rms per input signal and geometric separation of the signal characteristic frequencies (i.e. Lorentzian peak frequencies), and

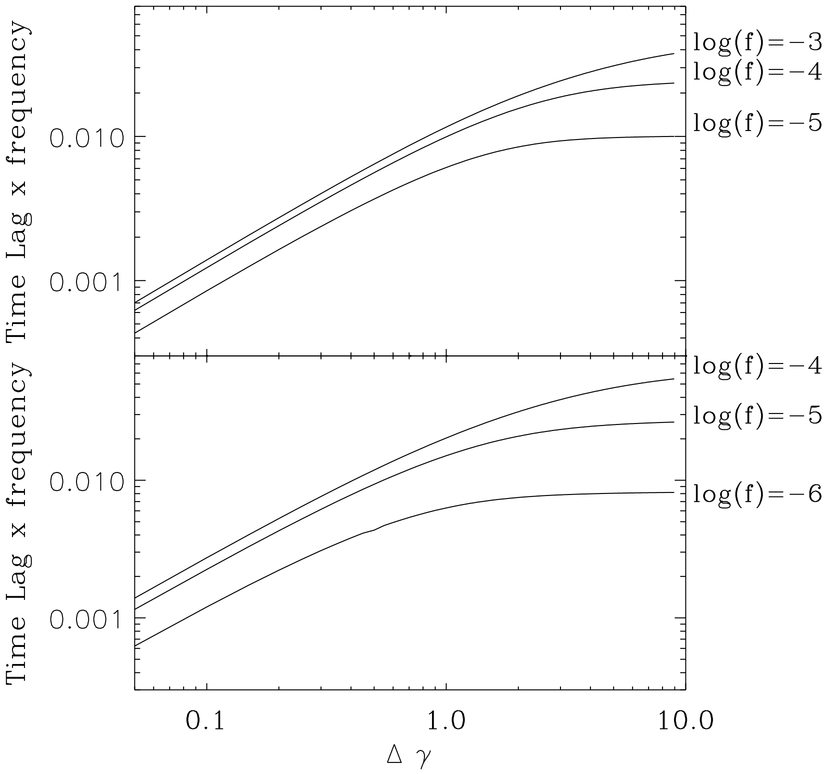

Figure 4.5: Top panel: Same as top panel of Fig. 4.3 but using $\beta = 1$, i.e. constant $(H/R)^2\alpha$. The lags are similar to the $\beta = 0$ case but the slope of the lag spectrum is closer to -1, so the fractional lags have approximately the same value at all Fourier frequencies. Bottom panel: Same as top panel of Fig. 4.3 (using $\beta = 0$) but using $(H/R)^2\alpha = 0.03$. The lags are equivalent to the case with $(H/R)^2\alpha = 0.3$ (top panel in Fig. 4.4) but for frequencies a factor of 10 lower. In both panels the lags were calculated for narrow input signal PSDs, with $Q = 10$.

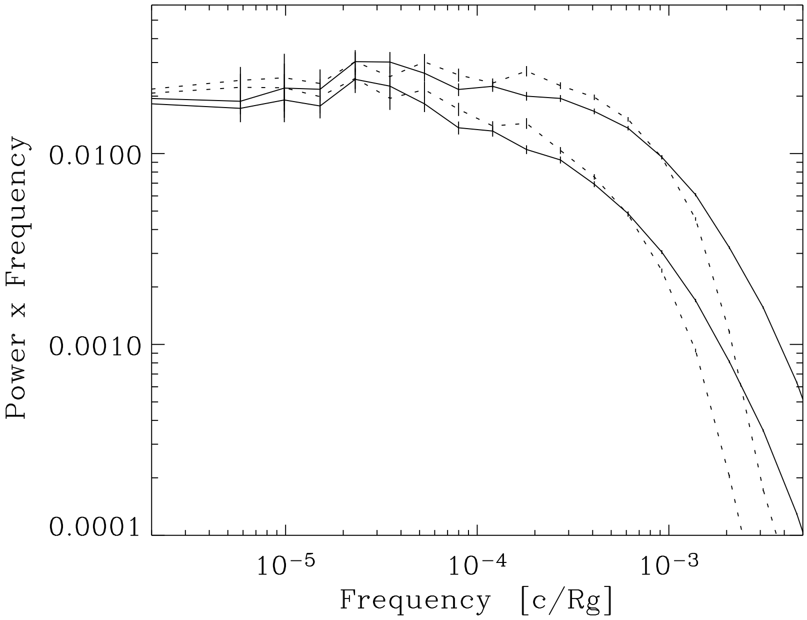

Figure 4.6: PSDs of soft ($\gamma = 3$, bottom) and hard ($\gamma = 4$, top), of two model realisations, with input signal PSD quality factor $Q = 0.5$ (in solid lines) and $Q = 10$ (dotted lines). The light curves with $Q = 10$ drop-off more sharply than their $Q = 0.5$ counterparts close to the maximum frequency $f = 3 \times 10^{-3} c/R_{\rm g}$. At lower frequencies both realisations follow a $1/f$ relation.

does not depend on the shape of the signal PSDs. On the other hand, the signal PSDs define the high frequency slope, so this part of the final PSD can serve as a diagnostic for the intrinsic variability process.

The signal PSD also affects the high frequency end of the lag spectra. Fig. 4.7 shows how time lags drop off less sharply for a broad-PSD signal. At low frequencies, however, there is no evident dependence of time lag on signal PSD.

The signal PSD has a stronger effect on the coherence between two energy bands. For broad signal PSDs, a given temporal frequency will have contributions from several (incoherent) signals produced by different annuli. As the different emissivity indices highlight differing regions of the disc, the coherence between the corresponding energy bands can drop. This is shown in Fig. 4.8, where we plot the coherence for light curves with broad

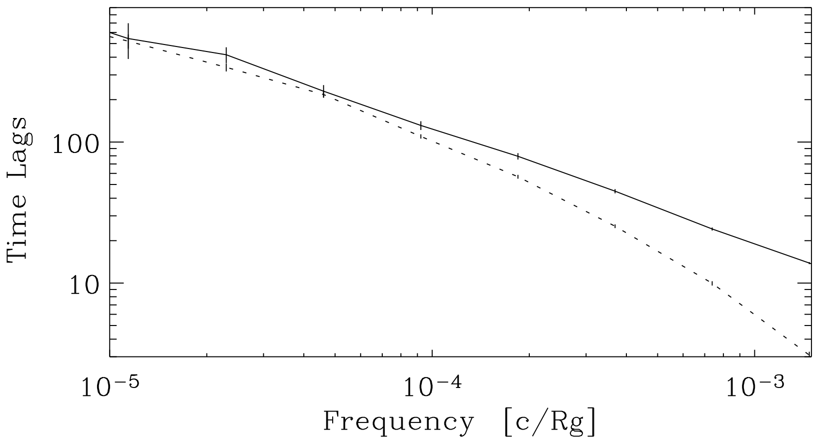

Figure 4.7: Time lags between soft ($\gamma = 3$) and hard ($\gamma = 4$) light curve pairs with input-signal PSD quality factors $Q = 0.5$ (top), $Q = 10$ (bottom). Broader-PSD signals increase the time lags close to the maximum frequency.

($Q = 0.5$) and narrow ($Q = 10$) signal PSDs, using dotted and dashed lines respectively. As expected, broader signal PSDs produce a stronger drop. Notice however, that in either case this loss of coherence is at most a few per cent. The emissivity indices have a much stronger effect on the coherence. For Fig. 4.8 we used $\gamma_{\rm soft} = 3$ and $\gamma_{\rm hard} = 4$. The same plot calculated for $\gamma_{\rm soft} = 3$ and $\gamma_{\rm hard} = 5$ would show a drop of up to 7 per cent, and for $\gamma_{\rm soft} = 3$ and $\gamma_{\rm hard} = \infty$, of 40 per cent, for lightcurves with $Q = 0.5$.

4.4.4 Damping

The effect of damping is to reduce the amplitude of the fluctuations as they propagate inward so that the farther they go the smaller they get. An immediate consequence is the reduction of variability power at all frequencies as seen in the PSD. As this suppression is frequency dependent, damping can change the shape of the PSD. Fig. 4.9 shows the PSD for four hard light curves ($\gamma = 4$) with equal disc parameters and input signal variability amplitudes, but affected by different degrees of damping. The most noticeable change is the overall reduction of variability power. However, as the input rms is arbitrary, this effect does not help to quantify the amount of damping affecting real data. A more important effect is the change in the low frequency slope, as damping can produce values of $\alpha_{\rm L} < -1$, as seen in

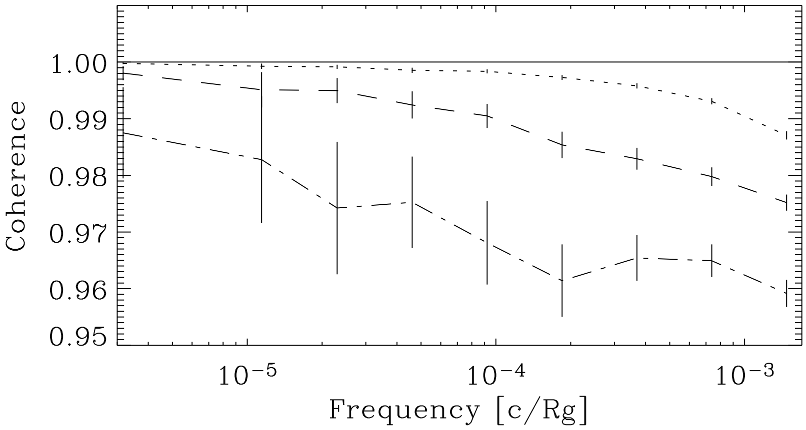

Figure 4.8: Coherence between soft ($\gamma = 3$) and hard ($\gamma = 4$) light curve pairs, with Lorentzian input signal PSDs with quality-factors $Q = 10$ (dotted line), and $Q = 0.5$ (dashed line). The light curves with broader input-signal PSDs show a stronger loss of coherence. The dot-dashed line corresponds to a $Q = 0.5$ light curve pair affected by damping ($D = 1$), which reduces the coherence by a few extra per cent. For comparison, coherence = 1 is shown by the solid line.

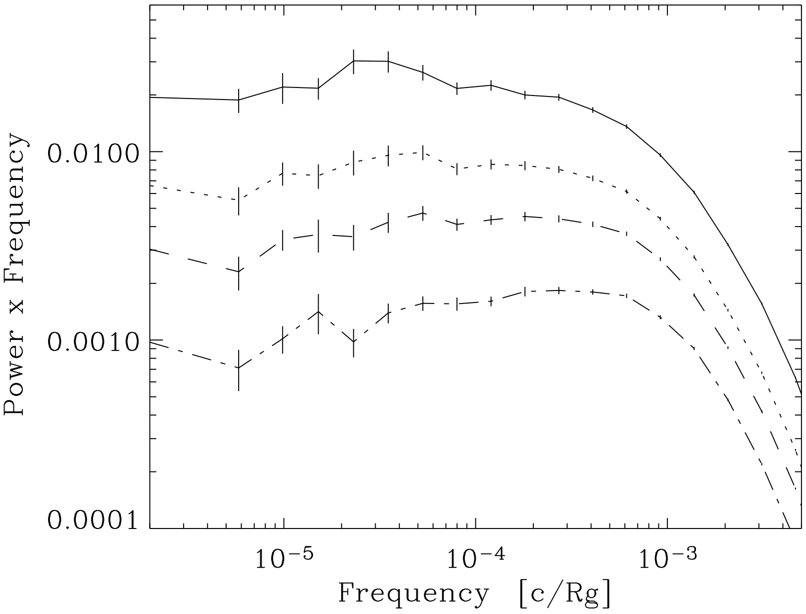

Figure 4.9: Effect of damping on the PSD. The solid line shows the PSD of a ($\gamma = 4$) light curve calculated without damping. The dotted, dashed and dot-dashed lines shows the PSDs of similar light curves calculated with damping coefficients D=0.5, 1 and 2, respectively. Damping reduces the overall power but acts more strongly on the lowest frequencies so the low frequency slope α_{L} flattens.

e.g. MCG-6-30-15 (M$^{\mathrm{c}}$Hardy et al. 2005). Table 4.2 shows the values of α_{L} for damping coefficients $D = 0, 0.5, 1$ and 2, for different emissivity indices. In all cases, the stronger damping flattens the low frequency PSD, by similar values regardless of γ, e.g. for $D = 2$ compared to $D = 0$, $\Delta\alpha_{\mathrm{L}} \sim 0.17$ for $\beta = 0$ and $\Delta\alpha_{\mathrm{L}} \sim 0.1$ for $\beta = 1$.

Damping can also reduce the coherence, especially in the case of broad input signal PSDs. The dot-dashed line in Fig. 4.8, shows the coherence for light curves of emissivity indices $\gamma_{\mathrm{soft}} = 3$ and $\gamma_{\mathrm{hard}} = 4$, $Q = 0.5$ and damping coefficient $D = 1$. These light curves only differ from those corresponding to the dashed line on the same plot by the effect of damping, which increases the loss of coherence at the highest frequency bin from 2 to 4 per cent. Again, a larger difference in emissivity indices makes this drop more pronounced, and damping effects increase these losses accordingly:

			α_L		
Model	D	β	$\gamma = 3$	$\gamma = 4$	$\gamma = 5$
1	2	0	-0.98	-0.83	-0.80
2	2	1	-1.19	-0.99	-0.90
3	1	0	-1.04	-0.89	-0.86
4	1	1	-1.24	-1.04	-0.95
5	0.5	0	-1.09	-0.94	-0.90
6	0.5	1	-1.26	-1.07	-0.98
7	0	0	-1.14	-1.00	-0.96
8	0	1	-1.29	-1.10	-1.02

Table 4.2: Low Fourier frequency slopes, α_{L}, fit to PSDs of light curves generated with damping coefficients D and radial dependence of the disc parameters given by β as described in the text, for emissivity indices $\gamma = 3, 4$ and 5. The fits are carried out only for data below $f = -3 \times 10^{-4} c/R_{\mathrm{g}}$.

for $\gamma_{\mathrm{soft}} = 3$ and $\gamma_{\mathrm{hard}} = 5$ the coherence at the highest frequency bin drops by ~ 12 per cent and for $\gamma_{\mathrm{soft}} = 3$ and $\gamma_{\mathrm{hard}} = \infty$, by 60 per cent. Finally, damping can produce slightly steeper lag spectra, reducing the lags at high frequencies. This effect is small: damping coefficients of $D = 0$ and $D = 1$ produce lags differing by a factor of < 1.5 at frequencies close to the measured break-frequency f_b and less at lower frequencies.

4.5 Comparison with AGN X-ray light curves

AGN X-ray light curves from long monitoring campaigns typically show power law PSDs with a slope ~ -1 at low frequencies, bending or breaking at high frequencies to slopes~ -2 or steeper (e.g. Uttley, M$^{\mathrm{c}}$Hardy & Papadakis 2002; Markowitz et al. 2003; M$^{\mathrm{c}}$Hardy et al. 2004; M$^{\mathrm{c}}$Hardy et al. 2005; Uttley & M$^{\mathrm{c}}$Hardy 2005). The high-frequency PSD is energy dependent, with higher energy PSDs showing a higher break frequency and/or flatter slopes above the break, depending on model assumptions (e.g. M$^{\mathrm{c}}$Hardy et al. 2004). Significant frequency-dependent time lags have been measured in a few AGN [NGC 7469 Papadakis et al. (2001); MCG-6-30-15 Vaughan et al. (2003); NGC 4051 M$^{\mathrm{c}}$Hardy et al. (2004); NGC 3783 Markowitz (2005)]. In all cases, these lags increase with time-scale and energy separation of the bands and show magnitudes of up to a few percent of the variability time-scale. The measured coherence is usually high (> 0.9) up to about the break frequency, sometimes dropping by tens of per cent above the break

(Vaughan et al. 2003; M^{c}Hardy et al. 2004). This behaviour is qualitatively consistent with the predictions of the fluctuating accretion model outlined in Section 4.4. Now we will compare the model predictions directly to AGN data to check this consistency quantitatively.

4.5.1 Time lags

The time lags in NGC 4051 reported by M^{c}Hardy et al. (2004) are among the largest measured in AGN, with values of $\sim$ 0.25, 2.5 and 4.5 per cent of the variability time-scale, when calculated between the 0.1-0.5 keV band and the 0.5-2, 2-5 and 5-10 keV bands, respectively. The slopes of the lag spectra are not well constrained but are consistent with -1. To reproduce these large lags with the model, we chose a fairly extended soft emitting region, with emissivity index $\gamma_{\rm soft} = 2.5$, assumed $(H/R)^2\alpha = 0.3$ at $r = 6$, and used a value of $\beta = 1$ to produce a lag-spectrum slope ~ -1, and used $D = 0$. Using Eq. 4.4, we calculated the lag spectra for these model parameters, choosing emissivity indices for the remaining energy bands to match the observed lags. We used $Q = 1$ for the calculation, although other Q values produce equally good fits as the width of the input signal PSD has a very small effect in the lag spectrum over the frequency range used here (see Sec. 4.4.3). The resulting lag spectra for $\gamma_{\rm hard}$=3.3, 5.5 and ∞ are shown in Fig. 4.10, in dotted, solid and dashed lines, respectively. To convert light-crossing times to seconds, we assumed a mass of $5 \times 10^5 M_{\odot}$ (Shemmer et al. 2003). Overlaid in this figure, we show the lags measured from *XMM-Newton* data for NGC 4051 , where the observed light curves were constructed as described in M^{c}Hardy et al. (2004). Although the errors on the data are large, it is clear that the chosen model parameters are consistent with the amplitude, slope and energy dependence of the measured lags.

4.5.2 Energy dependence of the PSD

NGC 4051 was monitored with *RXTE* and *XMM-Newton* on long and short time-scales respectively by M^{c}Hardy et al. (2004), producing a well sampled PSD over 6 decades in frequency. The high frequency PSD in NGC 4051 shows strong energy dependence, varying from a slope $\alpha_{\rm H} = 2.91 \pm 0.12$ in the 0.1-0.5 keV band to $\alpha_{\rm H} = 2.06 \pm 0.16$ in the 2-5 keV band.

The difference in emissivity indices for these energy bands, suggested by the lag spectra, can also explain the energy dependence of the high frequency PSD slope. To measure the energy dependence we produced model light

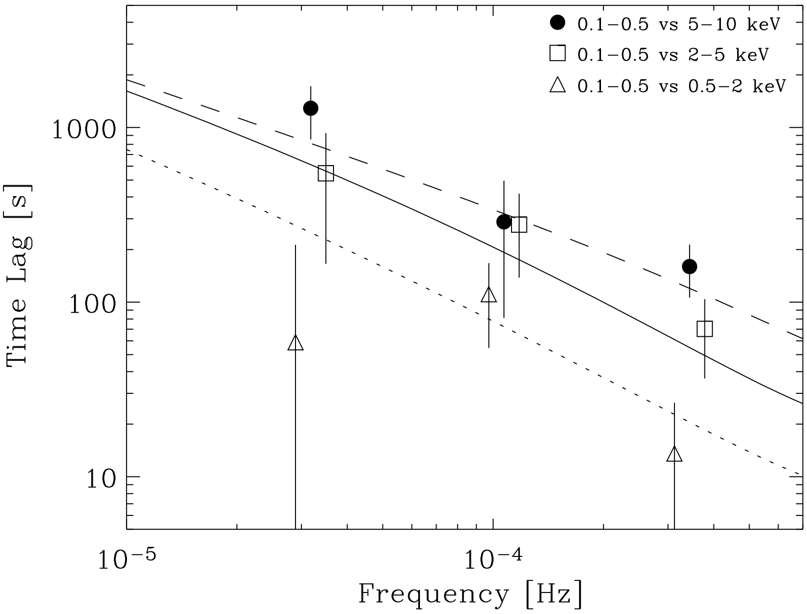

Figure 4.10: Time lags between the 0.1-0.5 keV band and 0.5-2, 2-5 and 5-10 keV bands (triangles, open squares and filled circles respectively), for NGC4051 *XMM-Newton* data. The lines represent the model lags calculated using Eq. 4.3 with model parameters fitted to match the observed PSDs as described in the text. The dotted, solid and dashed lines were calculated between synthetic light curves with emissivity indices $\gamma_{\rm soft} = 2.5$ and $\gamma_{\rm hard} = 3.3, 5.5$ and ∞, and $\beta = 1$, assuming a black hole mass of 5×10^5 $M_\odot$. The filled circles are placed at the correct frequency used for the three data sets, while the squares and triangles have been shifted in this plot to slightly lower and higher frequencies respectively, to avoid overlappingx the error bars.

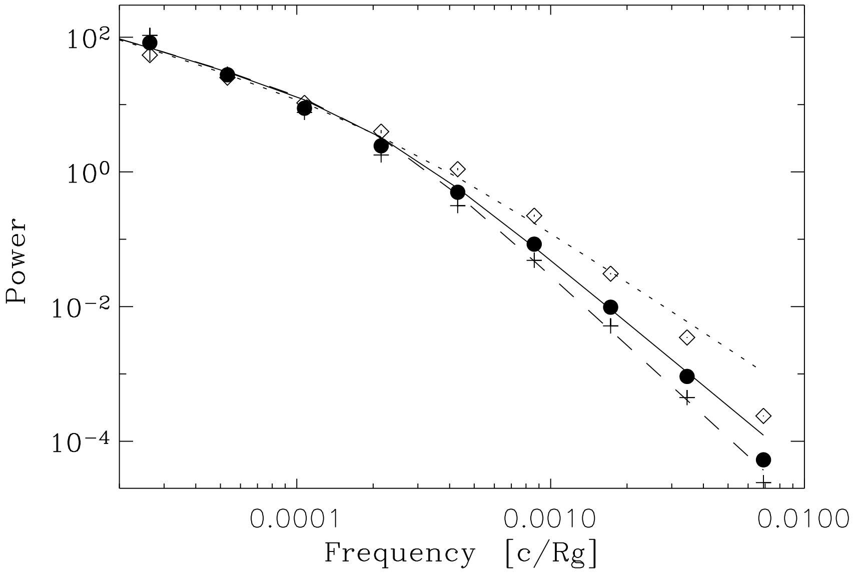

Figure 4.11: PSDs of three synthetic light curves of emissivity indices $\gamma = 2.5, 3.3$ and 5.5 in crosses, filled circles and open diamonds, respectively, calculated with $(H/R)^2\alpha = 0.3$, $D = 0$, $r_{\text{min}} = 6$ and $Q = 1$. The lines mark the bending power law model fit to each PSD in the frequency range shown, with fixed $\alpha_{\text{L}} = -1.1$ and $f_{\text{b}} = 2 \times 10^{-4} c/R_{\text{g}}$. The PSD and model normalisations have been rescaled to match at the low frequency end. The PSD of model light curves can be fitted approximately with a bending power law of fixed α_{L} and f_{b}, which highlights the differences in the high frequency slope.

curves with broad input signal PSDs, $Q = 0.5$, and model parameters as described above and fitted the final PSD with a bending power law model. To make a fair comparison with the data, we followed the procedure used by M$^{\mathrm{c}}$Hardy et al. (2004) by fixing the low-frequency slope α_{L} to -1.1 and the bend frequency f_{b} to the best fitting value for an intermediate emissivity index, and fitted the simulated PSDs over a similar range in frequencies. Using again $\gamma_{\mathrm{soft}} = 2.5$ for the 0.1-0.5 keV and $\gamma_{\mathrm{hard}} = 5.5$ for the 2-5 keV band, we obtained PSDs that differ by $\Delta\alpha_{\mathrm{H}} = -0.95$, spanning a similar range to that measured for the real data, $\Delta\alpha_{\mathrm{H,NGC}} = -0.85 \pm 0.2$. The resulting PSDs and bending-power law fits are shown in Fig. 4.11, for emissivity indices $\gamma = 2.5$, 3.3 and 5.5. Notice that in this figure the PSD normalisations have been rescaled to match at the low frequency end, to highlight the different changes in slope. The filled circles in this figure correspond to $\gamma = 3.3$, which would represent the 0.5-2 keV band, as seen in Section 4.5.1. Correspondingly, the difference in high frequency PSD slope between the $\gamma = 2.5$ and $\gamma = 3.3$ light curves is $\Delta\alpha_{\mathrm{H}} = -0.34$, placing the $\gamma = 3.3$ light curve between the 0.5-1.0 keV ($\Delta\alpha_{\mathrm{H,NGC}} = -0.25$) and 1.0-2.0 keV ($\Delta\alpha_{\mathrm{H,NGC}} = -0.54$) bands.

To check the consistency of the time-scales, we compared the bend frequency $f_{b,NGC}$ measured by M$^{\mathrm{c}}$Hardy et al. (2004), using the combined *RXTE* and *XMM-Newton* light curves, to model light curves covering a similar range in frequencies. As the NGC 4051 data used for this fit corresponded to the 4–10 keV *XMM-Newton* band, we used the 'hard' simulated light curves with γ between 5.5 and ∞. The best fit bend frequencies for $\gamma = 5.5$ and ∞, respectively, are 4.6×10^{-4} and $2 \times 10^{-3} c/R_{\mathrm{g}}$. Equating these values to $f_{b,NGC} = 5 \times 10^{-4}$ Hz yields a mass of $2 - 8 \times 10^{5} M_{\odot}$, consistent with the NGC 4051 reverberation mapping mass of $5^{+6}_{-3} \times 10^{5} M_{\odot}$ (Shemmer et al. 2003).

A similar energy dependence of the PSD has been found in other AGN. As an example, the PSD of the Seyfert 1 galaxy MCG-6-30-15 can also be fit with a bending power law model obtaining flatter high-frequency slopes for higher energy light curves (Vaughan et al. 2003). The energy dependence in this case is less pronounced than in NGC 4051, possibly suggesting that the energy bands used have closer emissivity indices. Incidentally, emissivity indices that are closer in value would also produce smaller time lags, as observed in MCG-6-30-15. However, more parameters contribute to define the observed lags, for example, the mass of the central object changes the frequency range probed in terms of the light crossing times. Therefore, simple lag measurements cannot be translated directly into intrinsic differences in emissivity between the objects without accounting for these effects.

4.5.3 Cross correlations

In most cases, AGN light curves are not densely sampled enough to produce reliable cross-spectra, but lags and coherence can be crudely estimated with the cross-correlation function (CCF). Time lags between two bands can translate into a shift of the CCF central peak if one light curve is a simple translation in time of the other, or produce an asymmetric peak if the lags are more complex. Fourier frequency dependent time lags, as produced by the model and seen in some AGN, produce skewed CCFs with centroids shifted to positive lags, meaning that the soft band leads the hard one. The CCF peak can remain close to zero lag because the lags associated with the narrow-width (i.e. short time-scale) CCF components are small. However, longer time-scale components are separated by progressively larger lags, producing noticeably better correlations at positive than at negative lags, so the CCF becomes skewed.

As an example, Fig. 4.12 shows a set of auto-correlation Functions (ACF) and CCFs for MCG-6-30-15. In this figure, solid lines represent the ACF for the soft band (0.5-0.7 keV) of three light curves, each approximately 100 ks long, taken by *XMM-Newton* during revolutions 301, 302 and 303. These data were first discussed by Fabian et al. 2002) and we followed the procedure described therein to construct the light curves. The dotted and dashed lines represent the CCF between this soft light curve and the medium (0.7-2.0 keV) and hard (2.0-10.0 keV) light curves. The CCFs are slightly asymmetric and this asymmetry increases with the energy separation of the bands, as would be expected from the lag spectrum results obtained by Vaughan et al. (2003) for the same data set. Notice, however, that in orbit 302 the CCFs are skewed towards negative lags (i.e. soft band lagging hard), contrary to what is seen in the other two orbits and what is obtained from the averaged lag spectra. As we will see, this anomaly can easily result from statistical fluctuations inherent in the variability process (and not associated with any changes to the emitting region), and highlights one of the caveats that must be borne in mind when using the CCF alone to determine time lags.

We used the variability model to produce synthetic light curves that match the MCG-6-30-15 PSD at low and high frequencies (M^{c}Hardy et al. 2005) and the PSD energy dependence and time lags (Vaughan et al. 2003). The smaller energy dependence and lags in this object, compared to NGC 4051, can be reproduced with closer emissivity indices, where values of $\gamma = 3$, 4 and 5 were appropriate to fit the soft, medium and hard bands used above. We used short segments of these simulated light curves to

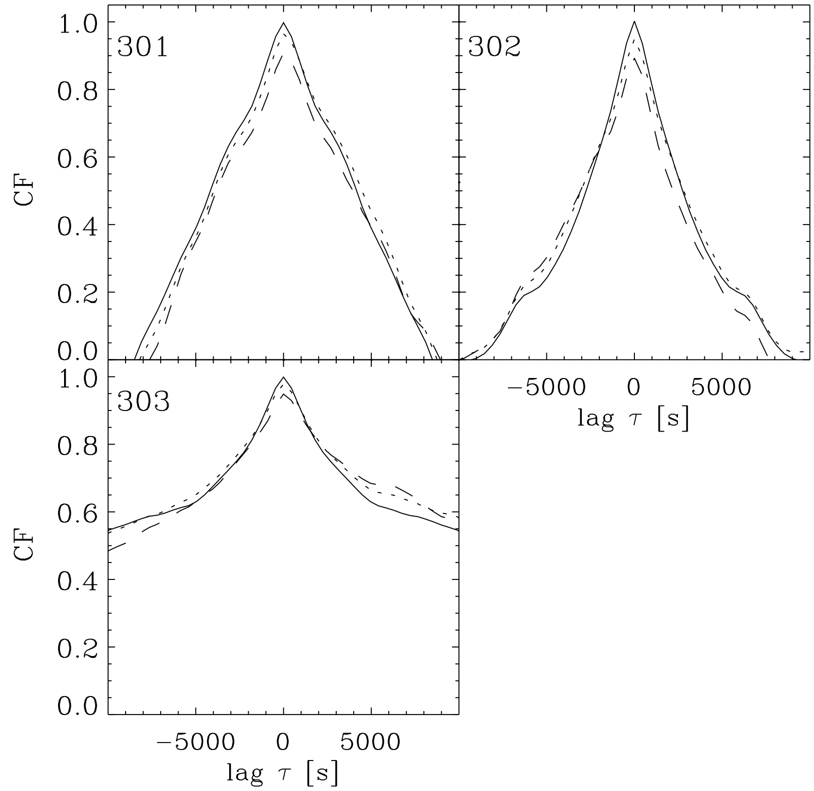

Figure 4.12: Auto- and cross-correlation functions for three, 100 ks long, observations of MCG-6-30-15 taken by *XMM-Newton* during orbits 301, 302 and 303. The solid line shows the ACF of the soft (0.5-0.7 keV) light curve, the dotted- and dashed-lines represent the CCF between this and the medium (0.7-2.0 keV) and hard (2.0-10.0 keV) light curves respectively. A CCF centroid displaced to positive lags indicates that the soft band leads the harder band.

compute ACFs and CCFs, to compare with the results of the real data. The segments used were $\sim 10^4 R_\mathrm{g}/c$ long, which equals 100 ks for a $2\times10^6 M_\odot$ BH, similar to the mass estimated for MCG-6-30-15 by M$^\mathrm{c}$Hardy et al. (2005) of $3-6\times10^6 M_\odot$. The ACFs for the $\gamma = 3$ synthetic light curve segments and the CCF between these and the $\gamma = 4$ and 5 segments are displayed in Fig. 4.13, in solid, dashed and dotted lines, respectively. This figure shows that the model can reproduce the asymmetry in the CCF and its energy dependence, but also that quite different CCF characteristics can be expected from the same underlying model parameters.

One thing to note when calculating the ACF of short stretches of *red-noise* light curves is that the width of the central peak varies. This is a consequence of the stochastic nature of the time series and does not necessarily imply a change in the underlying physical conditions. The different ACF central peaks shown in Fig. 4.13 are calculated from segments of a single long (stationary) synthetic light curve. The segments are $10^4 R_\mathrm{g}/c$ long, covering the frequency range around and above the bend in the PSD. Evidently, the same set of underlying model parameters can produce considerably different peak widths.

Secondly, the shift in the CCF centroid can change artificially from positive to negative lags. The time lags produced by the model are strictly positive, as the fluctuations propagate only inwards and harder bands are more centrally concentrated (see Equation 4.3). This produces CCFs skewed towards positive lags. This effect can be seen in the dotted and dashed lines in Fig. 4.13, that represent the CCFs between light curves of indices $\gamma_\mathrm{soft} = 3$ and $\gamma_\mathrm{hard} = 4$ and 5 respectively. In panels a, c and d, the CCF are better correlated at positive than at negative lags, and this positive asymmetry indicates that the 'hard' light curve lags the 'soft', as expected.

However, it happens occasionally that different fluctuations align by chance, and can make the hard light curve correlate with the soft one better at a negative lag. If this happens at low Fourier frequencies, where the amplitude of the fluctuations is largest, it can cause the CCF centroid to flip to negative lags, as in panel b of Fig. 4.13. A negative lag centroid occured for approximately one quarter of the segments of this length and for 5% of the cases where segments 10 times longer were used. Fig. 4.14 shows the lag spectra corresponding to panels a and b of Fig. 4.13, in solid lines, and the lag spectrum of the full synthetic light curves in dashed lines, all these calculated for $\gamma_\mathrm{soft} = 3$ and $\gamma_\mathrm{hard} = 5$. The large scatter around the underlying lag spectrum is caused only by the small number of points used in the short light curves, as these have no added observational noise. In panel a, the lags follow the underlying spectrum, and so, the corresponding CCF in Fig. 4.13 shows the expected positive-lag asymmetry, while the negative-lags seen in panel b of Fig. 4.13 are caused by the largely outlying lag value at the lowest frequency bin in Fig. 4.14 panel b. In conclusion, the slight asymmetry of the MCG-6-30-15 CCFs and the reversal of the lag sign in the data from orbit 302 can be accounted for by the variability model, without needing to invoke additional effects of, e.g. spectral evolution of the emitting region. A comparison of the fractional lags at, for example, the PSD bend frequency in each case gives a mass-independent measure, so an extrapolation of the lag spectra in NGC 4051 published by M^{c} Hardy et al. (2004) down to the break time-scale would suggest that the lags in this case are indeed systematically larger than in MCG-6-30-15

4.6 Application to Cyg X-1 data

We now apply our simple model to data from the well-studied, persistent black hole XRB Cyg X-1, in the high/soft state.

Our model produces light curves with a $\sim 1/f$ PSD shape down to low frequencies. This is because we assume that the input signals originate at many different radii throughout the accretion disc, are equally separated in the logarithm of frequency and have identical rms amplitudes of variability. PSDs of this shape are seen for several AGN (see previous section) and Cyg X-1 in its high/soft state.

We will use data from a short (2.3 ks) *RXTE* observation of Cyg X-1 in the high/soft state, obtained on 1996 June 18[2]. Using Proportional Counter Array (PCA) light curves with 2^{-8} s resolution, we measured the lag spectrum and PSD in two bands, 2–5.1 keV (soft band) and 8–13 keV (hard band). To keep the fitting simple, we consider only the ratio of the PSDs, after Poisson noise subtraction, and not the energy-dependent PSD shapes themselves, so we do not attempt to match the PSD shape by assuming any particular input signal. This approach allows us to estimate the lags and filtering effect in a simple analytical way, by assuming that each frequency contributing to the lag spectrum and PSD ratio corresponds to a single radius, so input signal PSDs do not overlap in frequency, with the lags and PSD filtering determined using the analytical expressions given in Appendix A.

We first stress that due to the complexity of fitting even our model to

---

[2] Unfortunately, no single long observation of Cyg X-1 in this state, with a $1/f$ PSD, is known to us. We do not combine data from different high/soft state observations, in case there are variations in the timing properties on long time-scales.

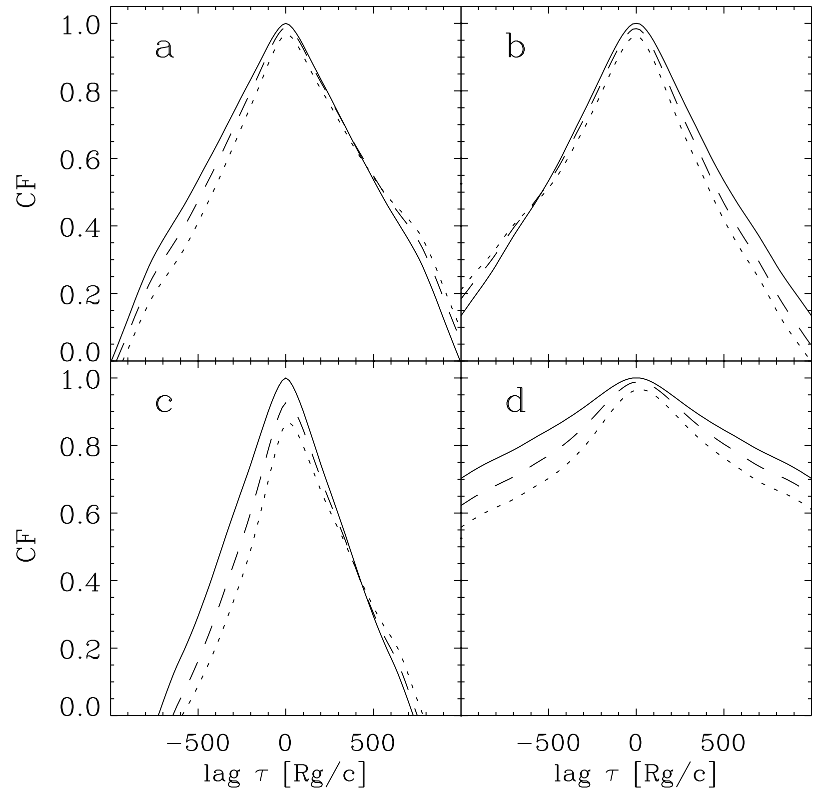

Figure 4.13: Auto- and Cross-Correlation functions for 4 stretches $10^4 R_\mathrm{g}/c$ long taken from a $10^6 R_\mathrm{g}/c$ long synthetic light curve. ACFs of light curves with $\gamma_\mathrm{soft} = 3$ are shown in solid lines, CCF between $\gamma_\mathrm{soft} = 3$ and $\gamma_\mathrm{hard} = 4$ and 5 in dashed and dotted lines, respectively. The time axis is in units of R_g/c, which equals 10 s for a mass of $2 \times 10^6 M_\odot$.

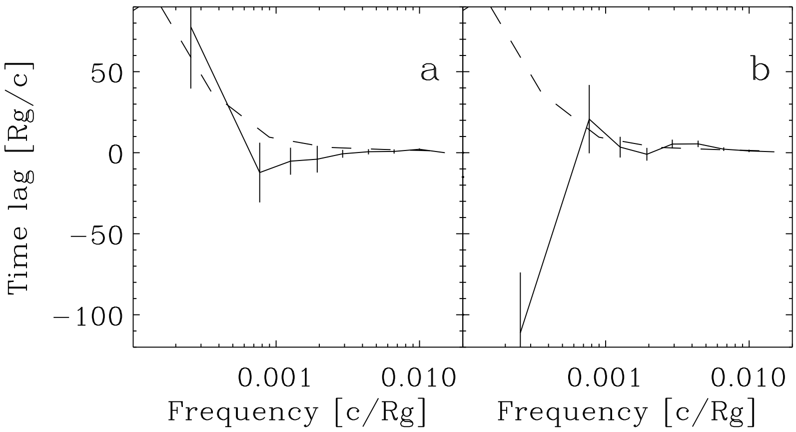

Figure 4.14: Time lags between simulated light curves of emissivity indices $\gamma = 3$ and 5. The dashed lines show the underlying lag spectrum, calculated from a long light curve ($\sim 10^6 R_\mathrm{g}/c$), the solid lines correspond to the lag spectra of short segments ($\sim 10^4 R_\mathrm{g}/c$) of the same light curve, also used in panels a and b of Fig. 4.13. The large scatter around the underlying lag spectrum is caused only by the limited number of points used. In panel a, the lags follows the underlying spectrum, and so, the corresponding CCF in Fig. 4.13 shows the expected positive-lag asymmetry, while the negative lags seen in panel b of Fig. 4.13 are caused by the outlier lag value at the lowest frequency bin in panel b.

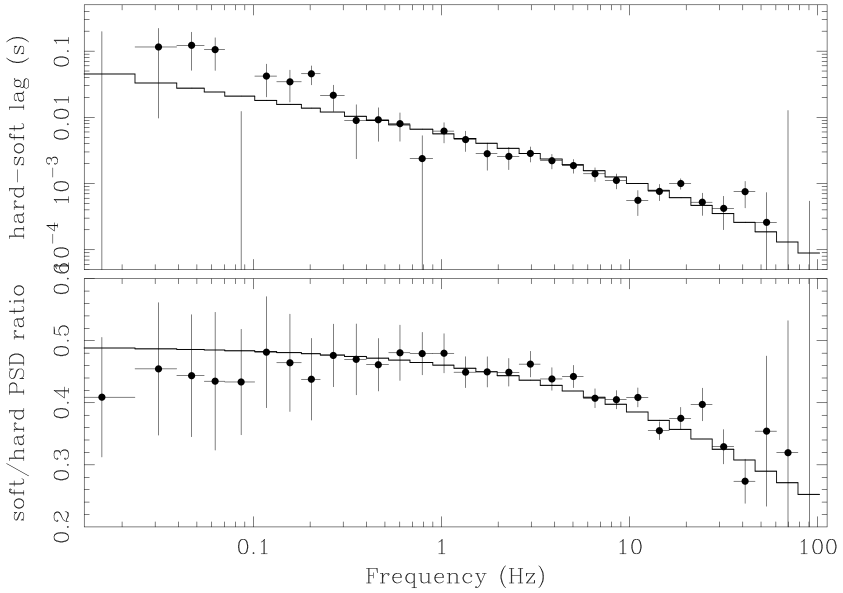

Figure 4.15: Time lags (top) and soft/hard PSD ratio (bottom) as a function of Fourier frequency for Cyg X-1 in the high/soft state (1996 June 18). The solid lines show the best-fitting analytical model described in the text.

the data, and the difficulty of quantifying certain measurement uncertainties (see below), we will only test the broad consistency of our model with the data. Therefore, we will not quote statistical errors on parameters derived here, which should be treated as only indicative of the underlying physical parameters. Since our model contains many parameters with complex degeneracies between them, we only fit the model with a few parameters left free, to demonstrate whether the model can reproduce the data. For all our fits, we assumed a black hole mass of 10 $\mathrm{M}_{\odot}$. The mass provides the scaling factor between the units of light-crossing time-scale used in our method, and the observed units of seconds. The effect of changing mass is therefore equivalent to that of a simple linear change in the quantity $(H/R)^2\alpha$ (see Section 4.4.2) at all radii, and is rather weak except at high frequencies. Consistent with our earlier simulations, we initially keep $(H/R)^2\alpha = 0.3$ at all radii. We assume a fixed outer disc radius $r_{\mathrm{max}} = 10^5$ R_{g}, but allow the inner disc radius r_{min} to vary, down to a minimum value of 1.23 R_{g} (i.e. the minimum stable orbit for a Kerr black hole). For simplicity, the soft emissivity index was initially fixed at $\gamma_{\mathrm{soft}} = 3$, while γ_{hard} was allowed to vary. We also introduced an additional normalising factor for the lags, so that all the lags predicted by the model can be increased by a single factor, which we leave free to vary in the fits. This renormalisation represents the possibility that the fluctuations propagate at some speed proportional to the theoretically predicted local drift velocity (see section 4.3.1), but not necessary equal to it.

Note that the PSDs in different energy bands can have different overall normalisations for a variety of reasons. For example, if a strong constant thermal emission component is present, as in the high/soft state (see Churazov et al. 2001), the variability is diluted in the soft band and the PSD normalisation reduced. Alternatively, spectral pivoting at high energies (e.g. due to Compton cooling of the corona), which we do not model here, can lead to a larger normalisation in the soft band compared to the hard band (e.g. see Uttley & M$^{\mathrm{c}}$Hardy 2005 for evidence of this effect in the AGN NGC 3227). For these reasons, when fitting our model we allow the normalisation of the PSD ratio to be free.

The observed lag and soft/hard PSD ratio spectra are shown in Fig. 4.15, together with the best-fitting model resulting from a joint fit of the lag and filtering equations to the data, i.e. we assume the same parameters for fitting both the lag and ratio plot. The reduced chi-squared, $\chi^2/\mathrm{d.o.f.} = 0.81$, indicates an excellent fit, for a renormalisation factor of 1.86 (i.e. fluctuations propagate at ~ 1.9 times lower drift velocity than given by standard disc theory), $r_{\mathrm{min}} = 1.23$, and $\gamma_{\mathrm{hard}} = 3.53$. We caution however that the goodness-of-fit is almost certainly over-estimated, since the random errors in the soft and hard PSDs are correlated at low frequencies due to the intrinsic correlation between the light curves in these bands (the correlation is much weaker at high frequencies due to Poisson noise effects), and hence the error bars at these frequencies are almost certainly over-estimated. Furthermore, there is likely some additional uncertainty in PSD ratio at high frequencies, since an assumed Poisson noise level had to be subtracted from each PSD before the ratio was taken, and the uncertainty in the assumed noise level is not accounted for in the fit.

The small inner disc radius preferred by the data is consistent with a rapidly rotating black hole. However, this interpretation is strongly governed by our assumptions about the emissivity profile, and our simplifying assumption that each frequency corresponds to a single input signal. Since the travel time of material from 6 R_{g} to 1.23 R_{g} is very short, the value of r_{min} is not driven by lags at lower frequencies, but is mainly due to a combination of the relatively large high-frequency lags, and the weak drop in PSD ratio at high frequencies. Indeed, the frequencies corresponding to signals at 6 R_{g} and 1.23 R_{g} are 65 Hz and 700 Hz respectively, so that if the edge of the emitting region were observed at 6 R_{g} a very pronounced drop in both the lags and the PSD ratio would be observed approaching this frequency, hence the smaller radius is preferred. However, if the input signals overlap substantially, the larger lags from signals at larger radii can contribute even at high frequencies, so a strong drop in lag and PSD ratio would not be expected (see section 4.4.3). There may also be substantial emission at radii smaller than r_{min}, which is not considered in our model. This would also increase the lags at high frequencies and reduce the effects of filtering which cause the drop in PSD ratio at high frequencies. Thus, the small value of r_{min} inferred from our fit is quite model-dependent and should be treated with caution.

For completeness we note here that, unlike the smooth $1/f$ shape seen in the high/soft state, Cyg X-1 in the low/hard state is characterised by a band-limited PSD with a few humps, which can be modelled as four broad Lorentzian components (Pottschmidt et al. 2003). The lag spectrum also reveals a stepped structure, but it still follows approximately a $f^{-0.7}$ power law slope. Although the model can fit reasonably well the general trend seen in the PSD ratio and lag spectra, it cannot reproduce these detailed features, indicating that some of the model assumptions are not appropriate in this case. In particular, our simple implementation of the model uses power law emissivity indices and equal variability power per contributing annulus, so these smooth functions cannot produce additional structure at a few given frequencies. The general scheme of propagating fluctuations can still be correct but additional assumptions need to be made, for example, assuming that a few annuli have much enhanced variability power will certainly produce a bumpy PSD and might reproduce the steps in the lag spectra, as suggested by Nowak (2000) and also Kotov et al. (2001).

4.7 Discussion

The extended emitting region in our model is responsible for the high frequency bend in the PSD, and the associated radial emissivity profiles produce the energy dependence of the PSD and the time lags. In this section we will summarise the spectral-timing properties produced by our model, consider the implications of our model for the size of the emitting region, and discuss some possible improvements.

4.7.1 Time lags

Keeping the local variability time-scales tied to the propagation time-scale produces time lag spectra of power law slope ~ -1 or flatter, and lags of $\sim 1 - 10\%$ of the variability time-scale, for a wide range of model parameters. As discussed in Sections 4.5 and 4.6, these simple assumptions produce lag spectra that match the data well in time-scale dependence and amplitude. We note once again that these lags arise solely due to the difference in emissivity profiles of the X-ray energy bands and do not involve any other spectral evolution of the emitting region. The amplitude of the lags depends mostly on the emissivity indices of the energy bands, increasing rapidly with their difference, up to $\Delta\gamma \sim 1$, above which the lag values tend to saturate. Significant lags can appear between energy bands characterized by similar emissivity profiles and, correspondingly, similar PSD shapes. In particular, the PSD of Cyg X-1 in the high/soft state shows rather weak energy dependence (see Section 4.6.1), but the PSD ratio and lags can still be reproduced simultaneously with close emissivity indices for each energy band ($\Delta\gamma \sim 0.5$), provided that the propagation time-scale is slightly longer than the local fluctuation time-scale, and assuming that the inner disc radius is small. The power-law shape of the lag spectra is quite robust, its slope depends only weakly on disc structure parameters $(H/R)^2\alpha$. Incidentally, the stability of the lag spectra might explain the behaviour seen in, e.g. Cyg X-1, in different spectral states. This object shows very different PSD and energy spectra in the high/soft and low/hard states, indicative of different disc configurations, but surprisingly similar lags (Pottschmidt et al. 2000).

4.7.2 PSD shape

A comparison with AGN and BHXRB data in the high/soft state shows that the filtering effect of the extended emitting region, acting on a simple $1/f$ underlying PSD shape, can broadly reproduce their PSD shape and energy dependence. Cyg X-1 in the low/hard state, however, requires a more complex *intrinsic* PSD. In either case, the extended emitting region introduces a bend in the PSD in addition to any intrinsic curvature, and produces the energy dependence of the filtered PSDs.

Note that the bending power-law, used to fit AGN data, is only an approximation to the actual PSDs produced by the fluctuating-accretion model. The filtered PSD bends down continuously at high frequencies and has no well-defined high-frequency power law slope. The difference between the bending power-law model and the filtered PSDs can be appreciated in Fig. 4.11, where the single-bend PSD fit overestimates the power in the highest frequency bins. However, as this region of the PSDs from real data is often heavily affected by Poisson noise, the associated error bars and scatter are large and it is not possible to appreciate any deviations from a simple power law slope. Therefore, even better AGN data would be needed to discern if the model can replicate the exact PSD shape or if additional variability components are needed.

In our model, thick disc parameters, $\alpha(H/R)^2 = 0.3$, in the inner regions of the accretion flow and inner radius $r_{\rm min} = 6$ puts the break frequency around $10^{-4} - 10^{-3} c/R_{\rm g}$ (i.e. ~2 - 20 Hz for a $10 M_{\odot}$ black hole, $2 \times 10^{-5} - 2 \times 10^{-4}$ for a $10^6 M_{\odot}$). These values are in general agreement with the average break frequencies of AGN and BHXRBs, indicating that fluctuations on the viscous time-scales of a geometrically thick accretion flow are appropriate to explain the variability. A geometrically thick disc is necessary to produce the observed high frequency fluctuations as *viscous* frequencies. If the fluctuations were instead produced on dynamical time-scales, or a magnetic time-scale related to this, as in e.g. King et al. (2004), then a thinner flow might be allowed. However, the fluctuations need not only be produced but also propagated, which poses a difficulty for much thinner accretion flows, as fluctuations on time-scales much shorter than the propagation time-scale are easily damped. This, of course, does not rule out an additional thin disc, possibly underlying the thick flow, that might contribute to the flux but not to the variability.

4.7.3 Extent of the emitting region

In our implementation of the variability model, the X-ray emitting region extends out to large radii. The bend in the PSD is produced by the radial distribution of variability time-scales and emissivity profiles alone and is not related to a characteristic time-scale at the maximum radius of emission. Therefore, an outer edge to the emitting region might be allowed but is not required. The steep emissivity profiles concentrate most of the emitted flux in the centre so, apparently, it would make little difference to the PSD if the emitting region were truncated at some radius or if it extended out to infinity. However, the extent of the emitting region has a major impact on the lag spectra. If, for example, the X-ray emission is confined to the central few R_g and responds to the variability pattern produced outside this radius, then time lags would still appear due to the radial segregation of the energy bands but, to first order, the lags would have the same value at *all* Fourier frequencies (e.g. Nowak et al. 1999a). In our case, frequency-dependent lags appear because the fluctuations are produced *within* the emitting region. This consideration gives further support to the idea that f_{b} does not correspond to the characteristic frequency of an outer edge of the emitting region, as noted above, as these lags are observed far below the break frequency. This, in turn, implies that the X-ray emitting region should extend at least as far as the radius correspondent to the longest time-scales where frequency-dependent lags are observed.

4.7.4 Improvements to the model

We have made a number of simplifying assumptions that seem to reproduce the broad spectral timing properties of AGN and BHXRBs. The detailed predictions of PSDs and lag spectra can be improved by including some additional effects.

As a first step, the assumption that all radii in the disc produce the same amplitude of fluctuations can be relaxed, allowing for strongly enhanced variability at a few discrete annuli. This scenario might represent Cyg X-1 in the low/hard state where the PSD appears to be composed of a few broad Lorentzians, so it would be interesting to check if the effect of the extended emitting region would reproduce well the steps observed in the PSD ratio and in the lag spectra. This issue will be investigated in a forthcoming paper (Uttley & Arévalo, in prep.).

To simplify the calculations, we have only allowed for power-law radial emissivity profiles. Though this appears to be a reasonable assumption given the profile of total energy loss expected for an accretion disc, it is not clear that each energy band should follow a simple power-law profile. For example, the energy spectrum reveals other components in addition to the direct continuum that might be expected from an optically thin X-ray emitting corona. In BHXRBs in the high/soft state, blackbody disc emission is also seen, although it does not vary significantly on short time-scales (Churazov et al. 2001), so may not contribute to the observed PSD and lag spectra. However, in several AGN (e.g. NGC 4051, Uttley et al. 2004), strongly variable soft excess emission is seen below ~ 1 keV, which may be associated with Comptonised disc emission and hence could contribute a different component to the emissivity profile in the soft band. Other complex profiles might be expected. For example, by fitting the profile of the broad iron line in MCG-6-30-15 with a relativistic disc-line model, Fabian et al. (2002) have inferred a broken power-law emissivity profile, which steepens from $\gamma = 2.5$ (i.e. similar to the value we infer for NGC 4051) to $\gamma = 4.8$ within 6 R_g of the black hole. Thus, more complex emissivity profiles, perhaps with breaks or additional components, and taking account of general relativistic effects, could be considered. Additional variable components, arising for example through reflection or reprocessing of the primary variable emission, can also affect the coherence and time lags and should be included in more detailed variability models. In particular, in high quality data from Cyg X-1, Kotov et al. (2001) show that a reflection component is necessary to reproduce the detailed *energy dependence* of the lags.

The simple fluctuating-accretion model presented here agrees generally well with the observational variability measurements, but still needs to be set on physical grounds to be fully validated. A physical treatment must consider two things, the source of the variability (i.e. source of accretion rate fluctuations, for example), and the source of emission. Work on the evolution of a physical (if simplified) accretion flow, implemented with numerical simulations (e.g King et al. 2004), suggests that the necessary accretion rate fluctuations and propagation can be realized physically. Finally, a model for the emission process, and its coupling to the accretion rate fluctuations, will be necessary to provide a physical motivation for the radial emissivity profiles of each energy band and, with it, a meaningful interpretation of the emissivity indices.

4.8 Conclusions

We have used a computational fluctuating-accretion model to reproduce the spectral-timing properties of X-ray light curves from AGN and BHXRBs. In the model, the variability is produced throughout the accretion flow as perturbations of the accretion rate on the local viscous time-scale, produced by many signals which are geometrically spaced in temporal frequency. The fluctuations propagate inward at the radial drift velocity and modulate the fluctuations produced further in. This general scheme, introduced by Lyubarskii (1997), produces light curves which possess $1/f$ type PSDs over a broad range of time-scales and follow a linear rms-flux relation. Following Kotov et al. (2001), X-ray emission from a radially extended region is assumed to track the local accretion rate fluctuations and to show a power law radial emissivity profile, which steepens for higher energy bands. The different emissivity profiles and the inward propagation produce differences between the PSDs of each energy band and introduce time lags. Our implementation of the model is successful in reproducing the observed variability properties of AGN and BHXRBs, as follows:

1. We reproduce the expected $\sim 1/f$ frequency-dependence of time lags between energy bands, and lag amplitudes of a few per cent of the variability time-scales, predicted by Kotov et al. (2001) and observed in BHXRB and AGN variability data.

2. We demonstrate that the amplitudes and slopes of the lag spectra are only weakly dependent on changes in the emissivity indices, the radial dependence of the product of disc parameters $(H/R)^2\alpha$, and the strength of damping of accretion fluctuations. The robust nature of the lag spectra may help to explain the similarity of lag spectra in the low/hard and high/soft states in Cyg X-1 (Pottschmidt et al. 2000), despite the very different PSD and energy-spectral shapes in these states.

3. The extended emitting region suppresses short time-scale fluctuations, producing a gradual bend in the PSD at high frequencies. The 'filtered' PSD shapes resemble those of AGN and BHXRBs in the high/soft state (e.g. M^{c}Hardy et al. 2004) and can be approximately fitted with a bending power-law model. The bend frequencies obtained match the observed frequencies if the fluctuations are produced on the viscous time-scales of a geometrically thick accretion flow. Values of $(H/R)^2\alpha \sim 0.3$ gave adequate bend frequencies compared to data

from Seyfert galaxies NGC 4051 and MCG-6-30-15 and the BHXRB Cyg X-1.

4. The fact that all energy bands are produced by the same emitting region can maintain a high coherence (> 0.95) between light curves of different energy bands, as observed by e.g. Nowak et al. (1999a) and Vaughan et al. (2003). However, the coherence can be substantially reduced at high frequencies if input signals at each radius have fairly broad PSDs and the difference between emissivity profiles in different bands is large. Coherence is also reduced if damping of the inward-propagating fluctuations is significant. These results may provide an explanation for the drops in coherence observed at high frequencies in various BHXRBs and AGN (Nowak et al. 1999a; Vaughan et al. 2003; M^{c}Hardy et al. 2004).

5. The model can simultaneously reproduce both the observed energy-dependence of PSD shape and the lag spectrum for the AGN NGC 4051 and the BHXRB Cyg X-1 in the high/soft state, although the inferred propagation times in Cyg X-1 are slightly slower than the drift velocity expected for a standard disc. In the low/hard state of Cyg X-1, our model can reproduce the general slope of the lag spectrum but cannot account for the stepped shape of the lag spectrum. Modelling the detailed features of this spectrum would require additional assumptions about the mechanism producing the variability.

6. Although direct comparison with spectral-timing data from AGN and BHXRBs shows good general agreement with our model, we note that, if our model is correct, the empirical bending or broken power-law models used to fit the PSDs of AGN and BHXRBs in the high/soft state must break down for high signal-to-noise data, because they only approximate the gradual bending shape predicted by our model. In particular, we note that our model implies that the PSD bend time-scale measured for AGN and BHXRBs is a function of both the underlying PSD of accretion fluctuations *and* the emissivity profile of the observed energy band. Therefore the PSD bend time-scale is not necessarily associated with the outer radius of the emitting region, which can in principle be extremely large, provided the emissivity profile is relatively steep.

Acknowledgments

This research has made use of data obtained from the High Energy Astrophysics Science Archive Research Center (HEASARC), provided by NASA's Goddard Space Flight Center. PA acknowledges support from the International Max-Planck Research School in Astrophysics (IMPRS), travel support from grants associated with the NASA *RXTE* Guest Observer program, and the hospitality of NASA's Goddard Space Flight Center. PU acknowledges a Research Associateship from the National Research Council.

4.9 Appendix A: Analytical estimates for filtered PSD and lags

As mentioned in Sec. 4.3, the extended emitting region acts as a low-pass filter on the PSD. This filter factor, F, can be approximated as:

$$\mathrm{PSD_{filt}}(f) = \mathrm{PSD}(f) \times F(r_f) = \mathrm{PSD}(f) \left(\frac{\int_{r_{\mathrm{min}}}^{r_f} \epsilon(r) 2\pi r dr}{\int_{r_{\mathrm{min}}}^{\infty} \epsilon(r) 2\pi r dr} \right)^2 \tag{4.5}$$

Taking the emissivity profile $\epsilon(r) = r^{-\gamma}(1 - \sqrt{r_{\mathrm{min}}/r})$, the filter factor takes the form (for $\gamma > 2$):

$$\begin{aligned} F(r_f) &= \left(\frac{\frac{r_f^{2-\gamma} - r_{\mathrm{min}}^{2-\gamma}}{2-\gamma} - \sqrt{r_{\mathrm{min}}} \frac{r_f^{1.5-\gamma} - r_{\mathrm{min}}^{1.5-\gamma}}{1.5-\gamma}}{\frac{r_{\mathrm{min}}^{2-\gamma}}{\gamma-2} + \frac{r_{\mathrm{min}}^{2-\gamma}}{1.5-\gamma}} \right)^2 \\ &= \left(1 - \frac{2 r_f^{2-\gamma}}{r_{\mathrm{min}}^{2-\gamma}} \left(\gamma - 1.5 - \sqrt{\frac{r_{\mathrm{min}}}{r_f}} (\gamma - 2) \right) \right)^2 \end{aligned} \tag{4.6}$$

In our implementation, the fluctuations are produced on the viscous timescale at the radius of origin, so $r_f = (2\pi f (R/H)^2/\alpha)^{-2/3}$. Substituting this value in the equation above gives the PSD filtering factor as a function of frequency f, where f is in units of c/R_g. This approximation for the filtering effect is appropriate for narrow-input-PSD signals, where most of the variability power produced by each annulus is produced on the corresponding viscous time-scale. Finite travel time effects contribute to cancel out variability produced at higher frequencies than f_{visc}, so the filtered PSD in this case is distorted further.

For the calculation of the time lags, the average travel time of a signal produced at r_s can be approximated as:

$$\bar{\tau}(s) = \frac{\int_{r_{\min}}^{r_s} \tau(r, r_s)\epsilon(r) 2\pi r dr}{\int_{r_{\min}}^{r_s} \epsilon(r) 2\pi r dr}, \tau(r, r_s) = \int_r^{r_s} \frac{d\tilde{r}}{v(\tilde{r})} \tag{4.7}$$

If the fluctuations propagate with viscous velocity, $v(r) = \alpha(H/R)^2 r^{-1/2}$, then $\tau(r, r_s) = \frac{2}{3\alpha(H/R)^2}(r_s^{3/2} - r^{3/2})$ and the average travel time can be calculated using the emissivity profile given above. For example, for the case where $\gamma \neq 1.5, 2, 3, \frac{7}{2}$, the average travel time is:

$$\bar{\tau}(s) = \frac{\left[\frac{2}{3\alpha(H/R)^2}\left(r_s^{\frac{3}{2}}\frac{r_s^{2-\gamma} - r_{\min}^{2-\gamma}}{2-\gamma} - r_s^{\frac{3}{2}} r_{\min}^{\frac{1}{2}} \frac{r_s^{\frac{3}{2}-\gamma} - r_{\min}^{\frac{3}{2}-\gamma}}{\frac{3}{2}-\gamma} - \frac{r_s^{\frac{7}{2}-\gamma} - r_{\min}^{\frac{7}{2}-\gamma}}{\frac{7}{2}-\gamma} + r_{\min}^{0.5}\frac{r_s^{3-\gamma} - r_{\min}^{3-\gamma}}{3-\gamma}\right)\right]}{\frac{r_s^{2-\gamma} - r_{\min}^{2-\gamma}}{2-\gamma} - r_{\min}^{0.5}\frac{r_s^{\frac{3}{2}-\gamma} - r_{\min}^{\frac{3}{2}-\gamma}}{\frac{3}{2}-\gamma}} \tag{4.8}$$

Substitution of the exponentials with logarithms in the appropriate terms give the equation for the rest of the cases. For signals produced on the viscous time-scale of the radius of origin, r_s can be substituted by r_f as above, producing average travel times as a function of temporal frequency. Finally, the difference between $\bar{\tau}(f)$ calculated for two different emissivity indices γ gives the time lag spectrum corresponding to this γ pair.

4.10 Appendix B: Spectral-timing measurements

We estimate the PSD using the periodogram, where the variability power, $P(f_i)$, is calculated for discretely sampled frequencies f_i as:

$$P(f_i) = \frac{2}{\bar{s}^2}\frac{\Delta t}{N}|\mathrm{Re}_S^2(f_i) + \mathrm{Im}_S^2(f_i)|, \tag{4.9}$$

where $\mathrm{Re}_S(f_i)$ and $\mathrm{Im}_S(f_i)$ are the real and imaginary parts of the discrete Fourier transform of the time series $s(t)$, $\bar{s}$ is the average count rate, Δt is the sampling time interval and N is the number of sampled points (Press et al. 1992).

The Cross Spectrum between two time series, e.g. simultaneous soft and hard light curves, $s(t)$ and $h(t)$, is defined as $C(f) = S^*(f)H(f)$, where $S(f)$ and $H(f)$ are the Fourier transforms of the respective light curves. The Cross Spectrum is a complex-valued function, from where the coherence and phase lags can be extracted. The coherence γ^2 for discretely sampled time series is calculated as:

$$\gamma^2(f_i) = \frac{\langle \mathrm{Re}_C(f_i)\rangle^2 + \langle \mathrm{Im}_C(f_i)\rangle^2}{\langle |\mathrm{S}(f_i)|^2\rangle \langle |\mathrm{H}(f_i)|^2\rangle} \tag{4.10}$$

where $\mathrm{Re}_C(f_i)$ and $\mathrm{Im}_C(f_i)$ are the real and imaginary parts of the Cross Spectrum $C(f)$ and angle brackets represent averaging over independent measurements (i.e. the numerator in the equation is the modulus-squared of the averaged cross-spectrum). Note that here, the averaging of independent measurements of the cross-spectrum and PSD is carried out by binning up in frequency, as well as by averaging measurements of the cross-spectrum measured at the same frequency from separate light curve segments.

The argument of the Cross Spectrum defines the phase lags: $\phi(f_i) = \arg \langle C(f_i)\rangle$, and from here the time lags, $\tau(f_i)$, are calculated as:

$$\tau(f_i) = \frac{\phi(f_i)}{2\pi f_i} = \frac{1}{2\pi f_i} \arctan \left\{ \frac{\langle \mathrm{Im}_C(f_i)\rangle}{\langle \mathrm{Re}_C(f_i)\rangle} \right\} \tag{4.11}$$

For a more detailed discussion on the measurement and interpretation of coherence and time lags, and the determination of errors on these measurements, see Vaughan & Nowak (1997) and Nowak et al. (1999a) and, in the context of AGN, Vaughan et al. (2003).

Chapter 5

Conclusion

The X-ray emission in AGN is intimately linked to the central engine that powers these objects. The rapid, high amplitude variability often observed in the X-ray band indicates that this flux must be emitted by a very compact region. This fact, in addition to the high energy of the photons, suggests that the X-rays are emitted where most of the energy is released. If the central engine is in fact an accreting super massive black hole, these arguments connect the X-ray emitting region to the centre of the accretion flow. We studied two Narrow Line Seyfert 1 galaxies, a type of AGN that displays the strongest X-ray fluctuations on short time-scales. This strong variability enabled us to extract a maximum of information from the time series. The light curves were generated with data taken by *XMM-Newton*. This observatory can produce the longest continuous observations, and its large collecting area permits accurate flux measurements with short exposures, allowing us to disentangle structures in a broad range of time-scales.

The analysis of the X-ray flux variability can be used to reveal the structure of the central engine. The data and analyses presented support the idea that two distinct emitting regions contribute to the observed flux, an optically thick thermal emitter and an optically thin Comptonising scatterer. The presence of a coronal component is supported by spectral fitting to the X-ray data, as shown in Chapter 2, where the X-ray spectrum of the Seyfert 1 galaxy PKS 0558-504 can be described well as two Comptonisation components. The optically thick thermal component is necessary to produce the seed UV photons to be Comptonised into X-rays and can be also responsible for the observed Optical/UV flux. As shown in Chapter 3, at least in the Seyfert 1 galaxy MCG-6-30-15, the lack of correlated variability with UV lagging X-rays, and the much smaller variability amplitude of the UV, indicate that the UV photons are not mainly produced through reprocessing of X-rays, showing that there must be at least two emission mechanisms at play. This gives further supports the hypothesis that both an accretion disc and a corona must be present and contribute to the observed flux.

As discussed in Chapter 4, the variability most likely arises from the accretion flow itself, so it can characterise the physics of the accretion process. The observed variability properties, in particular the break time-scale of the Power Spectral Density (PSD), indicate that a part of the flow must behave like a geometrically thick disc. This configuration is necessary to achieve the highest frequency fluctuations and allow their efficient propagation into the X-ray emitting region. Furthermore, if the fluctuations propagate towards the centre, as expected, the lags observed between different X-ray energy bands suggest that higher energies are produced by increasingly more compact regions. The observed lags and energy dependence of the PSD are consistent with a scenario where the X-rays are emitted by a radially extended corona, whose temperature and/or optical depth increase towards the centre. This extended corona can be identified with the optically thin, geometrically thick flow that produces and propagates the fluctuations.

Additional support for the hypothesis that the variability arises from the accretion flow is given by the X-ray/UV correlation in MCG-6-30-15. As discussed in Chapter 3, the observed delay in the X-ray fluctuations with respect to the UV is consistent with fluctuations propagating down the accretion disc, from a region producing mostly thermal UV photons, to the region emitting the bulk of the X-rays. In this case, the slight variations in the UV flux should be produced by the optically thick flow itself. As the same fluctuations are later observed in the X-rays, there must be a connection between both flows, optically thick and optically thin. A favoured scenario is a geometrically thin and optically thick flow extending to large radii, that converts, at least partially, into an optically thin, geometrically thick flow towards the centre.

The success of the propagating-fluctuation scheme also shows the power of phenomenological modelling. Purely theoretical modelling of accretion flows cannot, as yet, predict their behaviour from first principles nor reproduce the complexity of the observations. Numerical implementations, that follow the physical evolution of the accretion flow, can test more complex predictions of the accretion theory but still need to make simplifying assumptions, in order to be computable in finite time. In particular, self consistent modelling of the entire accretion disc/corona would require very extensive calculations. A phenomenological treatment of the accretion disc/corona connection can complement these two approaches. It can provide quantitative predictions that can be readily compared with the data to produce rough estimates of the overall structure of the central engine. Future efforts will be directed to extent the propagating-fluctuation phenomenological scheme to include possible interactions between the emitting regions, through the propagation of fluctuations from the UV-emitting region to the X-ray emitting region and through reprocessing of X-rays into the UV regime.

References

Antonucci R. R. J., Miller J. S., 1985, ApJ, 297, 621

Ballantyne D. R., Vaughan S., Fabian A. C., 2003, MNRAS, 342, 239

Benlloch S., Wilms J., Edelson R., Yaqoob T., Staubert R., 2001, ApJ,562, L121

Boller Th., Brandt W.N., Fink H., 1996, A&A, 305, 53

Boller Th., Brandt W.N., Leighly K.M., Ward M.J., 2000, eds. 'Proceedings of the Workshop on Observational and Theoretical Progress in the Study of NLS1 Galaxies', New Astron. Reviews 44, 381

Brandt W.N., Boller Th., 1998, Astron. Nachr., 319, 7

Brandt W.N., Boller Th., Fabian A.C., Ruszwoski M., 1999, MNRAS, 303, L53

Brinkmann W., Grupe D., Branduardi-Raymont G., & Ferrero E., 2003, A&A, 398, 81

Brinkmann W., Yuan W., & Siebert J., 1997, A&A, 319, 413

Chiang J., Reynolds C. S., Blaes O. M., et al., 2000, ApJ, 528, 292

Churazov E., Gilfanov M., Revnivtsev M., 2001, MNRAS, 321, 759

Corbin M.R., 1997, ApJS, 113, 245

Czerny B., Nikolajuk M., Piasecki M., Kuraszkiewicz J., 2001, MNRAS, 325, 865

den Herder J.W., Brinkman A.C., Kahn S.M., et al., 2001, A&A, 365, L7

De Vaucouleurs G., 1948, Annales d'Astrophysique, 11, 247

Edelson R.A., Krolik J.H., 1988, ApJ, 333, 646

Ehle M., Breitfellner M., Dahlem M., et al., 2001, XMM-Newton Users' Handbook,

Fabian A.C., 1979, Proc. R. Soc. London, Ser. A, 366, 449

Fabian A.C., Vaughan S., Nandra, K., et al., 2002, MNRAS, 335, L1

Fabian A. C., Vaughan S., 2003, MNRAS, 340, L28

Fabian A. C., Vaughan S., Nandra, K., et al., 2002, MNRAS, 335, L1

Freeman K. C., 1970, ApJ, 161, 802

Gaskell M., 2004, ApJ, 612, L21

Ghizzardi S., Molendi S., 2001, Proc. of the conference 'New Visions of the X-ray Universe', ESTEC Nov. 2001
Gierliński M., Zdziarski A., 2003, MNRAS, 343, L84
Gliozzi M., Boller Th., Brinkmann W., Brandt W.N., 2000, A&A, 356, L17
Gliozzi M., Brinkmann W., O'Brien P.T., et al., 2001, A&A, 365, L128
Gliozzi M., Brinkmann W., Räth C., Papadakis I.E., et al., 2002, A&A, 391, 875
Goodrich R.W., 1989, ApJ, 342, 224
Grupe D., Beuermann K., Mannhein K., Thomas H.-C., 1999, A&A, 350, 805
Guilbert P.W., Rees M.J., 1988, MNRAS, 233, 475
Haardt F., Maraschi L., 1991, ApJ, 380, 51
Haardt F., Maraschi L., 1993, ApJ, 413, 507
Haardt F., Maraschi L., Ghisellini G., 1994, ApJ, 432, L95
Hayashida K., Miyamoto S., Kitamoto S., Negoro H., Inoue H., 1998, ApJ, 500, 642
Iwasawa K., Fabian A.C., Reynolds C.S., et al., 1996, MNRAS, 282, 1038
Kaspi S., Smith P.S., Netzer H., et al., 2000, ApJ, 533, 631
Kato S., Fukue J., Mineshige S., 1998, Black-Hole Accretion Disks. Kyoto University Press, Kyoto
Kazanas D., Hua X.-M., Titarchuk L., 1997, ApJ, 480, 735
King A. R., Pringle J. E., West R. G., Livio M., 2004, MNRAS, 348, 111
Kotov O., Churazov E., Gilfanov, M., 2001, MNRAS, 327, 799
Kuhlbrodt B., Wisotzki L., Jahnke K., 2004, MNRAS, 349, 1027
Lyubarskii Y. E., 1997, MNRAS, 292, 679
Maoz D., Markowitz A., Edelson R., Nandra K., 2002, AJ, 124, 1988
Markowitz A., 2005, (astro-ph/0508521)
Markowitz A., Edelson R., Vaughan S., et al., 2003, ApJ, 593, 96
Mason K.O., Breeveld, A., Much R. et al., 2001, A&A, 365, 36
Mason K.O., McHardy I.M., Page M. J. et al., 2002, ApJ, 580, 117
Matt G., Fabian A.C., Reynolds C.S., 1997, MNRAS, 289, 175
Merloni A., 2003, MNRAS, 341, 1051
Merloni A., Fabian A.C., 2001, MNRAS, 321, 549
Merloni A., Fabian A.C., 2002, MNRAS, 332, 165
Mineshige S., Kawagichi T., Takeuchi M., Hayashida K., 2000, PASJ, 52, 499
Mineshige S., Takeuchi M., Nishimori H., 1994, ApJ, 435, 125
Miniutti G., Fabian A.C., Goyder R., Lasenby A. N., 2003, MNRAS, 344, 22
Miyamoto S., Kitamoto S., 1989, Nature, 342, 773

Moran E.C., Halpern J.P., Helfand D.J., 1996, ApJS, 106, 341
M^{c}Hardy I. M., Gunn K. F., Uttley P., Goad M. R., 2005, MNRAS, 359, 1469
M^{c}Hardy I. M., Papadakis I. E., Uttley P., Page M. J., Mason K. O., 2004, MNRAS, 348, 783
Nandra K., Le T., George I.M., Edelson R.A., et al., 2000, ApJ, 544, 734
Narayan R., Yi I., 1994, ApJ, L13
Nowak M. A., 2000, MNRAS, 318, 361
Nowak M. A., Vaughan B.A., Wilms J., Dove J.B., Begelman M.C., 1999a, ApJ, 510, 874
Nowak M. A., Wilms J., Dove J.B., 1999b, ApJ, 517, 355
O'Brien P.T., Reeves J.N., Turner M.J.L., et al., 2001, A&A, 365, L122
Osterbrock D.E., Pogge R.W., 1985, ApJ, 297, 166
Page K.L., O'Brien P.T., Reeves J.N., Breeveld A.A., 2003, MNRAS, 340, 1052
Page K.L., Pounds K.A., Reeves J.N., O'Brien P.T., 2002, MNRAS, 330, L1
Papadakis I. E., Nandra K., Kazanas D., 2001, ApJ, 554,133
Papadakis I. E., Petrucci P. O., Maraschi L., et al., 2002, ApJ, 573, 92
Persson S.E., 1988, ApJ 330, 751
Peterson B. M., McHardy I. M., Wilkes B. J., et al., 2000, ApJ, 542, 161
Peterson B. M., Wanders I., Horne K., et al., 1998, PASP, 110, 660
Petrucci P.O., Haardt F., Maraschi L., et al., 2001, ApJ, 556, 716
Pottschmidt K., Wilms J., Nowak M. A., et al., 2000, A&A, 357, 17
Pottschmidt K., Wilms J., Nowak M. A., et al., 2003, A&A, 407, 1039
Pounds K.A., Done C., Osborne J., 1995, MNRAS, 277, L5
Poutanen J., Fabian A.C., 1999, MNRAS, 306, L31
Press W.H., Teukolsky S.A., Vetterling W.T., Flannery B.P., 1992, Numerical Recipes. Cambridge University Press, Cambridge
Reig P., Papadakis I., Kylafis N. D., 2002, A&A, 382, 202
Remillard R.A., Bradt H.V., Buckley D.A.H., et al., 1986, ApJ, 301, 742
Remillard R.A., Grossan B., Bradt H.V., et al., 1991, Nature, 350, 589
Revnivtsev M., Gilfanov M., Churazov E., 2000, A&A, 363, 1013
Schlegel D., Finkbeiner D., Davis M., 1998, ApJ, 500, 525
Shakura N.I., Sunyaev R., 1973, A&A, 24, 337
Shemmer O., Uttley P., Netzer H., M^{c}Hardy I. M., 2003, MNRAS, 343, 1341
Siebert J., Leighly K.M., Laurent-Muehleisen S.A., et al., 1999, A&A, 348, 678
Simonetti J.H., Cordes M.J., Heeschen D.S., 1985, ApJ, 296, 46
Socrates A., Davis S.W., Blaes O., 2004, ApJ, 601, 405
Strüder L., Briel U.G., Dennerl K., et al., 2001, A&A, 365, L18

Sunyaev R., Titarchuck L.G., 1980, A&A, 86, 121

Tanaka Y., Nandra K., Fabian A. C., et al., 1995, Nature, 375, 659

Taylor R., Uttley P., M^{c}Hardy I.M., 2003, MNRAS, 342, 31

Timmer J., König M., 1995, A&A, 300, 707

Titarchuk L., 1994, ApJ, 434, 313

Titarchuk L., Lyubarskij Y., 1995, ApJ, 450, 876

Turner A. K., Fabian A.C., Lee, J., Vaughan S., 2004, MNRAS, 353, 319

Turner A. K., Fabian A.C., Vaughan S., Lee J.C., 2003, MNRAS, 346, 833

Ulvestad J.S., Antonucci R.R.J., Goodrich R.W., 1995, AJ, 109, 81

Urry C.M., Padovani P. 1995, PASP, 107, 803

Uttley P., 2004, MNRAS, 347, 61

Uttley P., M^{c}Hardy I. M., 2001, MNRAS, 323, 26

Uttley P., M^{c}Hardy I. M., 2005, MNRAS in press (astro-ph/0508058)

Uttley P., McHardy I.M., Papadakis I.E., 2002, MNRAS, 332, 231

Uttley P., M^{c}Hardy I. M., Papadakis I. E., 2002, MNRAS, 332, 231

Uttley P., Edelson R., McHardy I. M., et al., 2003, ApJ, 584, 53

Uttley P., Taylor R.D., M^{c}Hardy I.M., et al., 2004, MNRAS, 347, 1345

Uttley P., M^{c}Hardy I. M., Vaughan S., 2005, MNRAS, 359, 345

Van der Klis M., 1995, in Lewin, van Paradijs, van den Heuvel, eds. X-ray Binaries. Cambridge University Press, Campridge, p. 252

Vaughan B., Nowak M., 1997, ApJ, 474, L43

Vaughan S., Fabian A.C. 2004, MNRAS, 348, 1415

Vaughan S., Reeves J., Warwick R., Edelson R., 1999, MNRAS, 309, 113

Vaughan S., Fabian A.C., Nandra K., 2003a, MNRAS, 339, 1237

Vaughan S., Edelson R., Warwick R. S., Uttley P. 2003b, MNRAS, 345, 1271

Wang T., Matsuoka M., Kubo H., Mihara T., Negoro H., 2001, ApJ, 554, 233

Acknowledgments

I would like to acknowledge all the people that played an important role in the preparation of this thesis. First of all, I would like to thank my supervisor, Dr. Wolfgang Brinkmann, for introducing me to, and guiding me on, AGN research and X-ray data analysis. Special thanks also go to Dr. Iossif Papadakis who allowed me to participate in observational runs at Skinakas observatory and provided continuous help and support throughout the thesis. Thanks also to Dr. C. Räth and Dr. H. Scheingraber for instructing me on time series analysis, to Dr. M. Freyberg for invaluable help with *XMM-Newton* data reduction and to Dr. P. Uttley for many useful discussions.

I am also grateful to Prof. G. Morfill for accepting me in the theory group and providing financial support, and to the International Max-Planck Research School on Astrophysics (IMPRS) for allowing me to participate in their PhD programme.

I would also like to thank my friends for making my stay in Garching a wonderful experience; my parents, for their unconditional support and constant encouragement, and Jorge for always being there, and for helping me from the application to IMPRS to the revision of this thesis.